Role of the tetraspanin CD151 in the early human papillomavirus type 16 infection cascade

Dissertation

zur

Erlangung des Doktorgrades (Dr. rer. nat.)

der

Mathematisch-Naturwissenschaftlichen Fakultät

der

Rheinischen Friedrich-Wilhelms-Universität Bonn

vorgelegt von

Annika Massenberg

aus

Oberhausen

Bonn 2026

Angefertigt mit Genehmigung der Mathematisch-Naturwissenschaftlichen Fakultät der Rheinischen Friedrich-Wilhelms-Universität Bonn

Gutachter/Betreuer: Prof. Dr. Thorsten Lang

Gutachterin: Prof. Dr. Eva Kiermaier

Tag der Promotion: 27.03.2026

Erscheinungsjahr: 2026

Anmerkung

Teile dieser Arbeit wurden bereits in folgenden Publikationen veröffentlicht:

Massenberg, A.; Homsi, Y.; Schneider, C. N.; Mikuličić, S.; Döring, T.; Florin, L.; Lang, T. A rapid transfer of virions coated with heparan sulfate from the ECM to CD151 defines an early step in the human papillomavirus infection cascade, 2025, DOI: 10.1101/2025.04.17.649398.
In Teilen verwendet in Methoden (Abschnitt 3.2), Ergebnissen (Abschnitt 4.2 und 4.3) und Diskussion (Texte in "Anführungszeichen" wurden wörtlich zitiert und mit entsprechender Fußnote gekennzeichnet).

Mikuličić, S.; **Massenberg, A**.; Döring, T.; Brandenburg, K.; Lang, T.; Florin, L. HSPG-binding peptide Pep19-2.5 is a potent inhibitor of HPV16 infection. Antimicrobial agents and chemotherapy 2025, 69 (2), e0157524. DOI: 10.1128/aac.01575-24.
In Teilen verwendet in Methoden (Abschnitt 3.2.1, 3.2.9.4 und 3.2.9.9), Ergebnissen (Abschnitt 4.4) und Diskussion (Texte in "Anführungszeichen" wurden wörtlich zitiert und mit entsprechender Fußnote gekennzeichnet).

Mikuličić, S.; Shamun, M.; **Massenberg, A**.; Franke, A.-L.; Freitag, K.; Döring, T.; Strunk, J.; Tenzer, S.; Lang, T.; Florin, L. ErbB2/HER2 receptor tyrosine kinase regulates human papillomavirus promoter activity. Frontiers in immunology 2024, 15, 1335302. DOI: 10.3389/fimmu.2024.1335302.
In Teilen verwendet in Methoden (Abschnitt 3.2.3), Ergebnissen (Abschnitt 4.1.3) und Diskussion.

Table of contents

Table of contents

Abbreviations

a.u.	arbitrary units
A2t	annexin A2 heterotetramer
ADAM	a disintegrin and metalloprotease
Arf6	ADP-ribosylation factor 6
BSA	bovine serum albumin
BSA	bovine serum albumin
Cas9	CRISPR-associated protein 9
CD	cluster of differentiation’
Cdc42	cell division control protein 42 homolog
CRISPR	clustered regularly interspaced short palindromic repeats
CytD	cytochalasin D
ddH2O	double distilled water
DMEM	Dulbecco's Modified Eagle Medium
DMSO	dimethyl sulfoxide
DNA	deoxyribonucleic acid
DPBS	Dulbecco's phosphate-buffered saline
ECM	extracellular matrix
EdU	5-Ethinyl-2'-desoxyuridine
EGFR	epidermal growth factor receptor
ErbB2	human epidermal growth factor receptor 2
ESCRT	endosomal sorting complexes required for transport
EtOH	ethanol
F-actin	filamentous actin
FAK	focal adhesion kinase
FBS	fetal bovine serum
FWHM	full width at half maximum
GF	growth factor
GFP	green fluorescent protein
GFR	growth factor receptor
HCMV	human cytomegalovirus
HIV	human immunodeficiency virus

Abbreviations

HPV	human papillomavirus
HS	heparan sulfate
HSPG	heparan sulfate proteoglycan
HSV	herpes simplex virus
IF	immunofluorescence
Itgα6	integrin alpha 6
kb	kilo base pair
KLK8	kallikrein 8
LCR	long control region
LEL	large extracellular loop
LN332	laminin 332
mAb	monoclonal antibody
MEK	mitogen-activated protein kinase kinase
miRNA	micro ribonucleic acid
MMPs	matrix metalloproteinases
MVB	multivesicular bodies
OBSL1	obscurin-like protein 1
ORFs	open reading frames
Ori	origin of replication
p53	tumor protein p53
pA	polyadenylation
pAb	polyclonal antibody
pA_E	polyadenylation viral early
pA_L	polyadenylation viral late
PBS	phosphate buffered saline
PCC	Pearson correlation coefficient
PFA	paraformaldehyde
PLL	poly-L-lysine
PML-NBs	to promyelocytic leukemia nuclear bodies
PsV	pseudovirus
Rac1	Rac family small GTPase 1
RhoA	Ras homolog family member A

RNA	ribonucleic acid
ROI	region of interest
RT	room temperature
SALPs	synthetic anti-lipopolysaccharide peptides
SD	standard deviation
Sdc	syndecan
SEL	small extracellular loop
SIL	small intracellular loop
siRNA	small interfering ribonucleic acid
Src	Src kinase
STED	stimulated emission depletion
TEM	tetraspanin enriched microdomain
TIL	tumor-infiltrating lymphocyte
TMS	transmembrane segment
Tspan	tetraspanin
URR	upstream regulatory region
vge	viral genome equivalents
VLPs	virus-like particles
WASH	Wiskott-Aldrich Syndrome Protein and SCAR Homolog
WAVE	WASP-family Verprolin-homologous protein

List of Figures

List of Tables

1. Summary

Human papillomaviruses (HPV) are a diverse group of non-enveloped, double-stranded DNA viruses with profound significance in human health. An estimated 5% of all human cancer cases are attributed to HPVs. Among the types of cancer associated with HPV are cervical cancer, head and neck squamous cell carcinoma, anal cancer, and less common malignancies such as penile, vaginal, and vulvar cancers. HPVs are about 55 nm in size, and the capsid has an icosahedral structure. The viral capsid is composed of 72 pentameric capsomers, primarily assembled from 360 copies of the major capsid protein L1, with a smaller contribution from the minor capsid protein L2. For infection to occur, virions must reach dividing basal cells of the lower epithelium through a break in the epithelial barrier. On the basement membrane, viral particles bind to their primary attachment site, heparan sulfate (HS) within the extracellular matrix (ECM). This binding triggers a series of conformational changes which promote viral cell entry, with virions migrating along actin-rich protrusions to engage a yet uncharacterized secondary receptor complex on keratinocytes. Current evidence suggests that this secondary receptor is likely a multimeric complex rather than a single molecular entity. Several proteins have been implicated as essential for cell entry, including the tetraspanin CD151, integrin-α6 (Itgα6), growth factor receptors (GFRs), and the annexin A2 heterotetramer. Among these, CD151 plays a crucial role in facilitating viral access and organizing the cellular components necessary for successful infection. However, this multistep entry process is slow and asynchronous, and involvement of CD151 in HPV entry prior to endocytosis remains unclear.

In this study, HPV16 pseudovirions (PsVs) were used to investigate early infection stages and their association with CD151. PsV/CD151 assemblies were analyzed, revealing that PsVs preferentially bind to regions with increased CD151 density. Overexpression of CD151-GFP induced the formation of large CD151 aggregates, although these aggregates also form independently of PsV binding, indicating that aggregate formation depends on CD151 expression levels.

Furthermore, the actin inhibitor cytochalasin D (CytD) was employed to synchronize PsV uptake, revealing that actin dynamics within filopodia are crucial for releasing virions from the ECM and transferring them to the cell body. The human keratinocyte cell line HaCaT was validated as an ideal model system for studying early HPV infection events, due to its robust ECM production and restricted entry receptor expression primarily at the substrate-adhered basal membrane, closely mimicking *in vivo* conditions. Inhibition of actin-dependent processes resulted in entrapment of PsVs in the ECM. Upon removal of this blockade, HS-coated PsVs rapidly translocated to the cell body and to CD151 assemblies. After reaching the cell body, the viral capsid sheds its HS coat, followed by PsV/CD151 endocytosis. These findings demonstrate an early involvement of CD151 in HPV16 cell entry, where PsVs bind to preformed CD151 assemblies post-translocation from the ECM.

Moreover, the heparan sulfate proteoglycan (HSPG) -binding peptide 19-2.5 was evaluated for its potential to inhibit PsV infection. While peptide 19-2.5 did not affect PsV/CD151 association, it caused the formation of large viral aggregates several micrometers away from the plasma membrane, indicating a block in the translocation from the primary HSPG attachment site to the secondary receptor complex. This suggests that peptide 19-2.5 may serve as a promising alternative or complement to current HPV prevention strategies.

In conclusion, a rapid initial step in the HPV infection cascade has been identified, involving the transfer of HS-coated virions from the ECM to CD151 on the cell body. This step, however, occurs rapidly and thus does not explain the asynchronous uptake of HPVs. The peptide 19-2.5 can interfere with this translocation process, thereby preventing HPV infection.

2. Introduction

2.1 Viruses

Viruses are the most abundant and diverse biological entities in the biosphere. They are genetic parasites and rely on the protein synthetic machinery of the host to reproduce, as they lack the cellular structures and metabolic machinery necessary for independent existence. Therefore, viruses are not considered to be living organisms (Ramirez-Martínez, 2024, Ritsch et al., 2023, Taylor, 2014). They are composed of genetic material, either single- or double-stranded DNA or RNA in a linear, circular, or segmented form, enclosed in a protein shell, called viral capsid. Additionally, some viruses can have an envelope composed of lipids and viral proteins. The viral replication strategies vary widely, from RNA-dependent RNA synthesis, as seen in influenza and coronaviruses, to reverse transcription in retroviruses like human immunodeficiency virus (HIV), and DNA-based replication in herpesviruses and poxviruses (Domingo, 2020).

Recent advances in genomics and next-generation sequencing have expanded knowledge of viruses, revealing a vast and mostly unexplored diversity (Lauber, Seitz, 2022). Viruses can be found in soil, extreme environments, ubiquitously in oceans, and even in the air. This diversity is not only reflected in their vast array of shapes and genetic compositions, but also in the essential ecological and evolutionary roles they play, ranging from drivers of genetic innovation through horizontal gene transfer to modulators of host population dynamics. The enormous abundance and rapid evolutionary rates of viruses mean that they can adapt quickly to selective pressures, such as new hosts and environments, thus shaping both evolutionary trajectories and the emergence of new infectious diseases (Domingo, 2020, Ramirez-Martínez, 2024, Ritsch et al., 2023).

Viruses infect a diverse range of hosts, spanning nearly every form of life, including animals, plants, fungi, bacteria, and archaea. This broad host spectrum is driven by the capacity of the virus to recognize and enter specific host cells, mediated by surface receptors that differ among species, and by the ability to replicate efficiently within the cellular environment of the host. The spectrum of host species or cell types that can be infected by a virus, the so-called host-range or host-tropism of a virus, varies widely among viruses (Fermin, 2018). Some viruses, known as specialists, exhibit a narrow host range infecting only one or a few closely related species. The dengue virus, for example, primarily infects humans (Rothman, 2011). Other Viruses are generalists with a broad host range, capable of infecting multiple species across different taxonomic groups. A notable example is the influenza A virus, which infects birds and various mammals, reflecting its ability to cross species barriers and cause zoonotic infections (Fermin, 2018, Rumschlag-Booms, Rong, 2013). The complexity of host-virus interactions influences conditions such as host susceptibility and virus transmission dynamics in

natural and clinical settings. Transmission barriers, vector behaviors, and environmental factors can restrict or extend the effective host range of a virus. This leads to phenomena like '*spillover*' events whereby viruses infect alternative or novel hosts unexpectedly. These '*spillover*' events are particularly significant for public health, as they can lead to emerging infectious diseases when viruses adapt to become efficiently transmissible in new host populations (Fermin, 2018). An important and notable example of a '*spillover*' event is severe acute respiratory syndrome coronavirus 2 (SARS-CoV-2), which had a tremendous impact on global public health (Sparrer et al., 2023).

2.2 Human Papillomaviruses

Human papillomaviruses (HPV) are a diverse group of non-enveloped, double-stranded DNA viruses with profound significance in human health. The HPV genome consists of circular double-stranded DNA with a size of approximately 7.9 kb in length. The genome encodes two sets of conserved core proteins. The non-structural proteins E1 and E2 are required for viral DNA replication and the structural proteins L1 and L2 are essential for virion assembly (McBride, 2017). Over 200 types of human papillomaviruses are known to date. HPVs are phylogenetically classified into five genera (*Alpha*, *Beta*, *Gamma*, *Mu*, and *Nu*) based on DNA sequence homology in the L1 gene (Villiers et al., 2004). Many HPV genera developed a preference for specific anatomical regions or cells of the host epithelium (Schiffman et al., 2016). Whereas viruses within the *Alpha* genus infect both cutaneous and mucosal epithelia, viruses within the *Beta*, *Gamma*, *Mu*, and *Nu* genera only infect the cutaneous epithelium (Della Fera et al., 2021, Doorbar et al., 2015). HPV genotypes are divided into high-risk HPV and low-risk HPV depending on their oncogenicity (Aranda-Rivera et al., 2021, McBride, 2022). Low-risk HPV like HPV6 and HPV11 cause benign lesions such as oral focal hyperplasia and anogenital warts, whereas high-risk HPV like HPV16 and HPV18 cause precancerous lesions, that can evolve into various cancers (Zhang et al., 2025).

HPVs are about 55 nm in size, and the capsid has an icosahedral structure. The viral capsid is composed of 72 pentameric capsomers (Figure 1) assembled primarily from 360 copies of the major capsid protein L1 with a smaller contribution from the minor capsid protein L2 (Buck et al., 2008, Finch, Klug, 1965). A total of 12 pentavalent capsomers of the viral particle each have 5-fold symmetry and are surrounded by 5 neighboring capsomers. Additionally, a viral particle is composed of 60 hexavalent capsomers with a pseudo-6-fold symmetry. Each of the hexavalent capsomers is surrounded by 6 neighboring capsomers that are not evenly spaced. A loop of the C-terminus of every copy of L1 forms a connection to a neighboring capsomer by forming a stabilized disulfide bond (Baker et al., 1991, Hartmann et al., 2021). The number and positioning of L2 proteins within the capsid is still unknown. However, it has been proposed that the L2 protein binds in the center of the capsomer, exposing part of its N-terminus on the surface (Lowe et al., 2008). While some stoichiometric studies assume that a

HPV capsid has between 12 and 36 L2 molecules (Okun et al., 2001), other studies have suggested an amount of up to 72 L2 molecules per capsid, one within each capsomer (Buck et al., 2008, Doorbar, Gallimore, 1987, Goetschius et al., 2021, Trus et al., 1997).

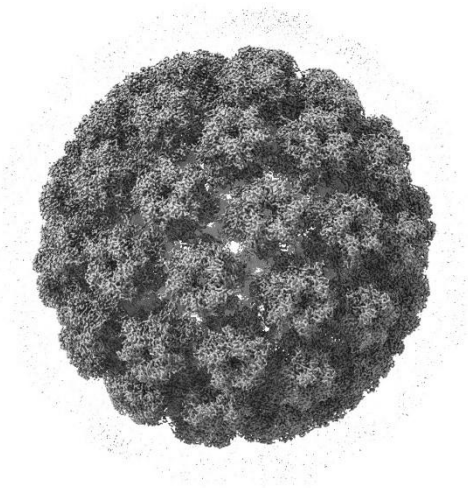

Figure 1. HPV16 capsid reconstruction from a high-resolution cryo EM micrograph.
An example of a 3D surface rendered model of a viral particle oriented in the x-axis. Figure taken and modified from reference (Goetschius et al., 2021).

The papillomavirus genome (Figure 2) is composed of three distinct regions separated by two polyadenylation (pA) signals, referred to as viral early (pA_E) and viral late (pA_L) signals. The three regions are early (E) and late (L) gene regions, as well as an upstream regulatory region (URR). The URR is also known as long control region (LCR) and does not encode any proteins. It is located between the L1 and E6 open reading frames (ORFs) and involved in transcription and replication (Yu et al., 2022). Additionally, the URR contains the single origin of replication (Ori) responsible for viral DNA replication. The early region genes encode for seven non-structural proteins: E1, E2, E1^E4, E5, E6, E7, and E8^E2. E1 and E2 are essential for HPV DNA replication. The protein E1 is a viral Ori-binding DNA helicase and the protein E2 is an E1 accessory protein. Additionally, the E2 protein acts either as a viral transcriptional activator or as a repressor, depending on its binding site. It also plays a role in the virus genome segregation during mitosis (McBride et al., 2006, Yu et al., 2022, zur Hausen, 2002). The protein E1^E4 is expressed in the late stage of infection and facilitates the viral release by interfering with the cytokeratin network of the host (Doorbar et al., 1991, McIntosh et al., 2010). The proteins E6 and E7 are viral accessory proteins targeting several oncogenic and tumor suppressor proteins and miRNAs. Thereby, they circumvent cell cycle checkpoints and induce cell transformation and immortalization (Roman, Munger, 2013, Vande Pol, Klingelhutz, 2013, Zheng, Wang, 2011). The E8^E2

protein inhibits viral genome replication and viral gene expression (Dreer et al., 2017, Yu et al., 2022). The expression of the two capsid proteins L1 and L2 occurs during the late stage of infection and is induced by viral vegetative DNA replication. Additionally, it is restricted to the terminally or highly differentiated epithelial cells (Wang et al., 2017, Woodham et al., 2012).

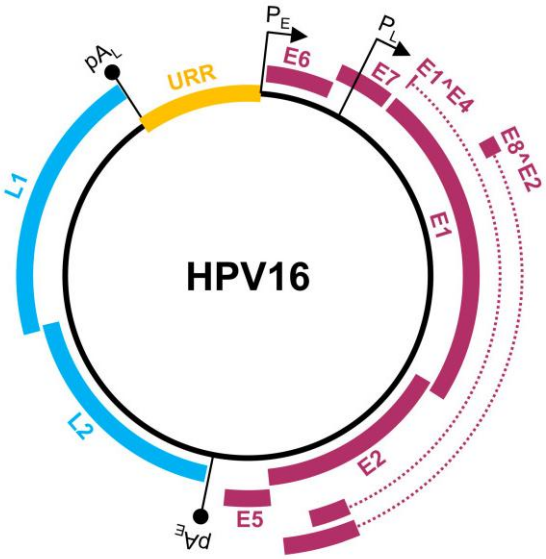

Figure 2. HPV16 genome and annotated ORFs.
The non-structural proteins from the early region of the genome, including E1, E2, E1^E4 (E4), E5, E6, E7, and E8^E2, are shown in purple. The viral capsid proteins, L1 and L2, from the late region of the genome are shown in blue. URR (yellow), upstream regulatory region. P_E and P_L mark the early and late promoters, and pA_E and pA_L stand for the early and late polyadenylation sites. Figure and legend taken and modified from reference (Yu et al., 2022).

2.3 Life cycle of HPV

Papillomaviruses have developed a highly specialized infection strategy that exploits the natural self-renewal cycle of stratified cutaneous and mucosal epithelia. In these epithelial tissues, basal cells anchored to the basement membrane divide either symmetrically, producing additional basal cells, or asymmetrically, where a daughter cell migrates upward toward the surface as part of tissue turnover. In the latter pathway, migrating cells progress through layers of the epithelium, undergoing distinct stages of differentiation before eventually being shed from the tissue surface. Papillomaviruses infiltrate the basal layer via small epithelial injuries, establishing a slow but persistent infection (Figure 3). Within these basal cells, the viral genome remains extrachromosomal and at a low copy number, with minimal transcriptional activity. As infected cells ascend and differentiate, viral DNA replication and gene expression sharply increase. By restricting active replication to terminally differentiated cells

outside the reach of immune surveillance, the virus effectively minimizes detection and evades immune responses (Della Fera et al., 2021, McBride, 2017, Stanley, 2012).

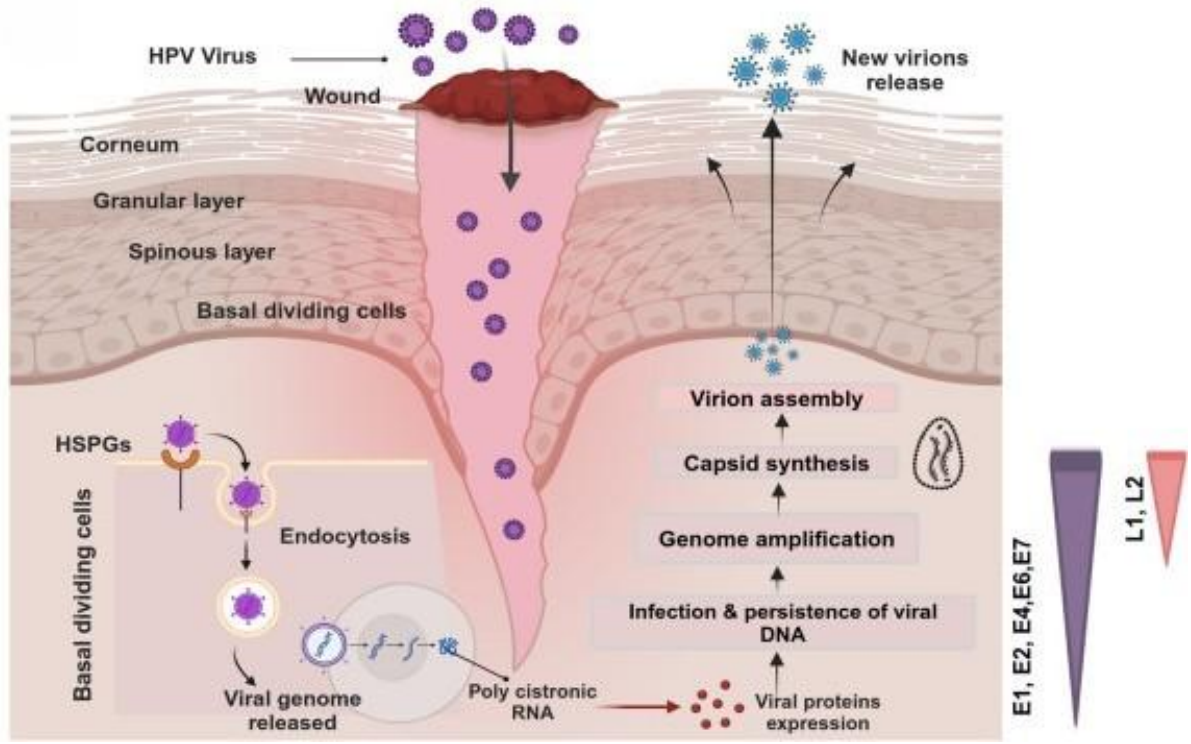

Figure 3. HPV infectious life cycle.
Schematic representation of the differentiated layers of a stratified epithelium infected with HPV. The virus must access the basal keratinocytes through a break in the epithelial barrier. After cell entry, the virus is trafficked through the endosome to the nucleus. After uncoating, the viral genome (in complex with the L2 protein) relies on a breakdown of the nuclear membrane during mitosis to gain entry to the nucleus. Within the nucleus, HPV genomes undergo a limited round amplification. Afterwards, they become established by attachment to host chromatin to maintain the viral genome at a constant copy number in dividing cells. Upon epithelial differentiation, infected cells amplify the viral DNA to high copy numbers, and late viral genes are expressed for virion assembly and packaging. Virions are shed from the epithelium in viral-laden squames. The viral protein expression levels are indicated on the right. Figure and legend taken and modified from reference (Baba et al., 2025).

For infection, virions must reach the dividing basal cells of the lower epithelium through a break in the epithelial barrier. On the basement membrane, viral particles bind to their primary attachment site, heparan sulfate proteoglycans (HSPGs). Afterwards, virions translocate to an uncharacterized secondary receptor on keratinocytes and induce a series of conformational changes to promote viral cell entry (Day, Schelhaas, 2014). During endocytosis the L2 minor capsid protein inserts into the membrane and covers the virus in a membrane vesicle to enter basal keratinocytes (DiGiuseppe et al., 2016). Within the cell, HPV is transported to the trans Golgi network subsequent to L2 association with cytoplasmic trafficking factors. Here, the virus resides until it gains access to the host nucleus (Calton et al., 2017). The vesicle enters the nucleus after a breakdown of the nuclear envelope during

mitosis and associates with condensed mitotic chromosomes. A central region of the L2 protein mediates the tethering of the viral genome (Aydin et al., 2014, Aydin et al., 2017). The vesicle containing HPV stays attached to the host chromosomes throughout mitosis until the nuclear envelope is restored (Della Fera et al., 2021).

Within the nucleus the viral DNA localizes to promyelocytic leukemia nuclear bodies (PML-NBs) where viral transcription and DNA replication is presumably initiated. Although host PML-NBs typically restrict gene expression in most DNA viruses, effective transcription of the HPV genome depends on PML-NBs and the displacement of the resident protein Sp100. Consequently, HPV exploits certain components of PML-NBs while avoiding others to promote a productive infection (Guion et al., 2019).

The HPV genome uses three distinct phases of DNA replication. These stages are initial amplification, maintenance, and vegetative amplification. During the initial amplification phase, the viral genome replicates a few times to establish a small pool of extrachromosomal genomes that persist in the self-renewing basal cells of the lower epithelium. These infected basal cells form the foundation of the lesion and function as a long-term reservoir for persistent HPV infection. In the maintenance phase, which occurs in proliferating cells, the extrachromosomal viral genomes replicate alongside host DNA and remain tethered to host chromatin to ensure equal segregation into daughter cells. The viral copy number stays constant until the infected cells begin to differentiate and migrate toward the epithelial surface, triggering late viral gene expression and extensive vegetative DNA amplification (Della Fera et al., 2021).

As keratinocytes undergo differentiation, a late promoter located within the E7 gene is activated, leading to elevated expression of the E1 and E2 proteins as well as late gene products such as E1^E4 (E4), L1, and L2. Production of late transcripts containing L1 and L2 relies on alternative splicing and recognition of alternate polyadenylation sites (Graham, 2017a). Ultimately, the viral genome is packaged, and new viral progeny is released within squames shed from the epithelial surface (Doorbar et al., 2015).

2.4 HPV mediated cancers

High-risk HPVs are known for their ability to cause cancers. About 5% of all human cancers are caused by HPV (Martel et al., 2017). HPV16 contributes to 87% of global oropharyngeal squamous cell carcinoma cases (Kreimer et al., 2005, Lu et al., 2022) and both, HPV16 and HPV18, are associated with more than 70% of cervical cancer cases (Tommasino, 2014). A clear correlation exists between HPV infection severity, lesion intensity, and the prevalence of oncogenic HPV genotypes. Oncogenic HPV genotypes have been suggested to play a role in the development of various cancers, including cervical cancer, head and neck squamous cell carcinoma, anal cancer, and more rare malignancies

such as penile, vaginal, and vulvar cancers (Baba et al., 2025, Plummer et al., 2016). Chronic high-risk HPV infections are estimated to be the cause of 90% of cervical and anal cancers, 70% of vulvar and vaginal cancers, 60% of penile cancers, and 70% of oropharyngeal cancers (Baba et al., 2025, Szymonowicz, Chen, 2020).

Both, men and women can be affected by HPV infection and over 80% of sexually active individuals are estimated to have contracted HPV by the age of 45 (Tao et al., 2022). It is assumed that 90% of HPV infections resolve within an average of two years (Shanmugasundaram, You, 2017). However, a persistent infection of epithelial stem and basal cells is assumed to be a main factor leading to cancer development (Moody, Laimins, 2010). The onset and progression of malignancies is facilitated by the integration of the viral genome within the host genome during persistent infections. This leads to a modification of the host cell condition. During the integration of the HPV genome (Figure 4), the deletion of large segments of viral DNA and the disruption of the E2 gene can occur whereas the E6 and E7 genes remain intact. As E2 functions as repressor that negatively regulates E6 and E7 expression its disruption together with alterations to cellular promotor elements can result in an increased expression of E6 and E7 (Baba et al., 2025, Yu et al., 2024). The increased expression of E6 and E7 is often a critical alteration needed for the progression of infection to malignancy (Münger et al., 1989) as overexpressed E6 and E7 activity interfere with the transcription of tumor suppressor genes such as p53 and Rb. Additionally, E6 and E7 activity is responsible for inhibited differentiation, chromosomal instability and promotes cell proliferation ultimately increasing the risk of malignancies (Graham, 2017b).

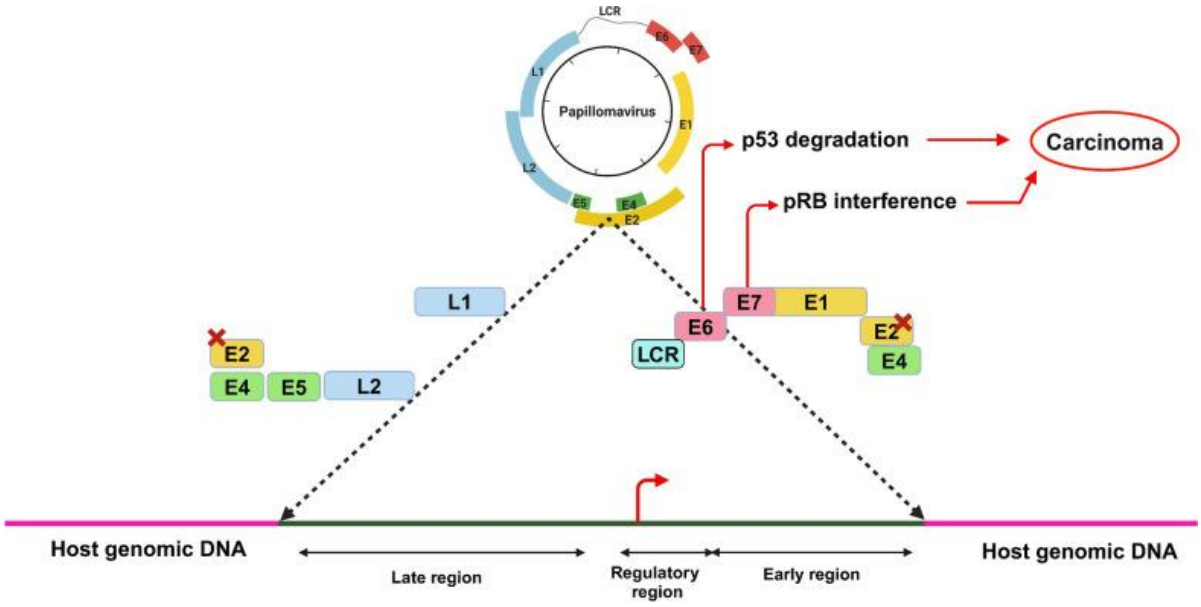

Figure 4. Schematic of the integration of the HPV genome into the host genome.
Integration of the HPV genome into the host genome induces disruption of the E2 gene, leading to the consecutive expression of the oncogenes E6 and E7, resulting in induced cellular immortalization,

transformation, and, ultimately, carcinoma. Figure and legend taken and modified from reference (Baba et al., 2025).

2.5 Therapeutic strategies to prevent HPV mediated carcinomas

Therapeutic approaches to prevent HPV infection have become a central focus in the effort to reduce global cervical cancer rates and related diseases. Different therapeutic approaches (Figure 5) and strategies to target oncoproteins in cancers as well as vaccinations against HPV are available to date. These potential targets and biomarkers present opportunities to reduce the global impact of HPV-related cancers through early intervention, personalized therapeutic strategies, and potentially curative treatments. However, early diagnosis of HPV is crucial to manage and prevent cancer causing HPV infections. Therefore, regular screening is essential to monitor HPV-related lesions (Boccardo, 2021).

Whereas secondary prevention, such as screening for cervical abnormalities and early intervention, reduces cancer burden, primary prevention, especially at the level of infection, is regarded as the most effective and cost-efficient public health approach (Mahajan et al., 2024). The most effective prophylactic tool against HPV infection is vaccination. Currently, there are safe and effective bivalent, quadrivalent and nonavalent vaccines available which have an efficacy of 90–99% against HPV when vaccination coverage is high (Aggarwal et al., 2023). Vaccines are based on virus-like particles (VLPs) that mimic the native structure of the viral capsid, without containing viral DNA. VLPs are considered to be non-infectious and safe for use. Upon administration, they induce robust neutralizing antibody responses capable of blocking viral attachment and entry. These vaccines are recommended for pre-adolescent females and males, ideally before the onset of sexual activity. (Mahajan et al., 2024, Ni et al., 2025). However, vaccinations are costly and vaccination rates are still low especially in low- and middle-income countries as disparities in global access remain a challenge (Ebrahimi et al., 2023).

Several other inexpensive and accessible alternatives like topical gels and lubricated condoms can provide additional preventive strategies. Additionally, clinical trials with a carrageenan-based gel revealed an efficient reduction of genital HPV infections (Laurie et al., 2023). Antiviral peptides capable of targeting several stages of viral infection are another promising therapeutic approach (Mikuličić et al., 2025, Vilas Boas et al., 2019). The combination of these topical or locally active agents with vaccination may provide enhanced protection, especially in populations with low vaccine rates.

Despite advances in vaccines and antiviral agents, screening for cervical precancerous lesions remains a crucial secondary prevention. Techniques range from cytology (Pap tests) to HPV DNA testing and visual inspection. Early detection allows for timely intervention and prevents the progression of a persistent infection to invasive cancer. However, in many settings, challenges related to participation

rates, cost, and infrastructure persist (Chen et al., 2025, Mo et al., 2022). For established precancerous lesions, surgical excision is recommended. Patients with milder changes may be managed with surveillance alone, while more advanced diseases may require multimodal therapy including surgery, chemotherapy, and radiotherapy (Ni et al., 2025). As high-risk HPV early proteins E6 and E7 play a major role in initiating HPV-mediated carcinoma, therapeutic strategies targeting those oncogenic proteins are another secondary prevention approach (Pang, Thierry, 2013). Additional secondary prevention strategies are utilizing genome editing technology such as CRISPR/Cas9 to suppress E6 and E7 expressions in cervical cancer (Ling et al., 2020) and anti-tumor immunity offered by tumor-infiltrating lymphocyte therapy (TIL therapy) (Stevanović et al., 2015).

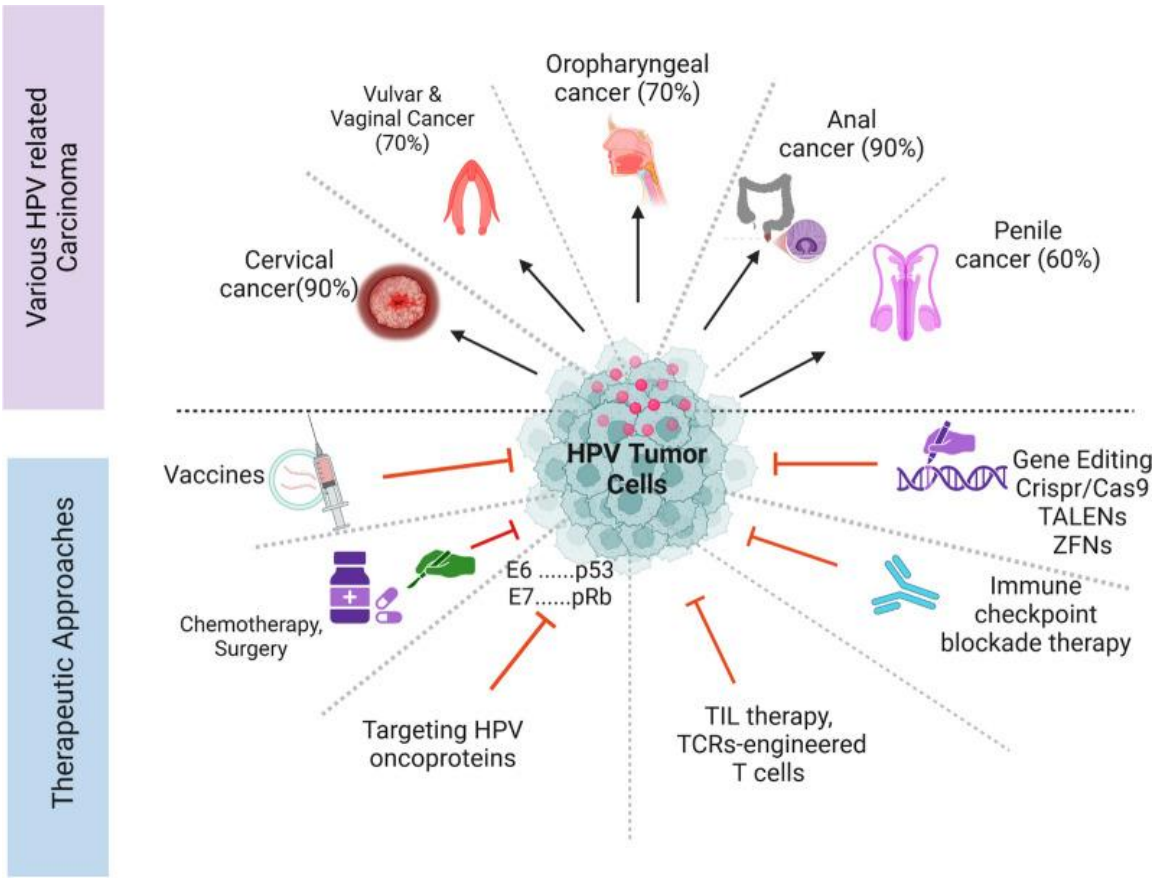

Figure 5. HPV related carcinoma and therapeutic strategies.
Depiction of HPV-related cancers comparing percentages of HPV-associated and other causes with an additional depiction of therapeutic approaches. Figure and legend taken and modified from reference (Baba et al., 2025).

2.6 Cell entry events in HPV infection

From most pathogenic lesions and organotypic (raft) epithelial tissue cultures only a small amount of HPV particles can be obtained. Therefore, the vast majority of the current knowledge of viral entry results from reductionist approaches studying laboratory-derived pseudovirion (PsV) interactions with

cultured cells in monolayers. In these approaches, PsVs consists of the L1/L2 capsid encapsidating a reporter gene plasmid instead of the viral genome. It is assumed that PsVs are structurally and immunologically indistinguishable from lesion- and tissue-derived HPVs (Ozbun, Campos, 2021). However, the entry of HPV PsVs is unusually asynchronous in cultured keratinocytes. While some PsVs enter the cells within minutes it can take up to several hours for the remaining PsVs on the cell surface to enter the cell (Becker et al., 2018, Ozbun, Campos, 2021).

For HPV infection (Figure 6), a disruption of the epithelial barrier is a prerequisite, as HPV uptake relies on mitotically active basal cells of the epithelium (Ozbun, 2019). Virions primary attach to linear polysaccharide HS in the ECM and on the cell surface. Virions can also bind to cell-free HS and/or syndecan (Sdc) HSPG ectodomains attached to laminin 322 (LN332) within the ECM or directly to LN332 in the ECM (Culp et al., 2006, Giroglou et al., 2001, Joyce et al., 1999, Richards et al., 2013, Surviladze et al., 2015). Binding is facilitated by positively charged and polar residues of the L1 capsid protein interacting with negatively charged HS resulting in a strong electrostatic bond (Dasgupta et al., 2011, Giroglou et al., 2001, Joyce et al., 1999, Knappe et al., 2007, Surviladze et al., 2015). *In vitro*, virions can freely bind to HS on the ECM and the cell surface, whereas *in vivo* virions may predominantly bind to HS of the extracellular basement membrane (Day, Schelhaas, 2014, Kines et al., 2009, Ozbun, Campos, 2021, Schiller et al., 2010). Before virions translocate to a still unknown secondary receptor on the cell surface, the strong bond between virions and the primary attachment site must be disrupted (Ozbun, Campos, 2021). However, the strong bond excludes a simple dissociation between virions and HS. To date, two mutually not exclusive release mechanisms are discussed.

In one model, the so-called priming model, the viral capsid is enlarged after binding to HS (Feng et al., 2024). Thereby, L1 is exposed and cleaved by kallikrein-8 (KLK8) (Cerqueira et al., 2015), following L2 exposure by cyclophilin (Bienkowska-Haba et al., 2009) and a subsequent L2 cleavage by furin (Richards et al., 2006). The now primed virion can bind to the secondary receptor.

In the second model, the virions remain associated with HS. Cleavage of HS/HSPGs by heparanases and proteinases produces HS fragments that are still bound to the virion surface but not to the ECM. However, the virion is no longer anchored to the ECM by the fragmented HS (Surviladze et al., 2012, Surviladze et al., 2015). Additionally, bioactive molecules including growth factors (GF) may bind to viral particles. The now released virion can reach the cell surface by diffusion. Indeed, in a co-culture trans-well assay, PsVs from donor cells were able to infect spatially separated receiver cells, indicating that diffusion may be sufficient for infection (Surviladze et al., 2012).

Nevertheless, several studies report an active transport mechanism, where virions migrate along actin-rich protrusions from the ECM toward the cell body (Schelhaas et al., 2008, Smith et al., 2008).

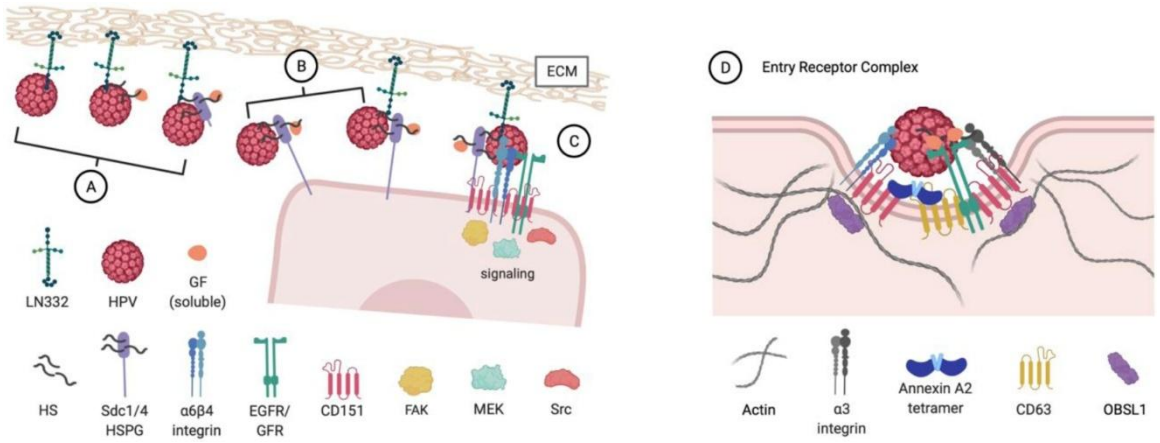

Figure 6. Extracellular interactions of HPV on human keratinocytes.
(A) HPV particles can bind to shed HS and/or Sdc HSPG ectodomains attached to laminin 322 (LN332) or directly to LN332 in the ECM. Viral particles may remain inert until they are released by enzymes and/or transferred to active filopodia for transport to the cell body. (B) HPV particles can attach to plasma membrane-resident Sdc HSPGs. Afterwards, they await ectodomain shedding by MMPs and ADAMs or HS processing by heparinase to release soluble HPV/HS/GF complexes that translocate to uptake receptor complexes. (C) LN332 interacts with Sdc1, CD151 and α6β4 integrin on the basal cell to provide cell anchorage to the ECM/basement membrane, termed the hemidesmosome. Sdc-1 and Sdc-4 capture EGFR family members and integrins via binding sites in their ectodomains and thereby, may provide rapid signaling and recruitment of uptake complexes for some incoming virions. Signaling is facilitated via focal adhesion kinase (FAK), mitogen-activated protein kinase kinase (MEK), or/and Src kinase (Src). (D) The HPV entry receptor complex consists of CD151 and EGFR, and potentially CD63, integrins, and A2t. Currently, potential roles of Sdc, HS and GF during entry are unclear. The cytosolic obscurin-like 1 protein (OBSL1) adaptor potentially links the complex to the actin cytoskeleton for endocytosis. Figure and legend taken and modified from reference (Ozbun, Campos, 2021).

The secondary receptor on the cell body surface is still unknown. However, it is currently assumed that the secondary receptor is most likely a multimeric complex rather than a single molecular component. Several proteins have been indicated to play a crucial role for cell entry such as the tetraspanin CD151 (Mikuličić et al., 2019, Scheffer et al., 2013, Spoden et al., 2008), integrin-α6 (Itgα6) (Evander et al., 1997, Yoon et al., 2001), growth factor receptors (GFRs) (Mikuličić et al., 2019, Surviladze et al., 2012), and the annexin A2 heterotetramer (Dziduszko, Ozbun, 2013, Woodham et al., 2012). It is assumed that the obscurin-like 1 adaptor protein (OBSL1) links the entry complex to the actin cytoskeleton for endocytic uptake (Wüstenhagen et al., 2016).

2.7 Tetraspanins in viral infection

The process by which viruses infiltrate host cells is a highly regulated event depending on a series of sequential interactions. Latest research revealed the pivotal contributions of tetraspanin-enriched microdomains (TEMs) in mediating the entry of diverse viruses into their target cells. Among the tetraspanin family, the protein CD151 stands out for its crucial role in facilitating viral access and organizing the multiple cellular components necessary for successful infection, particularly for viruses

such as HPV, human cytomegalovirus (HCMV), coronavirus, HIV, hepatitis C virus, and influenza virus (Bruening et al., 2018, Earnest et al., 2015, Florin, Lang, 2018, Hantak et al., 2019, Hochdorfer et al., 2016, Scheffer et al., 2013, Zona et al., 2013).

Tetraspanins are known as 'cluster of differentiation' (CD) molecules with a nomenclature that, however, does not refer to their function (Charrin et al., 2014, Schmidt et al., 2024). They are small transmembrane proteins (Figure 7) with four transmembrane domains linked extracellularly by one large and one small extracellular loop (termed LEL and SEL, respectively), widely expressed across eukaryotes. Mostly, they assemble into platforms with other tetraspanins, integrins, and adhesion molecules, creating microdomains on the plasma membrane (Hantak et al., 2019). These highly organized assemblies build up an interacting network the 'tetraspanin web' (Charrin et al., 2009).

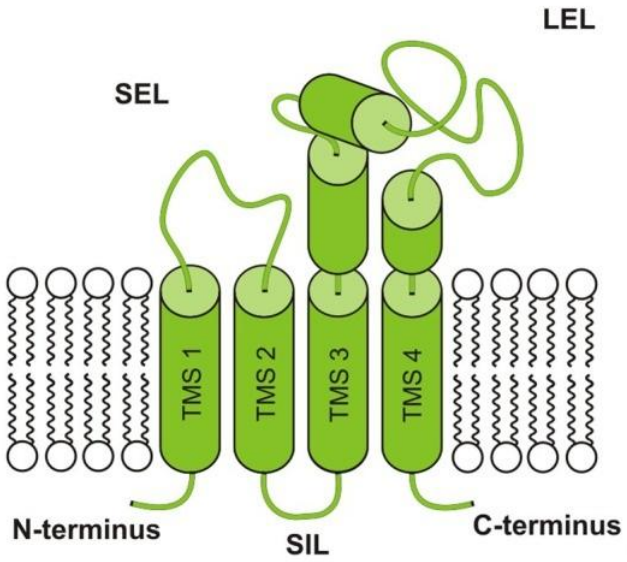

Figure 7. Topology of tetraspanins.
Depicted is the typical topology of a tetraspanin. Tetraspanins are composed of four transmembrane segments (TMS1, TMS2, TMS3, and TMS4). The intracellular site includes the N-terminus, the small intracellular loop (SIL), and the C-terminus. At the extracellular site, a small extracellular loop (SEL) connects TMS1 and TMS2 and a large extracellular loop (LEL) connects TMS3 and TMS4. Figure and legend taken and modified from reference (Hochheimer et al., 2019).

Tetraspanins have distinct functions during the viral cell entry and infection (Figure 8). TEMs recruit different proteins required for viral recognition and attachment to the cell surface. For example, HPV16 depends on the recruitment of integrins and GFRs to TEMs by CD151. The spatial proximity induced by CD151 is a precursory step for the internalization of HPV16 (Finke et al., 2020b, Florin, Lang, 2018, Hemler, 2001). After virus binding, TEMs coordinate the internalization steps, including

endocytosis and membrane fusion. During HPV16 internalization, viral particles colocalize with locally enriched CD151 and CD63 on the plasma membrane. Enriched CD151 and CD63 at HPV16 sites can be observed during invagination and in endosomes (Scheffer et al., 2014, Spoden et al., 2008). Additionally, TEMs guide intracellular trafficking and help traffic viral particles within transport vesicles toward productive infection. During cell entry, many viruses such as HPV, localize to endosomes that are enriched with CD63. In complex with syntenin-1, CD63 is responsible for HPV trafficking to multivesicular bodies (MVB) where viral capsid disassembly takes place (Gräßel et al., 2016).

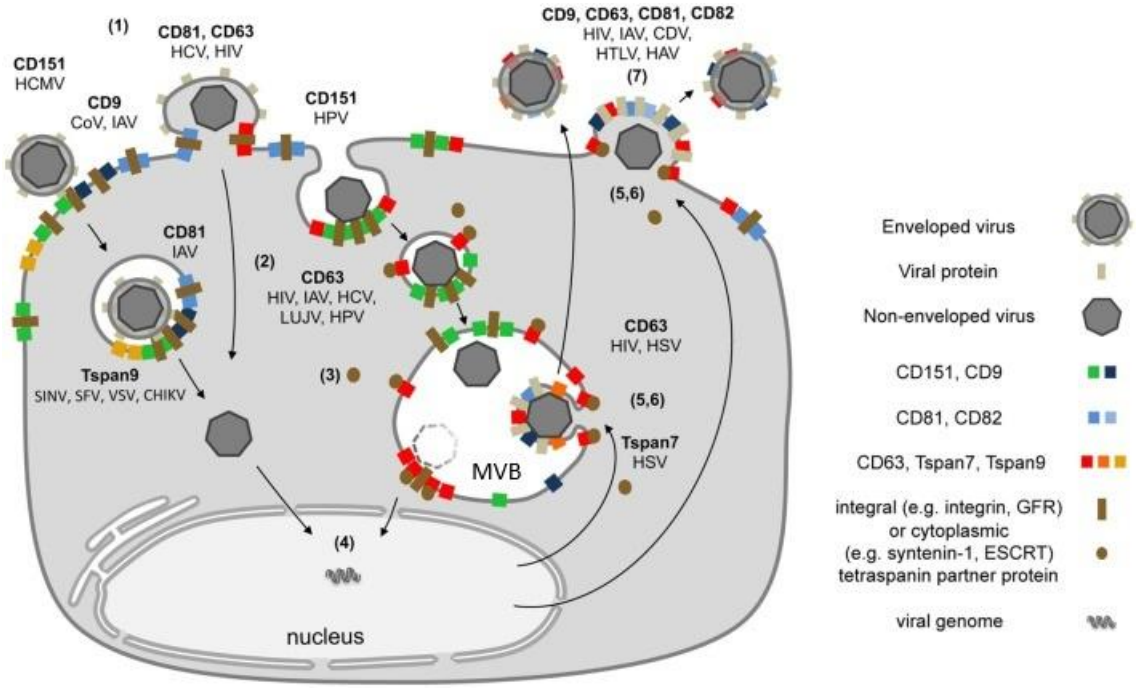

Figure 8. Schematic model of tetraspanins involved in viral infection.
(1) Viral particles interact with entry receptors at tetraspanin clusters and thereby trigger the formation of larger cluster networks. (2) Viral internalization is promoted by tetraspanin assemblies and endocytosis/fusion occurs. (3) After endocytosis, virus particles in transport vesicles are intracellular trafficked. In this step, tetraspanins mediate and organize interactions with cytoplasmic trafficking molecules. (4) Delivery of viral genomes into the cytoplasm or the nucleus resulting in successful infection. (5) Morphogenesis of enveloped viruses on TEMs. (6) Viral proteins are integrated into tetraspanin clusters. This induces spatial enrichment of other tetraspanins and viral proteins. (7) The resulting high concentration of virus envelope components enables efficient budding and release. Figure and legend taken and modified from reference (Florin, Lang, 2018).

2.8 Actin dynamics in viral infection

The actin cytoskeleton is a dynamic network of filaments critical for shaping the cell, enabling movement, and directing intracellular traffic. Many viruses, including HPV16, have evolved highly specialized mechanisms to hijack and reprogram the actin cytoskeleton at multiple stages of their infection cycle (Bienkowska-Haba, Sapp, 2011, Kloc et al., 2022, Taylor et al., 2011). Actin is the most abundant protein in eukaryotic cells, assembling into microfilaments through dynamic cycles of

polymerization and depolymerization. This remodeling enables: cell shape changes, formation of membrane protrusions such as filopodia and lamellipodia, endocytosis and phagocytosis, as well as intracellular trafficking and signaling (Taylor et al., 2011). Viruses exploit these capabilities to attach, internalize, and move within a cell. Additionally, viruses exploit these capabilities for cell exit. Many viruses interact directly or indirectly with the actin cytoskeleton. For instance, manipulation of actin polymerization drives viral entry via endocytic pathways, promotes transport inside the cell, and facilitates cell exit. In some cases, viral proteins subvert actin-related signaling pathways, while in others, the viruses stimulate membrane protrusions or reorganize cortical actin to create platforms for cellular invasion (Kloc et al., 2022, Taylor et al., 2011).

Entry of HPV16 into host cells is a multi-step process requiring active remodeling of the actin cytoskeleton. During this process, HPV16 utilizes a non-canonical actin-driven endocytic pathway that is independent of clathrin, caveolin, and dynamin (Mikuličić et al., 2021). Research revealed that actin polymerization is critical for HPV16 infection. Inhibitors that disrupt actin filaments (cytochalasin D) or stabilize actin excessively (jasplakinolide) strongly block HPV16 infection. Additionally, HPV entry relies on actin dynamics and not classic GTPase regulation. It has been shown, that this pathway does not require signaling through Rho-family GTPases (such as RhoA, Rac1, Cdc42) or Arf6, all of which are typical controllers of actin polymerization and endocytosis. However, the entry process is sensitive to inhibition of the Na^+/H^+ exchanger, implying features reminiscent of micropinocytosis (Schelhaas et al., 2012). Recent research highlights the importance of the key actin nucleation promoting factors Wiskott–Aldrich syndrome protein family verprolin-homologous proteins 1 and 2 (WAVE1 and WAVE2) during HPV16 infection. WAVE1 and WAVE2 mediate local actin protrusions at the plasma membrane upon addition of HPV16 PsVs. Thus, WAVE1/2 mediate a key step prior to HPV entry into cells that involves actin reorganization in the form of cellular dorsal surface protrusions (Fernandez et al., 2025). HPV16 is transported along actin-rich filopodial extensions by actin retrograde flow (Schelhaas et al., 2008). Actin retrograde flow is the movement of actin from the cellular periphery toward the cell body. It is the result of three activities: polymerization of actin at the tip, retrograde transport mediated by the anchored motor protein myosin II, and actin depolymerization at the cell body (Bienkowska-Haba, Sapp, 2011).

HPV16 entry complexes at the cell surface are composed of clusters of tetraspanins, integrins, actin, and other linker proteins such as OBSL1. This organization may link the plasma membrane to the underlying cytoskeleton, facilitating viral uptake and movement into endocytic vesicles (Finke et al., 2020b, Finke et al., 2020a). While actin polymerization is most crucial for entry, the cytoskeleton continues to influence endocytosis and intracellular trafficking. Mechanistically, actin polymerization facilitates vesicle scission and is driven by the nucleation-promoting factor WASH. Although WASH

commonly functions with the retromer complex on endosomes during retrograde trafficking, the formation of endocytic vesicles upon HPV16 infection occurs largely independent of both the retromer and its membrane-bending SNX-BAR adaptor. Therefore, WASH functions not only in intracellular membrane trafficking but also plays a distinct role during HPV16 endocytosis (Brinkert et al., 2025).

2.9 Aim of the study

The binding and internalization of human papillomaviruses at the cell surface is a complex, multi-step process that is not completely understood. Numerous host cell factors such as HSPGs, CD151, integrins, GFRs and actin retrograde flow have been identified as essential for viral attachment and endocytosis, yet the spatial and temporal coordination of these molecules on the cell surface is still unclear. Among the proteins involved in the secondary receptor complex CD151 stands out for its crucial role in facilitating viral access and organizing the multiple cellular components necessary for successful infection. However, it is still unclear whether CD151 plays an early role in HPV entry and how the HPVs are transferred from the primary receptor (HSPGs) to the secondary receptor complex.

Aim of the present study was the characterization of CD151 assemblies at PsV binding sites. The effect of CD151 expression levels on entry complex formation was analyzed. Additionally, it was characterized if PsVs bind to preformed CD151 assemblies. Moreover, the impact of ErbB2 signaling on PsV platform formation was explored.

Another aim of the study was analyzing the relationship between actin-dependent transport and CD151 association in HPV infection employing the actin inhibitor cytochalasin D. Thereby, the onset of PsV translocation from the ECM onto the cell body was explored. Hereby, the human keratinocyte cell line HaCaT was validated as ideal model system to study early events in HPV infection.

The last aim of the study was to study the effect of the HSPG-binding peptide peptide 19-2.5 on CD151 assemblies to analyze their potential capacity in inhibiting or preventing HPV infection.

3. Material and Methods

3.1 Material

3.1.1 Equipment

Table 1. Equipment

Equipment	Supplier	Application
3D 4-channel STED microscope coupled to an Olympus IX83 confocal microscope	Abberior Instruments, Göttingen, Germany; Olympus, Tokyo, Japan	Confocal and STED microscopy
Centrifuge 5810	Eppendorf SE, Hamburg, Germany	For cell culture purposes
Compact Shaker KS 15	Edmund Bühler GmbH, Bodelshausen, Germany	For cell culture purposes
GFL Incubation/Inactivation Water Bath 1008	Gesellschaft für Labortechnik mbH, Burgwedel, Germany	Heating of cell culture media
Incubator	BINDER GmbH, Tuttlingen, Germany	Cultivation of cells
Inverted microscope ECLIPSE TS100, CFI60 Infinity Optical System	Nikon, Tokyo, Japan	Brightfield microscope for cell culture purposes
NEON™ Transfection System	ThermoFisher Scientific, Waltham, USA	Transfection of cells by electroporation
Sonopuls HD 2070	Bandelin, Berlin, Germany	Generation of membrane sheets
Sterile bench	BDK Luft- und Reinraumtechnik GmbH, Sonnenbühl, Germany	Sterile workspace for cell culture purposes
Stuart™ SB2 rotator	Cole-Parmer GmbH, Vernon Hills, USA	For cell culture purposes

3.1.2 Chemicals

Table 2. Chemicals

Chemicals	Supplier
(4-(2-hydroxyethyl)-1-piperazineethanesulfonic acid) (HEPES, PUFFERAN® ≥99.5%, p.a.)	Carl Roth, cat# 9105.3
Ammonium chloride (NH_4Cl, ≥99.5%, p.a., ACS, ISO)	Carl Roth, cat# K298.2
(-)-Blebbistatin	Sigma-Aldrich, cat# B0560-1MG, stock solution 13.68 mM in DMSO

Bovine Serum Albumin (BSA) US Origin, Protease free, lyophilized powder	PAN Biotech, cat# P06-139210
Cytochalasin D	Invitrogen™, cat# PHZ, 1063, 10 mg/ml Stock in DMSO
Disodium hydrogen phosphate (Na_2HPO_4, ≥99%, p.a.	Carl Roth, cat# 4984.1
Ethylene glycol-bis(β-aminoethyl ether)-N,N,N′,N′-tetraacetic acid (EGTA, ≥99%, p.a.)	Carl Roth, cat# 3054.3
Furin inhibitor I	Sigma-Aldrich, cat# 344930-1MG, stock solution 5 mM in DMSO
Leupeptin	Carl Roth, cat# CN33.1, stock solution 100 mM in $_{dd}H_2O$
L-Glutamic acid monopotassium salt monohydrate (KGlu, 97+%)	Thermo scientific, cat# A17232.0B
Paraformaldehyde (PFA)	Carl Roth, cat# 0335.1
Phalloidin iFluor488	abcam, cat# ab176753, used 1:1000
Phalloidin iFluor647	abcam, cat# ab176759, used 1:1000
Poly-L-Lysine Hydrobromide (PLL)	Merck Chemicals GmbH, cat# P2636-100 mg
Potassium acetate (KAc, CELLPURE® ≥99%)	Carl Roth, cat# HN10.3
Potassium chloride (KCl, ≥99.5%, p.a., ACS, ISO)	Carl Roth, cat# 6781.1
Potassium dihydrogen phosphate (KH_2PO_4, ≥99%, p.a., ACS)	Carl Roth, cat# 3904.1
Sodium chloride (NaCl, 99.85%)	Acros Organics, cat# 327300025
Triton X-100	Carl Roth, cat# 3051.3
Tucatinib	Biomol GmbH, cat# Cay31411-10, 10 mM Stock in DMSO

3.1.3. Buffer and solutions

All buffers and solutions were prepared using double distilled water ($_{dd}H_2O$) and autoclaved or sterile filtered if necessary.

Table 3. Buffers and solutions

Buffer	Composition
Blocking buffer	3% (w/v) BSA in PBS
Paraformaldehyde (PFA) stock solution	16% (w/v) PFA in $_{dd}H_2O$
PFA fixation buffer	PFA stock solution was adjusted with 1x PBS to get fixation solution of 4% PFA
Permeabilization buffer	0.2% (v/v) Triton X-100 in PBS
Phosphate buffered saline (PBS)	137 mM NaCl, 2.7 mM KCl, 1.76 mM KH_2PO_4, 10 mM Na_2HPO_4 in $_{dd}H_2O$ adjusted to pH 7.4
Poly-L-lysine (PLL) stock solution (20x)	2 mg/mL PLL in $_{dd}H_2O$
Quenching buffer	50 mM NH_4Cl in PBS

Sonication buffer	120 mM KGlu, 20 mM KAc, 10 mM EGTA, 20 mM HEPES in $_{dd}H_2O$ adjusted to pH 7.2

3.1.4 Cell culture media

Table 4. Cell culture media

Name	Composition	Supplier
Dulbecco's PBS (DPBS)		Gibco®, cat# 14190169
Fetal bovine serum Supreme (FBS)		PAN Biotech, cat# P30-3031
HaCaT growth medium	High glucose DMEM medium supplemented with 10% FBS and 1% Penicillin/Streptomycin (10,000 U/ml Penicillin, 10 mg/ml Streptomycin)	High glucose DMEM (Gibco®, cat# 61965-026) FBS (PAN Biotech, cat# P30-3031) Penicillin/Streptomycin (PAN Biotech, cat# P06-07100)
HaCaT medium for experiments	High glucose DMEM medium supplemented with 10% FBS	High glucose DMEM (Gibco®, cat# 61965-026) FBS (PAN Biotech, cat# P30-3031)
HeLa growth medium	High glucose DMEM medium supplemented with 10% FBS and 1% Penicillin/Streptomycin (10,000 U/ml Penicillin, 10 mg/ml Streptomycin)	High glucose DMEM (Gibco®, cat# 61965-026) FBS (PAN Biotech, cat# P30-3031) Penicillin/Streptomycin (PAN Biotech, cat# P06-07100)
HeLa medium for experiments	High glucose DMEM medium supplemented with 10% FBS	High glucose DMEM (Gibco®, cat# 61965-026) FBS (PAN Biotech, cat# P30-3031)
High glucose DMEM		Gibco®, cat# 61965-026
Penicillin/Streptomycin	10,000 U/ml Penicillin and 10 mg/ml Streptomycin	PAN Biotech, cat# P06-07100
Trypsin solution		PAN Biotech, cat# P10-0231SP

3.1.5 Kits

Table 5. Kits

Kit	Supplier	Application
ClickTech EdU Cell Proliferation Kit 488	Carl Roth, cat# 1Y67.1	Staining of EdU-PsVs via click-chemistry

ClickTech EdU Cell Proliferation Kit 647	Carl Roth, cat# 1Y64.1	Staining of EdU-PsVs via click-chemistry
Lipofectamine™ RNAiMAX Transfection Reagent	Invitrogen™, cat# 13778150	Transfection of cells with siRNA
Neon™ Transfektionssystem 100 µl-Kit	Invitrogen™, cat# MPK10096	Transfection of cells with plasmids

3.1.6 Antibodies

Primary antibodies

Table 6. Primary antibodies

Target/Name	Host/Clone	Supplier	Dilution
CD151	Mouse IgG, monoclonal	Biorad, cat# MCA1856GA	1:200
CD151	Rabbit IgG, polyclonal	abcam, cat# ab185684	1:200
Heparan sulfate (HS)	mouse IgM, monoclonal	amsbio, cat# 370255-S	1:200
HS neo-epitope (Δ-HS)	mouse IgG, monoclonal	amsbio, cat# 370260-S	1:200
HPV16 L1 (312F)	mouse IgG, monoclonal	as described previously (Knappe et al., 2007), PMID: 17640876	1:200
HPV16 L1 (K75)	rabbit IgG, polyclonal	as described previously (Rommel et al., 2005), PMID: 15543569	1:1000
Integrin alpha 6 (Itgα6)	rabbit IgG, polyclonal	Invitrogen™, cat# PA5-12334	1:200

Secondary antibodies

Table 7. Secondary antibodies

Target	Host	Fluorophore	Supplier	Dilution
GFP	alpaca	Booster Atto488	Chromotek®, cat# gba488	1:200
mouse IgG	donkey	AlexaFluor™ 594	Invitrogen™, cat# A21203	1:200
mouse IgM	goat	AlexaFluor™ 594	Invitrogen™, cat# A21044	1:200

mouse IgG	goat	STAR RED	Abberior, cat# STRED-1001-500UG	1:200
rabbit IgG	donkey	AlexaFluor™ 594	Invitrogen™, cat# A21207	1:200
rabbit IgG	goat	STAR GREEN	Abberior, cat# STGREEN-1002-500UG	1:200
rabbit IgG	goat	STAR RED	Abberior, cat# STRED-1002-500UG	1:200

3.1.7 Plasmids

Table 8. Plasmids

Construct	Origin	Backbone	Description
CD151-GFP	(Scheffer et al., 2013)	pEGFP-C1, Clontech Laboratories, Mountain View, USA	CD151 N-terminally tagged with EGFP

3.1.8 siRNA

For ErbB2 siRNA a pool of two siRNAs with dT-dT overhangs was used: ErbB2#1 (CAAAGAAAUCUUAGACGAA[dT][dT]) and ErbB2#2 (GUGUGCACCGGCACAGACA[dT][dT]) provided by Sigma-Aldrich (Hamburg, Germany). AllStars Negative Control siRNA was used as nonsilencing control and was obtained from Qiagen (Hilden, Germany).

3.1.9 Cell lines

HaCaT

Human immortalized keratinocytes (HaCaT) were obtained from Cell Lines Services (Eppelheim, Germany). HaCaTs are derived from an adult human skin melanoma and spontaneously immortalized (Boukamp et al., 1988).

HeLa

The immortalized human cell line HeLa is the oldest human cell line and derived from cervical cancer. HeLa cells were obtained as a kind gift from Waldemar Kolanus, Bonn, Germany (SCHERER et al., 1953).

3.1.10 PsVs

HPV16 PsVs were kindly provided by Luise Florin and produced following established procedures (Buck et al., 2004, Spoden et al., 2012). In brief, a pGL4.20 luciferase reporter plasmid containing the HPV

long control region (LCR) HPV16 promotor was co-transfected with codon-optimized L1 and L2 expression vector pShell 16L1/L2wt into HEK 293TT cells using polyethylimine. Afterwards, the cell culture medium was supplemented with 20 µM 5-ethynyl-2'-deoxyuridine (EdU, Click-iT AlexaFluor® 488 Imaging Kit, Thermo Fisher Scientific) to enable DNA-staining by click-chemistry. After 48 hours, cells were lysed and PsVs were purified by gradient centrifugation using OptiPrep (Sigma-Aldrich, Hamburg, Germany). To quantify viral genome equivalents (vge) of PsVs, quantitative PCR using a 7500 Real-Time PCR System and Sequence Detection Software v2.3 (Applied Biosystems, Foster City, USA) was used. For all experiments a stock solution of 7.7 x 10^6 vge/µL was used.

3.1.11 Software

Table 9. Software

Software	Supplier/Developer	Application
CorelDraw Graphics	Corel Corporation, Ottawa, Canada	Illustration, layout and visualization of data
GraphPad Prism 9.5.1	GraphPad Software Inc., San Diego, USA	Data organization, statistical analysis, and visualization/ data plotting
ImageJ (FIJI bundle)	Wayne Rasband, National Institute of Health, USA	Image analysis
Microsoft Office Excel	Microsoft Corporation, Redmond, USA	Data analysis, statistical analysis, and organization
Microsoft Office Word	Microsoft Corporation, Redmond, USA	Writing

3.2 Methods

3.2.1 Cell culture

HaCaTs were cultured in high glucose DMEM (Gibco® 61965-026) medium supplemented with 10% FBS (PAN Biotech, cat# P30-3031) and 1% Penicillin/Streptomycin (10,000 U/ml Penicillin, 10 mg/ml Streptomycin; PAN Biotech, cat# P06-07100) at 37 °C with 5% CO_2. HeLas were cultured in high glucose DMEM (Gibco® 61965-026) medium supplemented with 10% FBS (PAN Biotech, cat# P30-3031) and 1% Penicillin/Streptomycin (10,000 U/ml Penicillin, 10 mg/ml Streptomycin; PAN Biotech, cat# P06-07100) at 37 °C with 5% CO_2. Cells were grown to confluence and passaged every 3-4 days. HaCaTs and HeLas were split at approximately 1:10 - 1:20. HaCaT and HeLa cells were used up to a maximum passage of 40 and 30, respectively.

3.2.2 Transfection with plasmids

HaCaT cells were transfected with plasmid DNA using the Neon™ Transfection electroporation system, according to the manufacturer's instructions. For transfection, 2 x 10^6 HaCaT cells were centrifuged at 1000 g for 3 min. The supernatant was removed, and cells were washed with PBS, following an additional centrifugation step at 1000 g and 3 min. The cell pellet was resuspended in 125 µl R-buffer and mixed with 12 µg of plasmid DNA. Three pules for 10 ms at 1400 V were applied. Transfected HaCaT cells were transferred into antibiotic-free growth medium and cultivated at 37 °C and 5% Co_2 for 24 h. Approximately 1 x 10^5 HaCaT cells not undergoing the electroporation were used as control.

3.2.3 Transfection with siRNA

HaCaT cells were transfected with siRNA using the Lipofectamine RNAiMAX Transfection Reagent according to the manufacturer's instructions. Approximately 150,000 HaCaT cells were plated onto 25 mm diameter poly-L-lysine (PLL) coated glass coverslips in 6-well plates and incubated over night at 37 °C and 5% CO2. The next day, cells were incubated with 45 pmol of pooled ErbB2 siRNA per well. The corresponding amount of AllStars Negative Control siRNA was used as control. Cells were incubated for 48 h at 37 °C and 5% CO_2.

3.2.4 Incubation with CytD

150,000 HaCaT cells were plated onto PLL-coated glass coverslips in 6-well plates and incubated for 24 h. The next day, cells were incubated with 50 vge PsVs per plated cell in DMEM supplemented with 10% FBS for a total of 5 h at 37 °C and 5% CO_2. After 0 h, 1 h and 3 h, 10 µg/ml cytochalasin D (CytD; stock solution 10 mg/ml in dimethyl sulfoxide (DMSO)) was added. As a control, the same amount of DMSO was added. Cells were fixed and further processed for imaging.

3.2.5 Transient incubation with CytD

150,000 HaCaT cells were plated onto PLL-coated glass coverslips in 6-well plates and incubated for 24 h. The next day, cells were incubated with 50 vge PsVs per plated cell and 10 µg/ml CytD (stock solution 10 mg/ml in dimethyl sulfoxide (DMSO)) in DMEM supplemented with 10% FBS for 5 h at 37 °C and 5% CO_2. As a control, the same amount of DMSO without CytD was added. Cells were washed with PBS and fresh DMEM supplemented with 10% FBS was added. HaCaTs cells were incubated for another 0 min (here the medium was added followed by immediate removal), 15 min, 30 min, 60 min and 180 min at 37 °C and 5% CO_2. Cells were fixed and further processed for imaging.

3.2.6 Incubation with peptide 19-2.5

150,000 HeLa cells were plated onto PLL-coated glass coverslips in 6-well plates and incubated for 24 h. The next day, cells were incubated with PsVs of approximately 50 vge per cell for 1 h at 37 °C

and 5% CO_2. An hour after PsVs addition, 1 µg/mL control peptide, peptide 19-2.5, or no peptide was added, and cells were incubated for additional 3 h. Cells were fixed and further processed for imaging. Additionally, one sample was directly fixed after the one-hour incubation with PsVs.

3.2.7 Sample preparation

3.2.7.1 PLL-coated coverslips

For cleaning of glass coverslips (25 mm diameter, high precision, 1.5H) used for microscopic experiments, coverslips were incubated with 1 M HCl for 2 h under constant agitation. Afterwards, HCl was removed, and coverslips were thoroughly washed with distilled H_2O, following an incubation with 1 M NaOH for 1 h under constant agitation. Coverslips were thoroughly washed with distilled H_2O again. Then, coverslips were kept in 100% EtOH until further usage. For microscopic experiments, glass coverslips were coated with poly-L-lysine (PLL). Therefore, coverslips were transferred into 6-well plates. After excess EtOH has evaporated, coverslips were coated with 100 µg/ml PLL in H_2O for 30 min. Afterwards, the PLL solution was removed and coverslips were dried overnight, followed by a sterilization with UV light for 20 min. 6-well plates with coverslips were kept at 4 °C until further usage.

3.2.7.2 Generation of membrane sheets

For membrane sheet generation, HaCaT cells seeded on PLL-coated glass coverslips were washed 2-times in ice-cold PBS. Afterwards, coverslips were transferred into a petri-dish containing ice-cold sonification buffer and a 100 ms ultrasound pulse at 100% power was applied (the distance of the sonication tip was adjusted to approximately 0.1 mm above the coverslip). This was repeated until in total about 10 pulses were applied at various locations of the coverslip.

3.2.7.3 Fixation and fluorescence labeling

Cells or membrane sheets on PLL-coated coverslips were fixed with 4% PFA at room temperature (RT) for 30 min. PFA is removed, and residual PFA is quenched with 50 mM NH_4Cl in PBS for 30 min at RT. If cells or membrane sheets were permeabilized, 0.2% Triton-X-100 in PBS was applied for 1 min. Samples were blocked with 3% BSA in PBS for 30 min at RT. If PsVs were stained via click-chemistry, staining of PsVs was performed for 30 min at RT according to the manufacturer's instructions. Then, samples were washed three times with PBS. In case of no PsV labeling by click-chemistry, directly after blocking, primary antibody staining was performed in 3% BSA in PBS for 2 h at RT. Samples were washed three times with PBS before adding the respective secondary antibodies and fluorescent labelled phalloidins in 3% BSA in PBS for 1 h at RT. Afterwards, samples were washed three times with PBS, followed by mounting of the coverslips onto microscopy slides using ProLong® Gold antifade mounting medium.

3.2.8 STED and confocal microscopy

For confocal and STED microscopy, samples were imaged employing a 4-channel STED microscope from Abberior Instruments. The microscope is based on an Olympus IX83 confocal microscope equipped with an UPlanSApo 100x (1.4 NA) objective (Olympus, Tokyo, Japan). For confocal imaging a 488 nm laser for excitation detected at 500–550 nm was employed (excitation of STAR GREEN, GFP Booster Atto488, phalloidin iFluor488, and PsVs labelled by click-chemistry with 6-FAM-Azide) and for STED imaging a 561 nm laser for excitation detected at 580–630 nm (excitation of Alexa594) in combination with a 775 nm laser for depletion and a 640 nm laser for excitation detected at 650-720 nm (excitation of STAR RED and PsVs labelled by click-chemistry with Eterneon RED 645-Azide) in combination with a 775 nm laser for depletion was employed. First, confocal micrographs were taken followed by STED micrographs. For experiments where CytD was washed off, confocal and STED micrographs were taken in parallel. Laser intensity for STED micrographs was 45% for excitation with a 561 nm laser, 45% for excitation with a 640 nm laser and 45% for depletion with a 775 nm laser. The pixel size was set to 25 nm.

3.2.9 Image analysis

Images were analyzed using Fiji ImageJ in combination with custom written macros. When analyzing double stainings using Alexa594 (excited with 561 nm; red channel) together with STAR RED (excited with 640 nm; long red channel), crosstalk from the red into the long red channel was corrected. Prior to image analysis 40% of the red-channel-image was subtracted from the long-red-channel image. Images were smoothed with a Gaussian blur of $\sigma = 0.5$, except for images of PsVs labelled with click-chemistry that were smoothed with a Gaussian blur of $\sigma = 1$, to improve maxima detection. If not stated otherwise a rectangular region of interest (ROI) was placed in one channel and propagated to the other channels. This ROI was used for maxima analysis, mean intensity and Pearson Correlation Coefficient (PCC).

3.2.9.1 Maxima analysis

Maxima analysis was performed with a custom written macro (developed by Dr. Jan-Gero Schloetel). The macro is based on the 'Find Maxima' function in ImageJ and used to determine maxima density, maxima fluorescence intensity, maxima size and maxima distances (Schmidt et al., 2024). Local maxima were detected using the 'Find Maxima' function in ImageJ with a specific threshold (noise tolerance) that varied between experiments. The following noise tolerances were used: 10 for PsVs (PsV-DNA) in Figure 9; 80 for PsVs (PsV-L1) and 10 for CD151 in Figure 10-11; 6 for PsVs (PsV-DNA) and 4 for CD151 in Figure 13-14; 60 for PsVs (PsV-L1) in Figure 16; 80 for PsVs (PsV-L1) in Figure 18; 80 for PsVs (PsV-L1) in Figure 22; 80 for PsVs (PsV-L1) and 8 for CD151 in Figure 23-24; 3 for PsVs (PsV-DNA),

6 for HS and 15 for Itgα6 in Figure 27-30; 80 for PsVs (PsV-L1) and 6 for HS in Figure 31-33; 150 for PsVs (PsV-L1) and 4 for CD151 in Figure 35-37.

Maxima density was calculated by relating the number of detected maxima to the analyzed area (ROI size).

To measure the maxima fluorescence intensity, a circular ROI with a diameter of 125 nm (5 pixels) was placed onto the determined maxima positions. Within these ROIs, the average fluorescence intensity of each maximum is measured. The average background fluorescence intensity is measured in a ROI placed next to the cell or membrane sheet and subtracted from the average fluorescence intensity of the maxima.

To determine the maxima size, a horizontal and a vertical line scan (31 pixels long × 3 pixels width) was fitted on every maximum location, and a Gaussian function was fitted to the intensity profile of each line scan. Only the Gaussian fit with the best quality was considered for further analysis. Based on the best fit, the maxima size was determined by the full-width of half maximum (FWHM). Based on the circular 125 nm diameter ROI used to determine maxima fluorescence intensity, the center of mass of fluorescence is determined for every maximum, yielding the maxima positions in sub-pixels. These positions were used to calculate maxima distances between channels.

For all the parameters analyzed only maxima undergoing a quality control step were included in the analysis. Only if the fitted Gaussian distribution of the best fitted line scan (31 pixels long × 3 pixels width) exhibits a fit quality of $R^2 > 0.8$ and if the Gaussian maximum locates central to the intensity distribution the maximum is included in the further analysis. However, when analyzing the shortest distance between maxima only the maximum from which the shortest distance to the next nearest maximum in the respective other channel was determined undergoes the quality control step.

3.2.9.2 Mean intensity

To measure the mean intensity in a ROI, the mean gray value was determined in ImageJ. For background correction, the mean gray value measured in a ROI next to the cell or membrane sheet was subtracted.

3.2.9.3 Neighbored maxima analysis

For measuring the neighbored maxima with a custom written ImageJ macro (developed by Dominik Sons), the circular 125 nm diameter ROI used for determining the maxima fluorescence intensity was enlarged to a circular 425 nm or 925 nm diameter ROI and placed onto the maxima positions from the 'Find maxima' function. Employing the same threshold (noise tolerance) as for the maxima detection, the number of maxima within the circular ROI was counted.

3.2.9.4 Normalized PsV neighbored CD151 maxima

For measuring the normalized PsV neighbored CD151 maxima with a custom written ImageJ macro, the circular 125 nm diameter ROI used for determining the maxima fluorescence intensity was enlarged to a circular 925 nm diameter ROI. To this end, at every PsV maxima position, the 925 nm circular ROI was placed, and the number of CD151 maxima in this ROI were counted employing the same noise tolerance as for the maxima detection. For each cell, the counted CD151 maxima at every PsV position were normalized to the average CD151 maxima density of the large rectangular ROI used for maxima detection, yielding the normalized PsV neighbored CD151 maxima. To obtain a control for the randomized association between L1 and CD151 the same procedure was employed on horizontally and vertically flipped ROI areas of the CD151 channel, using the original PsV maxima positions.

3.2.9.5 Background correction close PsV association fraction

Based on the shortest distances of a PsV and its next nearest entry component, the fraction of PsVs closely associated with different entry components was analyzed. For a close association, a distance close to the resolution limit of the used microscope of ≤ 80 nm was defined and the fraction of PsVs fulfilling this distance to its next nearest maximum of entry components was calculated. The fraction of closely associated PsVs is further corrected for random background association. Therefore, the fraction of closely associated PsVs was calculated on horizontally and vertically flipped (randomized) ROI-defined images of entry components. The values of the closely associated PsVs calculated from flipped images were plotted against the maxima density of the corresponding entry components and a linear regression line was fitted through the data points. Based on this calibration curve, the random background association for every maxima density can be calculated and the fraction of closely associated PsVs can be background corrected.

3.2.9.6 Pearson correlation coefficient

The PCC was calculated with a custom written ImageJ macro (developed by Dr. Jan-Gero Schloetel) to determine the overlap between two images. In theory, the PCC would equal 1 in the case of a perfect overlap and -1 for a perfect negative correlation (an image and its negative). The PCC was calculated between ROI-defined images. As a control for random overlap, the PCC was calculated after one image was horizontally and vertically flipped (randomized).

3.2.9.7 PsV distribution in HaCaT cells

To analyze the PsV distribution in HaCaT cells after CytD treatment, the PsV images were converted into 8-bit format in Image J. Binary images were generated employing an individual threshold for every image to reduce background noise. Afterwards, the integrated density was calculated for every image and the fraction of PsV signal in every cell section was calculated.

3.2.9.8 PsV diminishment in cell border region

The ImageJ ‘Make Binary’ function was used on CD151 micrographs for generating a binary mask in order to define the cell border region. The ‘Wand’ tool was used to further outline the area covered by the cell, when possible, otherwise the same was done manually using the original micrograph as a reference. A ROI was created from the outline in the binary mask and filled in white with the ’Flood Fill’ Tool. Afterwards, the ROI was shrunk to a 20-pixel broad strip, and cleared outside of the strip, leaving a 20-pixel broad, closed ribbon marking the intracellular side of the cell border. However, this process produced arbitrary edges that were removed by manual adjustments with the ’Pencil’ tool and the clear function. The obtained ROI defines the intracellular side of the cell border. Subsequently, the ROI was symmetrically broadened by 40 pixels using the ‘Enlarge’ function in ImageJ resulting in a at least 60 pixels broad ROI. This ROI covered approximately two thirds of the intracellular and one third of the extracellular side of the cell. Using the ImageJ ‘Find Maxima’ function, PsV maxima were detected with a custom written macro in ImageJ both in the cell border region ROI and in a ROI covering the entire micrograph (excluding a 2-pixel edge). From these values, the percentage of PsVs within the cell border region was calculated.

3.2.9.9 Distal PsVs analysis

In X,Z-scans and Y,Z-scans, to analyze the fraction of distal PsVs, the images of both channels were interpolated in the z dimension by a factor of 8. Then, the cell was outlined with reference to the CD151 signal. Using these ROIs, the integrated density of PsVs was measured in the cell outline. In addition, the integrated density of the entire image was measured. For background correction, a small ROI was placed onto a background region. The integrated density was measured and with reference to the area of the cell outline and the entire image the background signal was calculated and subtracted. Based on the background corrected values, the percentage of distal PsVs was calculated as 100% (entire image) − percentage in the “cell outline”.

3.2.10 Statistics

Data sets were based on three biological replicates, including at least 14 images per replicate. Data was analyzed with GraphPad Prism 9.5.1 and tested for significance with a two-tailed, unpaired student’s t test with significance * = $p < 0.05$, ** = $p < 0.01$ and *** = $p < 0.001$.

4. Results

HPV16 is one of the most prevalent and oncogenic HPV genotypes, serving as the primary etiologic agent for cervical and other anogenital cancers (Baba et al., 2025, Kreimer et al., 2005, Lu et al., 2022, Martel et al., 2017, Szymonowicz, Chen, 2020, Tommasino, 2014). Entry of HPV16 into host cells marks the beginning of infection and, ultimately, cancer development. Recent research has increasingly illuminated the pivotal role of the tetraspanin CD151 in mediating and organizing the early steps of HPV16 cell entry (Scheffer et al., 2013, Scheffer et al., 2014, Spoden et al., 2008). HPV16 initially binds to cell surface heparan sulfate proteoglycans (Culp et al., 2006, Giroglou et al., 2001, Joyce et al., 1999, Richards et al., 2013) before undergoing structural changes (Bienkowska-Haba et al., 2009, Cerqueira et al., 2015, Richards et al., 2006) that facilitate interaction with secondary receptors, including integrins and tetraspanins. CD151 forms part of TEMs on the host cell membrane, assembling with laminin-binding integrins to create specialized viral entry complexes (Evander et al., 1997, Finke et al., 2020b, Yoon et al., 2001). Within these microdomains, CD151 acts as a molecular organizer, recruiting and clustering integrins and accessory factors, enhancing their lateral mobility, and positioning them for efficient viral uptake (Finke et al., 2020b). These complexes are critical for the transfer of bound viral particles from the cell surface into the cell. However, it remains unclear whether CD151 already plays a role in early stages of HPV entry prior to internalization, as well as how HPV virions are transferred from the primary receptor to the secondary receptor complex. Additionally, the slow and asynchronous nature of HPV uptake makes membrane-level microscopy challenging for analyzing early virus entry events. In this study, the initial phases of HPV infection were examined in detail.

4.1 Characterization of the PsV/CD151 association

Among the proteins involved in the formation of the secondary receptor complex during HPV16 cell entry, CD151 stands out for its crucial role in facilitating viral access and organizing the cellular components required for successful infection (Finke et al., 2020b, Mikuličić, Florin, 2019, Scheffer et al., 2013, Scheffer et al., 2014). HPV16 and CD151 have been shown to form large clusters during viral cell entry, especially upon CD151 overexpression (Finke et al., 2020b). However, it is possible that the formation of these extensive CD151 aggregates on the cell surface is a PsV-independent process that only depends on CD151 expression levels.

4.1.1 PsV concentration

To assess the role of CD151 in HPV16 PsV cell entry, the concentration required for half-maximal PsV binding was determined. This approach ensures that a sufficient number of PsV binding events can be analyzed per cell. First, HaCaTs were treated with and without PsVs for 3 h. Afterwards, cells were fixed, permeabilized and antibody stained for Itgα6 (green) as a cell body marker. PsVs were stained

via click-chemistry with a fluorescein dye (magenta). Samples were imaged with confocal microscopy. Both stainings appeared in a spotty pattern (Figure 9A). Whereas Itgα6 concentrated in spots scattered across the cell surface, the PsV staining concentrated at cell protrusions and the cell periphery (Figure 9A). Importantly, in the sample without PsVs no discrete PsV signals in the respective channel were recorded, although the EdU staining produced a fuzzy dim background noise that was absent in the PsV sample.

Next, different PsV concentrations were tested to determine the concentration required for half-maximal PsV binding. Therefore, HaCaT cells were treated with different PsV concentrations (0 – 92.5 vge/plated cell) for 3 h, fixed, permeabilized and stained for Itgα6 (green) and PsVs (magenta) as mentioned above. Samples were imaged with confocal microscopy (Figure 9B). Region of interests (ROIs) were placed by outlining the cell shape based on the Itgα6 staining. The total PsV maxima were counted within these ROIs (Figure 9C) and the concentration required for half-maximal PsV binding (IC50) was determined (Figure 9D). At lower vge, the PsV maxima per cell correlate with the PsV concentration used (Figure 9C). However, with a concentration higher than 55.5 vge/plated cell the PsV maxima reached a plateau. This may be caused by saturation of binding sites and/or the limited resolution of single PsVs when reaching a specific concentration. The calculated concentration required for half-maximal PsV binding is 34.01 ± 5.05 vge/plated cell (Figure 9D). However, to guarantee enough PsV events per cell to analyze the secondary receptor complex, a PsV concentration of 46 vge/plated cell was used throughout all subsequent experiments.

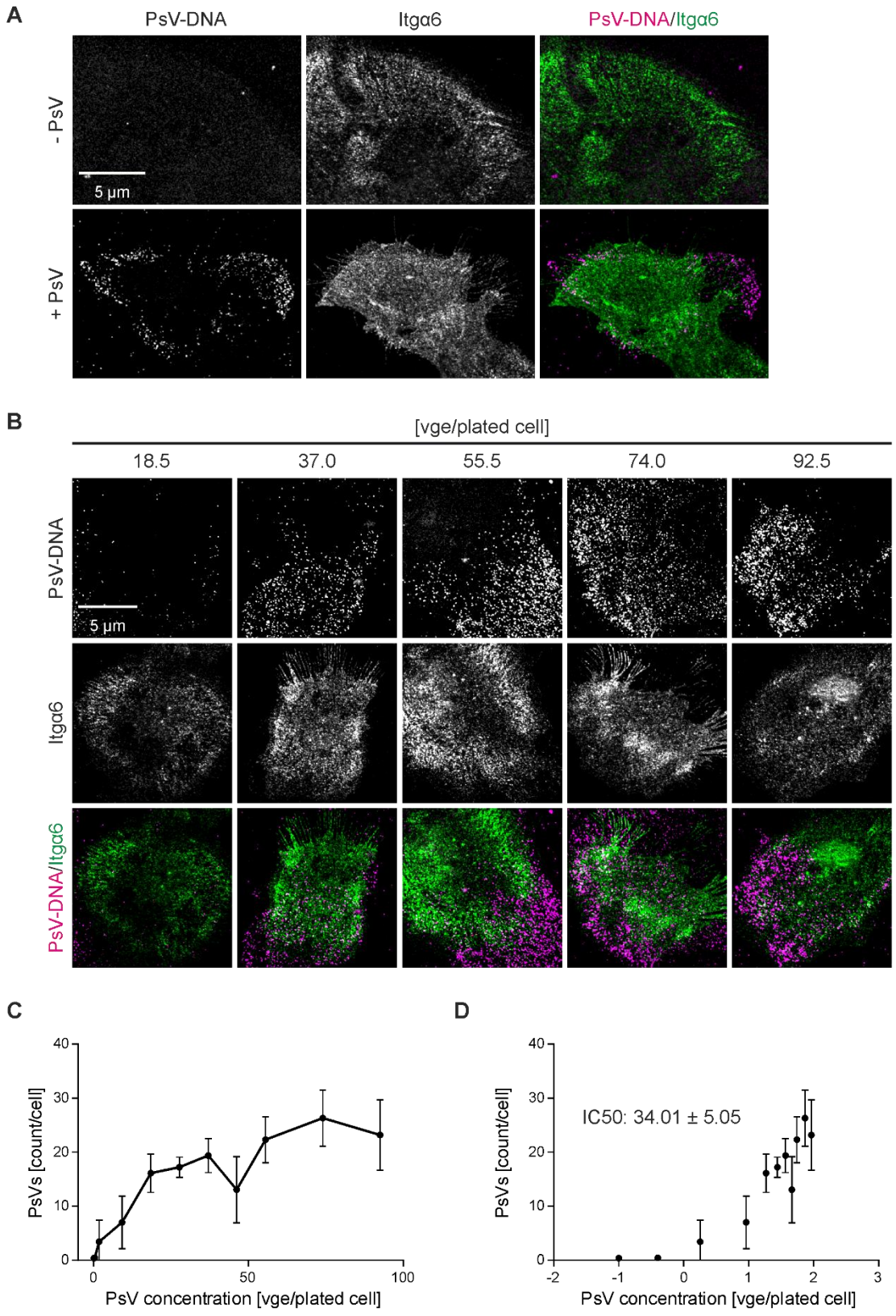

Figure 9. Determination of the concentration for half-maximal PsV binding.
(A) HaCaT cells were incubated with PsVs for 1 h. Then, cells were fixed, permeabilized and PsVs (magenta) were visualized by click-labeling of the plasmid DNA in the confocal channel, whereas Itgα6 (green, AlexaFluor™ 594) was visualized by antibody staining in the STED channel. (B) In the same experiment described in (A) were different PsV concentrations tested. (C) An image algorithm detects

local maxima in the PsV images. The PsV maxima counted per cell were plotted against the PsV concentration. (D) The IC50 was calculated to determine the concentration of half-maximal PsV binding. Values are given as mean ± SD (n = 3).

4.1.2 Impact of CD151 overexpression on CD151 maxima

It has been shown that HPV16 and CD151 form large agglomerations during the viral cell entry. Especially upon CD151 overexpression, large CD151 agglomerations can be observed (Finke et al., 2020b). It is still unknown whether those large agglomerations are a side effect off the CD151 overexpression or virus induced. To analyze the impact of the CD151 overexpression on the CD151 agglomeration formation, HaCaT cells were transfected with CD151-GFP and incubated with and without PsVs for 5 h. As a control, untransfected cells were used. Cells were fixed, sheeted and immunostained with antibodies against CD151 (green) and L1 (PsVs, magenta). Both stainings appeared in a spotty pattern (Figure 10A). Whereas CD151 concentrated in spots scattered across the membrane sheet, the L1 staining is highly variable and appeared in spots either at the membrane sheet periphery or across the membrane sheet. Membrane sheets of HaCaTs transfected with CD151-GFP appear brighter than sheets of control cells (Figure 10A). Images were analyzed using a custom written macro (by Jan-Gero Schloetel) in Fiji ImageJ. ROIs were placed on the membrane sheets based on the GFP/phalloidin signal. In CD151-GFP transfected HaCaT cells, CD151 maxima are 100% brighter than CD151 maxima in control cells, independent of a PsV incubation. Nevertheless, CD151 maxima are about 10% brighter upon PsV treatment (Figure 10B). Additionally, CD151 maxima are 25% wider in CD151-GFP overexpressed cells, independent of an additional PsV treatment. Upon PsV incubation, CD151 maxima are slightly wider than in cells not treated with PsVs (Figure 10C). The maxima density of CD151 maxima is in CD151-GFP overexpressed HaCaT cells, about 15% lower compared to control cells. The PsV incubation has no effect on the CD151 maxima density (Figure 10D). Additionally on membrane sheets of PsV treated HaCaT cells, the Pearson Correlation Coefficient (PCC) between L1 and CD151 was determined. In control cells the PCC is 0.24 and in CD151-GFP overexpressed cell 0.2. As a control, the PCC was determined on horizontally and vertically flipped (randomized) images as well and is close to zero (Figure 10E). This indicates a specific association between L1 (PsVs) and CD151.

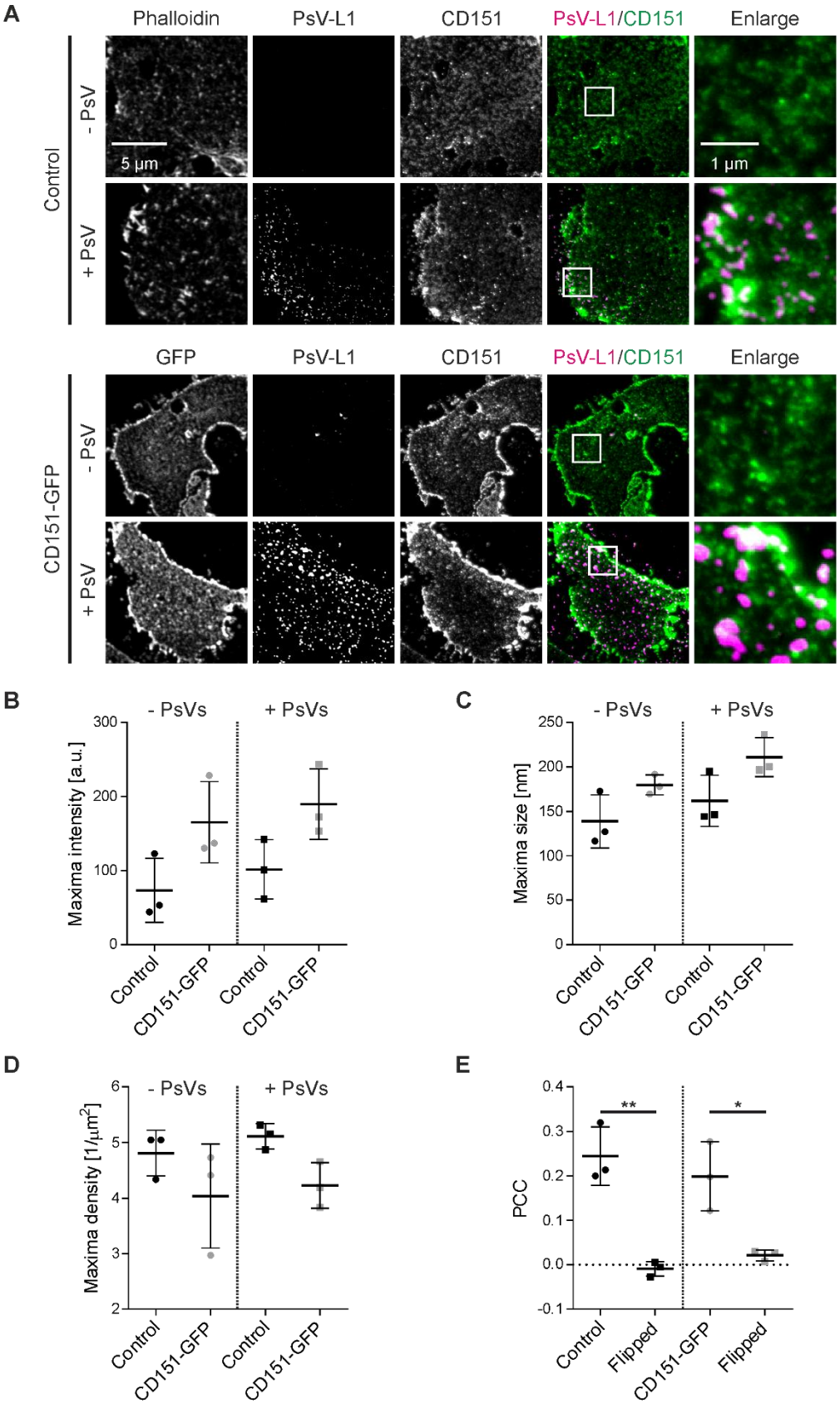

Figure 10. Effect of a CD151 overexpression on the association between PsVs and CD151.
(A) HaCaT cells were transfected with CD151-GFP and incubated with PsVs for 5 h. Then, cells were fixed, membrane sheets were generated, and F-actin was stained with phalloidin iFluor488. PsVs were

stained by immunofluorescence using an antibody against L1 in combination with an AlexaFluor™ 594-labelled secondary antibody and CD151 was stained by immunofluorescence with STAR RED. Images of phalloidin were acquired in the confocal mode and images of PsVs and CD151 were acquired in the STED mode of a STED microscope, respectively. ROIs were placed on the membrane sheets based on the GFP/phalloidin signal. Analysis of the CD151 maxima intensity (B), CD151 maxima size (C) and CD151 maxima density (D). (E) PCC analyzed in the ROI between the PsVs and CD151 in original and flipped (randomized) images. Values are given as means ± SD (n = 3). Statistical differences between the groups were analyzed using unpaired student's t-test.

As PsVs in CD151 transfected HaCaT cells appear brighter (Figure 11A), a histogram of the PsV intensities was plotted. The intensity distribution of PsVs on membrane sheets from CD151-GFP transfected cells is slightly right-shifted compared to the intensity distribution of PsVs from control cells (Figure 11A), indicating that more PsVs have a high intensity in CD151-transfected cells. To analyze the number of CD151 maxima surrounding the PsVs, a circular 425 nm in diameter ROI was placed onto each PsV maximum and the CD151 maxima within this region were counted. Additionally, this analysis was performed on horizontally and vertically flipped (randomized) images as control. Both, in CD151-GFP transfected and in control cells about 2.5 CD151 maxima were counted in this narrow PsV surrounding. In the flipped control only 2 CD151 maxima were counted in this region. In CD151 transfected cells significantly more CD151 maxima were counted in the original data compared to the flipped control (Figure 11B). To further analyze the L1/CD151 association, the distance between each L1 maximum and its next nearest CD151 maximum was calculated. Therefore, a horizontal and a vertical linescan (31 pixels long × 3 pixels width) was placed on every maximum position. A Gaussian distribution was fitted to the intensity distribution of each maximum. Only PsV maxima where the best fit exhibits a fit quality of $R^2 > 0.8$ and if the Gaussian maximum locates central to the intensity distribution the maximum is included in the further analysis. Based on a circular 125 nm diameter ROI at the PsV and CD151 maxima positions, the center of mass of fluorescence was determined, yielding the maxima positions in sub-pixels. Based on these positions the shortest distance of a PsV maximum to the nearest CD151 maximum was calculated. The same analysis was performed on horizontally and vertically flipped (randomized) images as control. The average shortest distance in control cells is 81 nm whereas in CD151-GFP transfected cells the shortest distance averages at 100 nm. In flipped images the distance is 133 nm and 140 nm, respectively. For both, in control and CD151-GFP transfected cells, the distance is significantly lower in the original analysis compared to the flipped analysis. Additionally, the shortest distance from a PsV maximum to the nearest CD151 maximum is significantly lower in control cells compared to CD151-GFP transfected cells (Figure 11C). This can be explained by the larger maxima size of CD151 maxima (Figure 11C) in CD151-transfected cells. Next, the fraction of PsVs that are closely associated with CD151 was determined. As criteria for close association, a distance of 80 nm between PsV and CD151 maxima was defined, as this value was close

to the resolution limit of the microscope used. In control cells 59% of PsVs have a close association to CD151 and in CD151 transfected cells 43%, which is significantly lower. This can be explained by the larger average distance between PsVs and CD151 based on the larger maxima size of CD151 in CD151-GFP transfected cells. However, the fraction of closely associated PsVs in the original data is significantly higher in both control and CD151 transfected cells, compared to the flipped control where the fraction is 25% and 30%, respectively (Figure 11D). For better visualization of the distance between a PsV and its nearest CD151 maximum, examples are shown in Figure 11E.

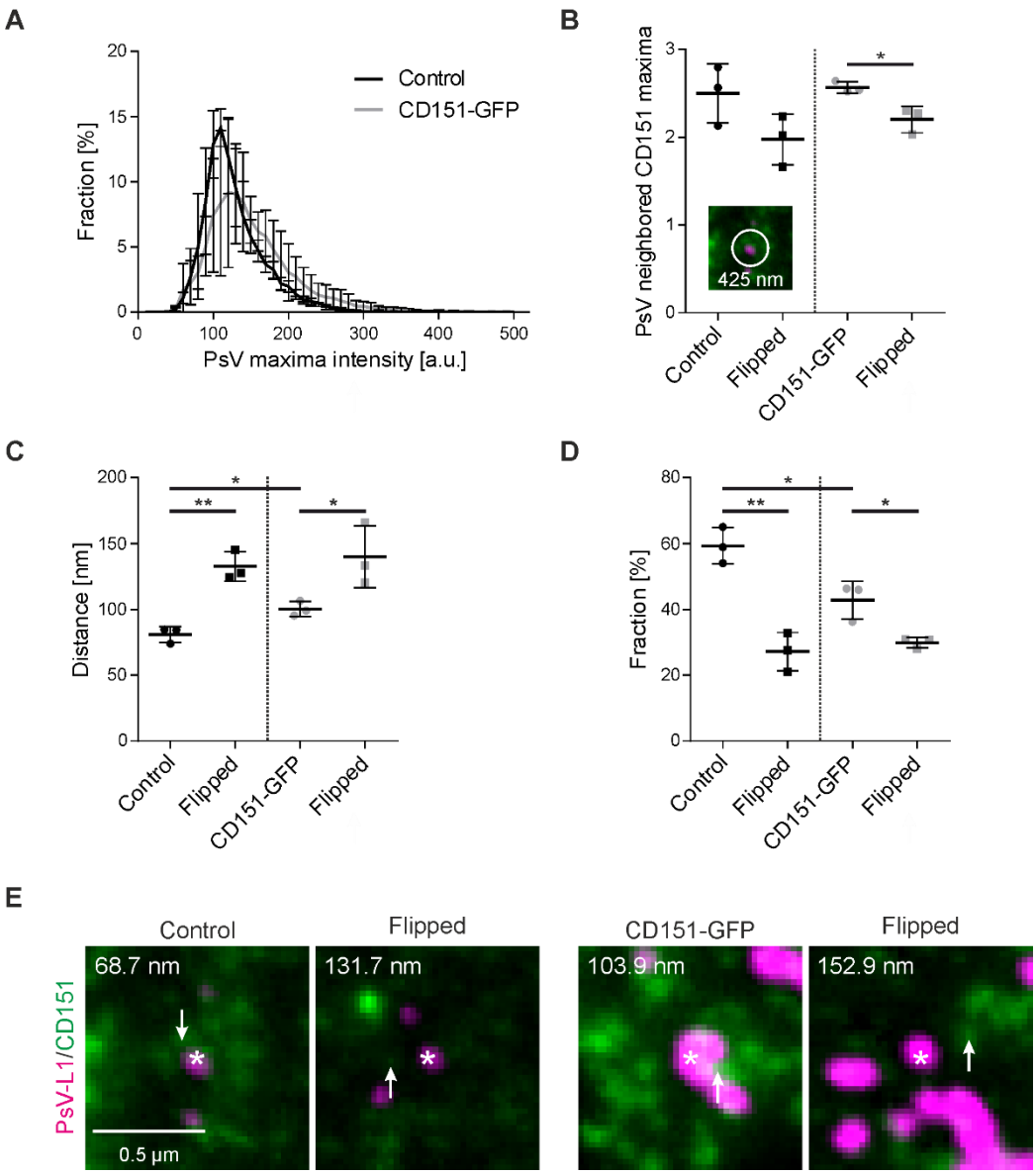

Figure 11. Analysis of the association between PsVs and CD151 during CD151 overexpression.
(A) PsV maxima were detected, and their intensities were quantified in a circular 125 nm diameter ROI, followed by background correction. The fraction of PsVs, expressed in percent, is plotted against the maxima intensity. (B) At every PsV position, a circular 425 nm ROI was positioned and the CD151 maxima were counted in original and flipped images. (C) Average shortest distance between a PsV maximum and its next nearest CD151 maximum over time. (D) The fraction of closely associated PsVs

(PsV maxima with a distance ≤ 80 nm to the next nearest CD151 maximum) was analyzed on original and flipped images. (E) Two examples of PsVs (each marked by an asterisk) taken from the control (left) and CD151-GFP (right) conditions. Number in the upper left, the shortest distance between the PsV maximum and the next nearest CD151 maximum (marked by an arrow) is given in nm. Values are given as means ± SD (n = 3). Statistical difference between original and flipped images was analyzed by using the two-tailed, unpaired student's t test.

So far, the data shows that on membrane sheets CD151 maxima are larger in CD151-GFP transfected HaCaT cells compared to untransfected control cells (Figure 10C). Large agglomerations were not observed, different from a previous study that visualized agglomerations by GFP-tagged CD151 in intact cells (Finke et al., 2020b). Therefore, intact HaCaT cells were transfected with CD151-GFP and analyzed. Cells were treated for 3 h with or without PsVs. Afterwards, cells were fixed and stained for PsVs via click-chemistry and the CD151-GFP signal was enhanced by adding a GFP-Booster. Confocal images were taken from the basal membrane and intracellular (Figure 12A). As in the previous study, large CD151-GFP agglomerations were observed in intact cells at the basal membrane and intracellular, regardless of a PsV treatment (Figure 12A). ROIs were placed on the cell body based on the GFP staining. In PsV treated HaCaT cells, the PCC between PsVs and CD151-GFP was calculated. At the basal membrane, the PCC is significantly higher compared to the flipped (randomized) control (PCC of 0.16 for original data compared to PCC 0.00 for flipped data) as observed in the previous experiment. In intracellular images, the PCC is significantly higher compared to the flipped control as well (PCC of 0.34 for original data and -0.05 for flipped data) (Figure 12B). This indicates a specific association between PsVs and CD151-GFP not only at the basal membrane but intracellular as well.

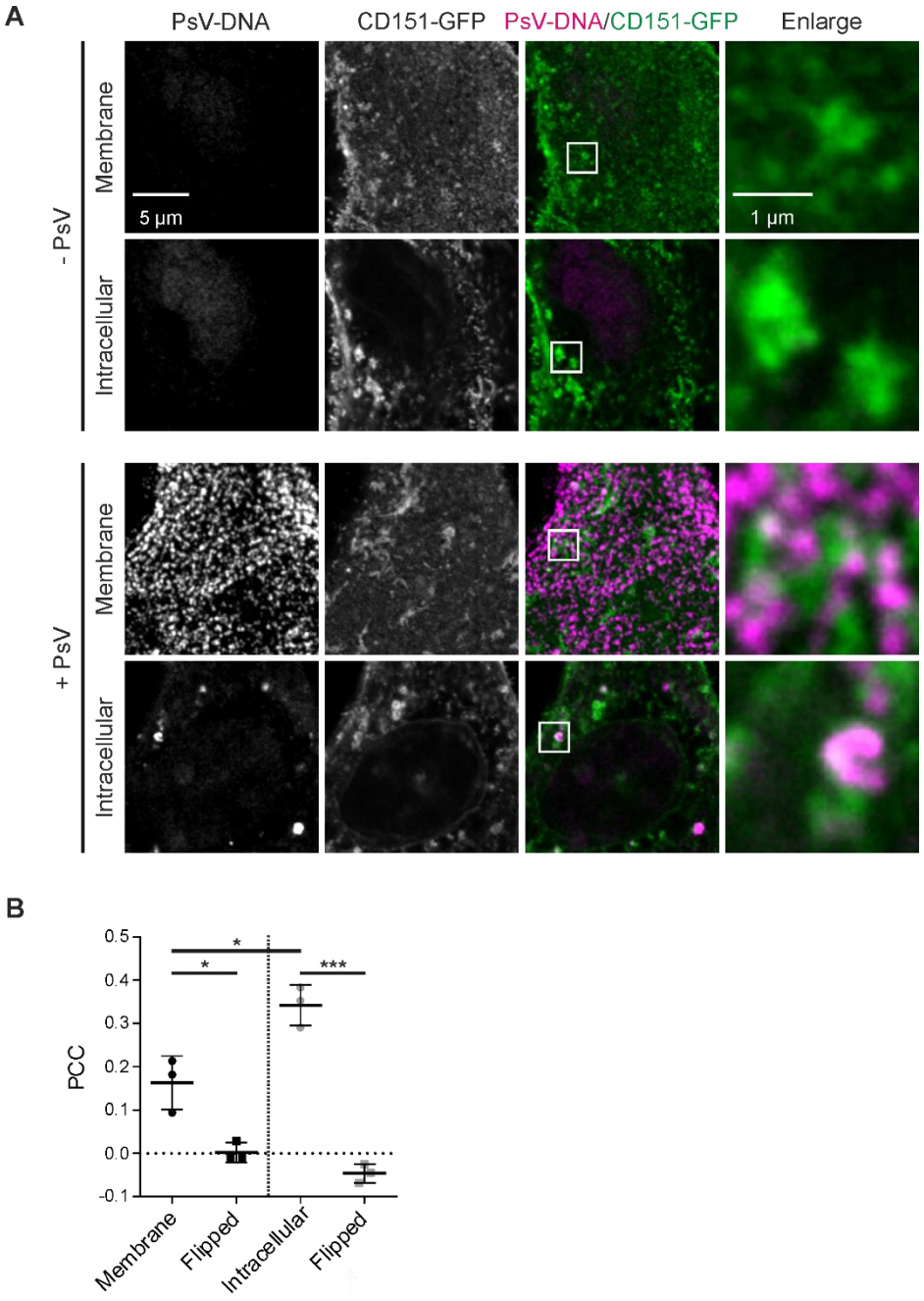

Figure 12. Effect of a CD151 overexpression on the association between PsVs and CD151 at the basal membrane and intracellular.
(A) HaCaT cells were transfected with CD151-GFP and incubated with PsVs for 3 h. Then, cells were fixed and PsVs were visualized by click-labeling of the plasmid DNA while the CD151-GFP was enhanced with GFP Booster Atto488. Images were acquired at confocal resolution. ROIs were placed on the cell body based on the GFP staining. (B) PCC between PsVs and CD151-GFP was calculated from original and flipped images. Values are given as means ± SD (n = 3). Statistical difference between original and flipped images was analyzed by using the two-tailed, unpaired student's t test.

Taken together, the data indicates a specific association between PsVs and CD151. A CD151 overexpression leads to larger CD151 maxima compared to control cells (Figure 10C). Additionally, in

CD151 transfected HaCaT cells, large CD151 agglomerations form independent of a PsV incubation (Figure 12A).

4.1.3 Impact of ErbB2 on PsV/CD151 association

Proteome analysis with additional String-db analysis of endosomal preparations in HaCaT cells treated with HPV16 PsVs, revealed the ErbB2 receptor tyrosine kinase as a potential central component in the HPV16 infection process (Mikuličić et al., 2024). To clarify whether ErbB2 has an impact on the CD151 mediated HPV16 cell entry platform formation, HaCaT cells were treated with ErbB2 inhibitor tucatinib or ErbB2 targeting siRNA and incubated with PsVs.

The ErbB2 inhibitor tucatinib inhibits the phosphorylation of ErBB2 and therefore the ErbB2 induced signaling cascade. HaCaT cells were inhibited with 1 µM or 2.5 µM tucatinib for 1 h. As a control, cells were treated only with DMSO. After the 1 h incubation, HPV16 PsVs were added and cells were incubated for additional 3 h. Cells were, fixed, sheeted, permeabilized and stained for PsVs via click-chemistry and antibody stained for CD151. Images of PsVs and CD151 were recorded in the confocal and STED mode of the microscope, respectively. As observed in previous experiments, both stainings appeared in a spotty pattern (Figure 13A). Whereas CD151 concentrated in spots scattered across the membrane sheet, the PsV staining is highly variable and appeared in spots either at the membrane sheet periphery or across the membrane sheet (Figure 13A). ROIs were placed on the membrane sheet based on the CD151 staining. The PCC between PsVs and CD151 was calculated. For all three conditions, no difference in the PCC was observed. Compared to the flipped (randomized) control, the PCC was higher in the original data. For control cells the effect was not significant because of a very high standard deviation but in tucatinib treated cells, the difference between the original data and flipped data was significant (Figure 13B). Therefore, the specific association between PsVs and CD151 was not affected by the inhibition of ErbB2. To further analyze the impact of ErbB2 on the platform formation, the PsV neighbored CD151 maxima were counted. At each PsV maximum position, a circular 925 nm diameter ROI was placed, in which the number of CD151 maxima was counted. Afterwards, the fraction of PsVs is plotted versus the number of their neighbored CD151 maxima (Figure 13C). For all conditions, a similar distribution was observed (Figure 13C), indicating that an inhibition of ErbB2 with tucatinib has no effect on PsV association with CD151.

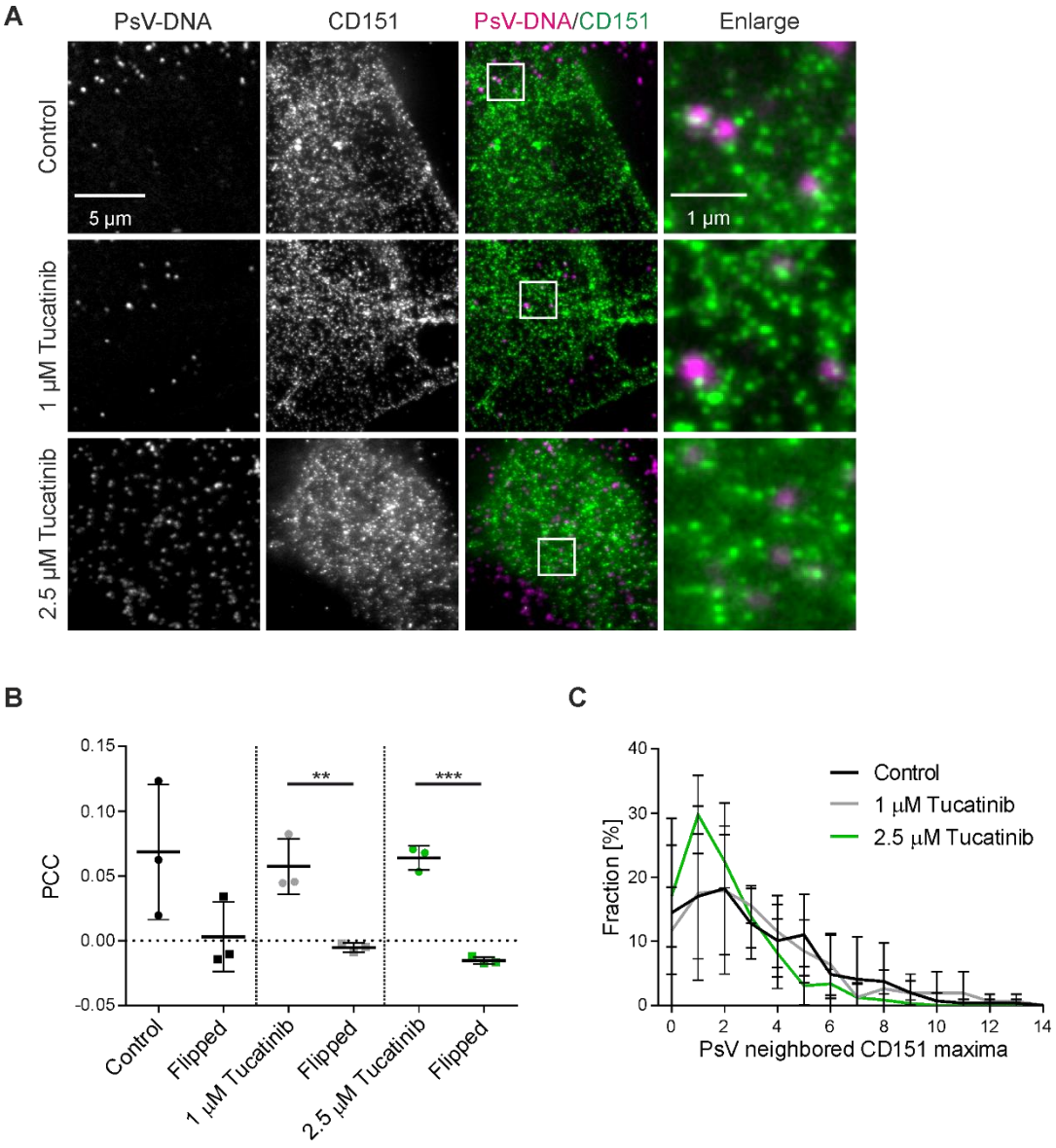

Figure 13. Effect of ErbB2 inhibition on the association between PsVs and CD151.
(A) HaCaT cells were treated with control buffer or 1 µM or 2.5 µM of the ErbB2-specific inhibitor tucatinib for 1 h prior to PsVs addition for 3 h. Then, membrane sheets were generated, fixed, permeabilized and PsVs (magenta) were visualized by click-labeling of the plasmid DNA in the confocal channel, whereas CD151 (green, STAR RED) was visualized by antibody staining in the STED channel. ROIs were placed on the membrane sheet based on the CD151 staining. (B) PCC between PsVs and CD151 was calculated from original and flipped images. (C) An image algorithm detects local maxima in the PsV images. At the maxima positions of the PsVs, 925 nm diameter circular ROIs were placed, in which the number of CD151 maxima were counted. The percentage of PsVs is plotted versus the number of their neighbored CD151 maxima. Values are given as means ± SD (n = 3). Statistical difference between original and flipped images was analyzed by using the two-tailed, unpaired student's t test. Figure and legend taken and modified from reference (Mikuličić et al., 2024).

Next, the effect of ErbB2 targeting siRNA on the PsV association with CD151 was analyzed. The ErbB2 targeting siRNA was previously validated (Mikuličić et al., 2024). HaCaT cells were transfected with a pool of ErbB2 targeting siRNA and incubated for 48 h. As a control, cells transfected with control siRNA

were used. Then, cells were treated with PsVs for 3 h. Cells were fixed, sheeted, permeabilized and PsVs were stained with click-chemistry whereas CD151 was antibody stained. Images of PsVs and CD151 were recorded in the confocal and STED mode of the microscope, respectively. As observed in previous experiments, both stainings appeared in a spotty pattern (Figure 14A). Whereas CD151 concentrated in spots scattered across the membrane sheet, the PsV staining is highly variable and appeared in spots across the membrane sheet (Figure 14A). ROIs were placed on the membrane sheet based on the CD151 staining. As observed before when treated with tucatinib, anti-ErbB2 siRNA has no effect on the PCC between PsVs and CD151 (Figure 14B). Additionally, there was no effect of anti-ErbB2 siRNA on the counted CD151 maxima near a PsV maximum (Figure 14C).

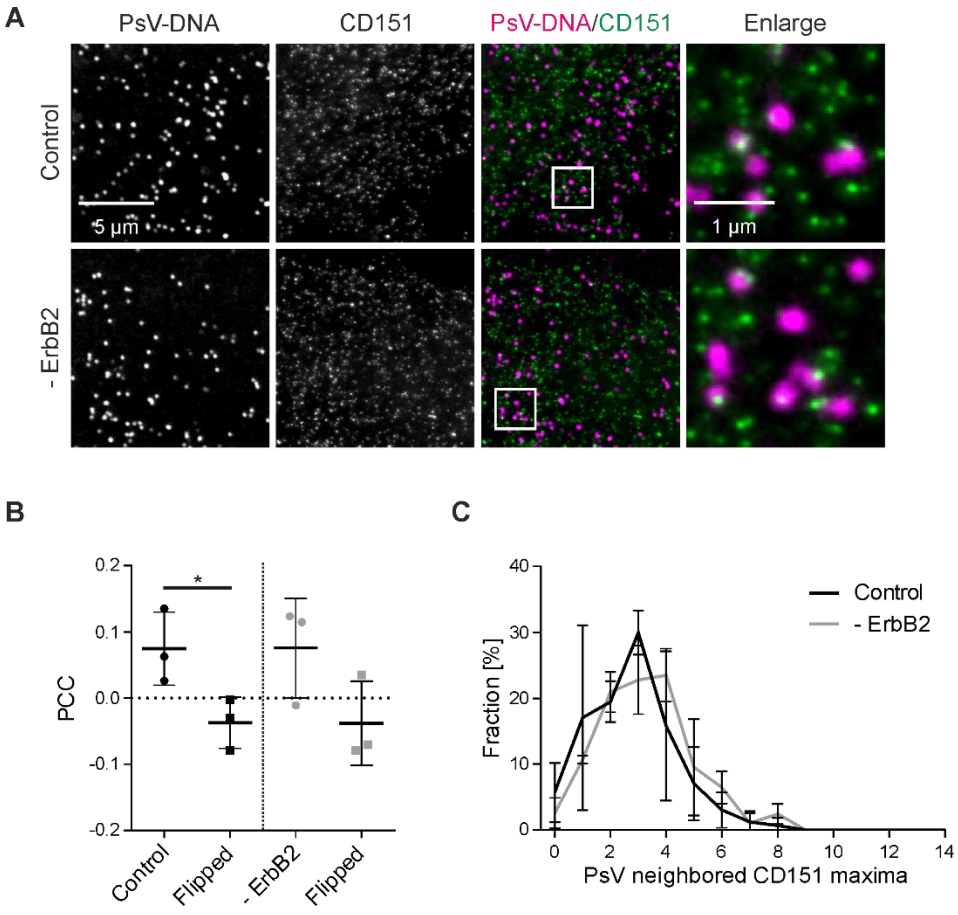

Figure 14. Effect of ErbB2 depletion on the association between PsVs and CD151.
(A) HaCaT cells were transfected either with control or ErbB2 targeting siRNA (- ErbB2) and after 48 h incubated with HPV16 PsVs for 3 h. Then, membrane sheets were generated, fixed, permeabilized and PsVs (magenta) were visualized by click-labeling of the plasmid DNA in the confocal channel, whereas CD151 (green; STAR RED) was visualized by antibody labelling in the STED channel. ROIs were placed on the membrane sheet based on the CD151 staining. (B) PCC between PsVs and CD151 was calculated from original and flipped images. (C) An image algorithm detects local maxima in the PsV images. At the maxima positions of the PsVs, 925 nm diameter circular ROIs were placed, in which the number of CD151 maxima were counted. The percentage of PsVs is plotted versus the number of their neighbored CD151 maxima. Values are given as means ± SD (n = 3). Statistical difference between

original and flipped images was analyzed by using the two-tailed, unpaired student's t test. Figure and legend taken and modified from reference (Mikuličić et al., 2024).

In both experiments, inhibiting ErbB2 with tucatinib or knocking down of ErbB2 with siRNA, there was no effect on the PCC between PsVs and CD151 and on the counted PsV neighbored CD151 maxima (within a 925 nm circular ROI placed at PsV positions). This indicates that ErbB2 inhibition/knock down had no effect on the PsV association with CD151 and on the PsV entry platform formation. In conclusion, ErbB2 signaling is not necessary for PsV entry platform formation. Therefore, ErbB2 presumably plays a role in a different step of PsV infection.

4.2 Inhibition of PsV infection by the actin inhibitor cytochalasin D

Actin dependent processes play an important role during HPV16 infection (Mikuličić, Florin, 2019, Schelhaas et al., 2012). The actin inhibitor cytochalasin D (CytD) successfully inhibits PsV infection (Schelhaas et al., 2012). CytD arrests both actin polymerization and depolymerization, destabilizing existing filaments and disrupting the integrity of cytoskeletal networks (Schliwa, 1982, Shoji et al., 2012). Through these effects, CytD is an ideal research tool for investigating actin-dependent processes like viral entry.

4.2.1 Impact of CytD on HaCaT cell shape

It is assumed that virions bind to components of the ECM and migrate by an actin-dependent transport along cell protrusions toward the cell body (Schelhaas et al., 2008, Smith et al., 2008). To block and explore the actin-dependent transport of HPV16 PsVs, the cell permeable mycotoxin and actin polymerization inhibitor CytD was used. As CytD alters cellular architecture and motility the effect on the cell shape of HaCaT cells was examined. HaCaT cells were incubated with 10 µg/ml CytD or the corresponding amount of DMSO as control for 5 h. Cells were fixed, permeabilized and antibody stained for CD151. Confocal images of the cell were taken in X,Y and X,Z direction (Figure 15). Whereas in the X,Y direction the cells had a comparable size (Figure 15, compare X,Y), in the X,Z direction, some differences were observed. Control cells looked more regular and convex shaped in the X,Z direction, with an evenly distributed cytoplasm. CytD treated cells were composed of a narrower cytoplasm with a protruded nucleus sitting on top of the cytoplasm in the X,Z direction (Figure 15, compare X,Z).
In summary, CytD treatment led to HaCaT cell rounding. However, the size of the basal membrane was only partially affected by CytD.

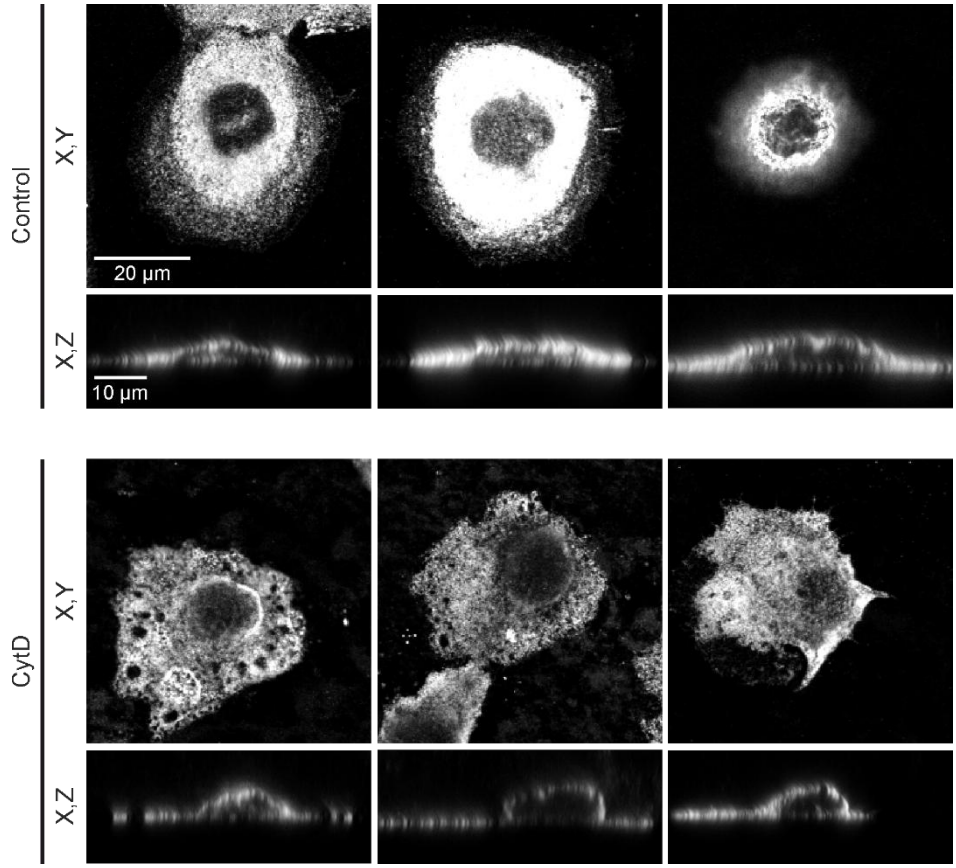

Figure 15. HaCaT cell shape upon CytD treatment.
HaCaT cells were incubated in the absence (control) or presence of 10 µg/ml CytD at 37 °C for 5 h. Then, cells were fixed and stained for CD151 (STAR RED). Confocal images were taken in the X,Y and X,Z direction.

4.2.2 Impact of CytD treatment on the PsV association with HaCaT cell surface

It has been previously shown that virions utilize actin retrograde flow to move along filopodia toward the cell body (Schelhaas et al., 2008). To analyze this process in more detail CytD was used to inhibit actin dynamics. After blocking the actin-dependent transport of PsVs to the cell body and the actin-dependent infection and endocytosis of PsVs by CytD, the PsVs were analyzed. HaCaT cells were incubated with PsVs for a total of 5 h. After 0 h (CytD), 1 h (CytD after 1 h) and 3 h (CytD after 3 h), 10 µg/ml CytD was added. The corresponding amount of DMSO was added for the whole 5 h incubation time as control. Cells were fixed, sheeted and antibody stained for L1 and CD151. Additionally, F-Actin was stained with phalloidin iFluor488. Phalloidin was imaged in the confocal and L1 and CD151 in the STED mode of the microscope, respectively. On control membrane sheets, the PsV staining appeared in spots across the membrane sheet. When CytD was added for the whole 5 h incubation time, accumulated PsV spots appeared at the periphery of the membrane sheet. Adding CytD after 1 h, some accumulated PsV spots appeared at the periphery of the membrane sheet while some PsV spots appeared scattered across the membrane sheet. When CytD was added after 3 h, the

PsVs appeared in a spotty pattern scattered across the membrane sheet (Figure 16A). The PsV intensity was quantified in a ROI covering the cell body and the cell periphery. A histogram of the PsV maxima intensities was plotted and illustrated that CytD broadens the intensity distribution toward many PsVs that are several-fold brighter than the most frequent maxima intensity of the control (Figure 16B). When CytD was added after 1 h or after 3 h, the intensity distribution was broader compared to the control and narrower compared to the intensity distribution of PsVs from membrane sheets where CytD was present during the whole 5 h incubation time (Figure 16B). After CytD treatment, PsV maxima were 40% brighter compared to the control. The accumulation of PsVs at the periphery of the membrane sheet resulted in overlapping and thus poorly resolved PsVs that appeared brighter. When CytD was added after 1 h or 3 h, PsV maxima were still 15% brighter compared to the control as some PsVs were still accumulated and therefore poorly resolved (Figure 16C).

Taken together, it appeared that CytD only arrested PsVs on their journey toward the cell surface and translocation of PsV to the cell body appeared to take longer than 1 h as some PsVs were still accumulated at the periphery of the membrane sheet when CytD was added after 1 h (Figure 16A, see arrows).

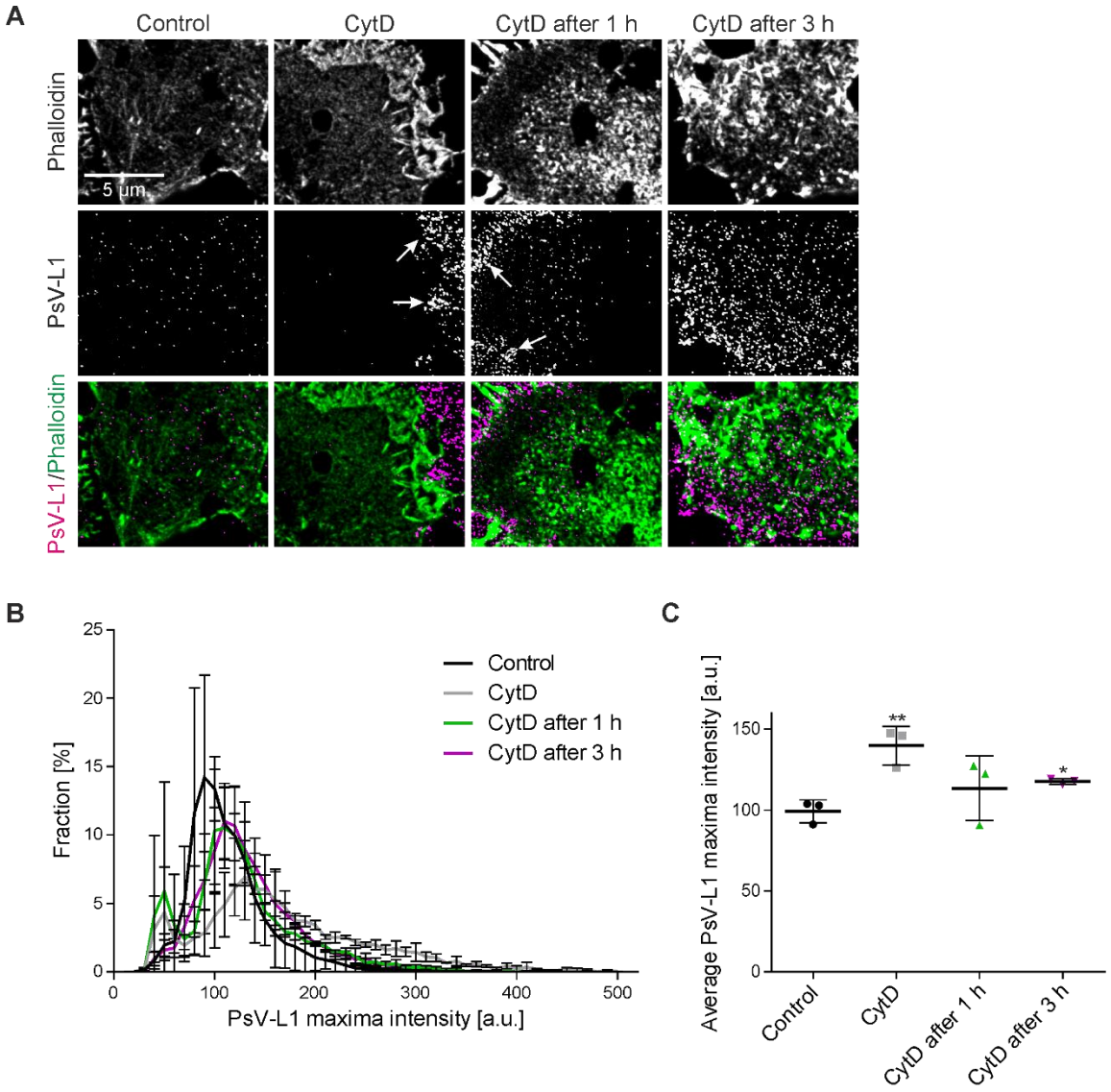

Figure 16. CytD arrests PsV translocation from the ECM to the cell body.
(A) HaCaT cells were incubated in the absence (control) or presence of 10 µg/ml CytD with PsVs at 37 °C for 5 h. In two additional conditions, CytD was added 1 h after the PsVs (CytD after 1 h) or 3 h after PsVs (CytD after 3 h). Then, cells were fixed, membrane sheets were generated, and F-actin was stained with phalloidin iFluor488 (green) and PsVs were stained by immunofluorescence using an antibody against L1 in combination with an AlexaFluor™ 594-labelled secondary antibody (magenta). Images of phalloidin and L1 were acquired in the confocal and STED mode of a STED microscope, respectively. Arrows in the magenta panels point toward accumulated PsVs. (B) PsV maxima were detected, and their intensities were quantified in a circular 125 nm diameter ROI, followed by background correction. The fraction of PsVs, expressed in percent, is plotted against the maxima intensity. (C) Average PsV maxima intensity. Values are given as means ± SD (n = 3). Statistical differences between control and CytD was analyzed by using the two-tailed, unpaired student's t test. Figure and legend taken and modified from reference (Massenberg et al., 2025).

4.2.3 Impact of CytD on PsV distribution in HaCaT cells

So far, the effect of CytD treatment on PsVs and their distribution were analyzed only on membrane sheets representing the basal membrane. In an additional experiment the PsV distribution within HaCaT cells was analyzed upon CytD treatment. Therefore, HaCaT cells were incubated with PsVs for a total of 5 h. After 0 h (CytD), 1 h (CytD after 1 h) and 3 h (CytD after 3 h), 10 µg/ml CytD was added. The corresponding amount of DMSO was added for the whole 5 h incubation time as control. Cells were fixed, permeabilized and antibody stained for Itgα6 (green). The PsVs were stained via click-chemistry (magenta). Confocal Z-Stacks were taken, starting at the basal membrane in 400 nm steps going up to 1600 nm inside the cell. A similar PsV distribution at the basal membrane was found compared to the membrane sheets from the previous experiment. In control cells, the PsV staining appeared in spots across the cell surface. When CytD was added for the whole 5 h incubation time, accumulated PsV spots appeared at the cell periphery. Adding CytD after 1 h, some accumulated PsV spots appeared at the cell periphery while some PsV spots appeared scattered across the cell surface. When CytD was added after 3 h, the PsVs appeared in a spotty pattern scattered across the cell surface (Figure 17A, basal membrane). In control cells and cells with CytD added after 3 h, PsV spots were visible in all cell sections, although only a few PsVs were found in sections + 1200 nm and + 1600 nm. In cells treated with CytD for the whole 5 h incubation time, no PsVs were found in cell sections above + 800 nm. The most PsVs were found in cell sections above + 800 nm in cells treated with CytD after 1 h (Figure 17A). The PsV distribution throughout the cell sections was calculated based on the whole image. Therefore, a threshold was adjusted for every image, and the integrated density was calculated from the binary images and background corrected. To exclude any scattered light from other cell sections, only the cell sections from the basal membrane, + 800 nm and + 1600 nm were included in this analysis. About 70 – 80% of the total PsV signal were found at the basal membrane for all four analyzed conditions. About 5% of the PsV signal was found in the highest cell section at + 1600 nm in all conditions except the cells with CytD added after 1 h. When CytD was added after 1 h a two-fold increase of the total PsV signal was found in the cell section + 1600 nm (11%). The rest of the total PsV signal was found in the cell section + 800 nm with about 20% for all four conditions (Figure 17B).

The cell permeable mycotoxin and actin polymerization inhibitor CytD is known to inhibit endocytosis of virions ((Schelhaas et al., 2012)). This analysis indicates that CytD inhibits the PsV cell entry when added directly together with the PsVs. When CytD was added after 1 h, the endocytosis of the PsVs is inhibited and PsVs seemed to be stuck in a cell section from + 800 – 1600 nm. In control cells or when CytD was added after 3 h no stuck PsVs were found in the analyzed cell sections, indicating that PsVs may be found in other cell sections of the cell, probably deeper inside the cell as the PsVs were able to reach a later step of the cell entry process.

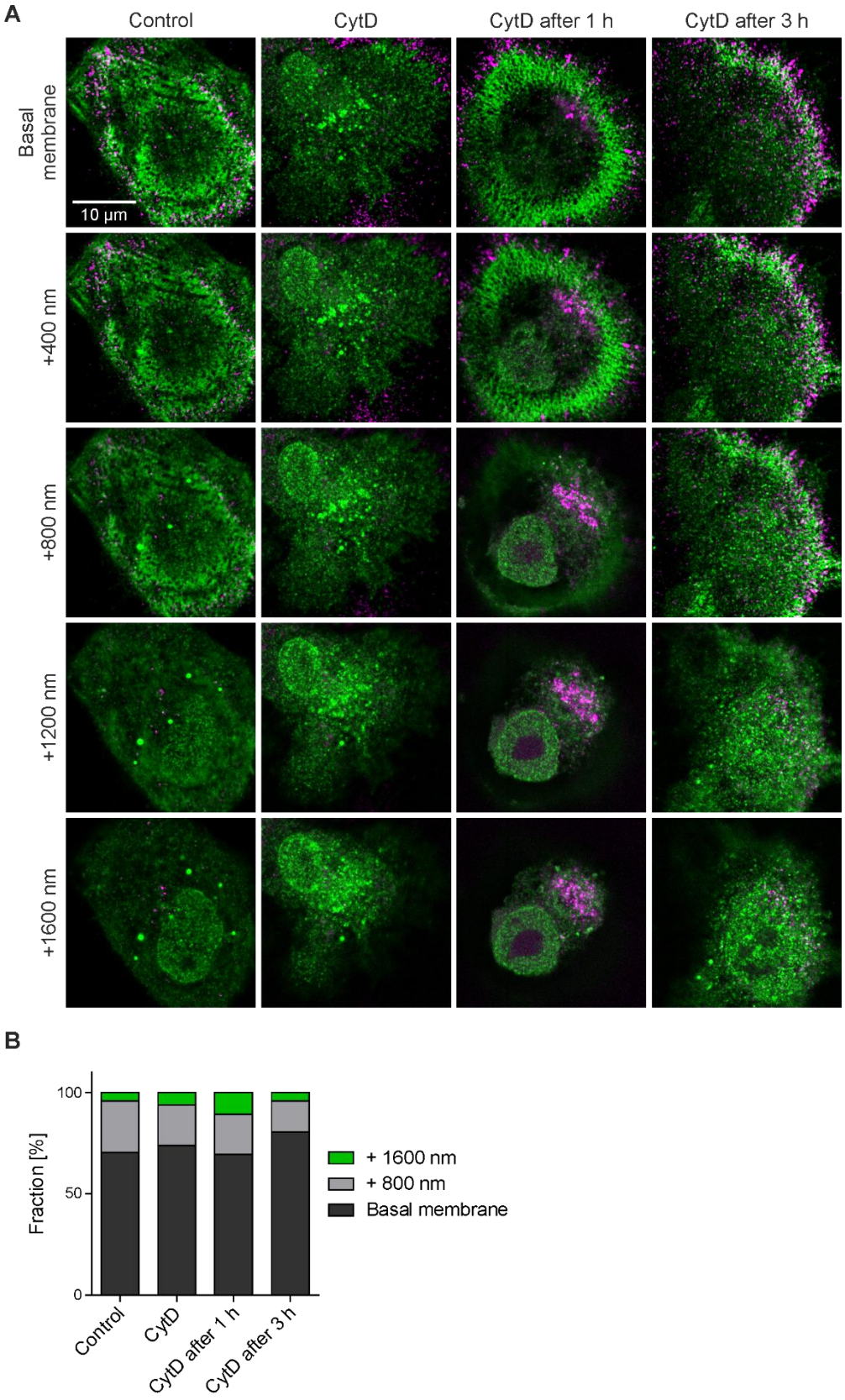

Figure 17. Distribution of PsVs in HaCaT cells during inhibition of PsV infection.
(A) HaCaT cells were incubated in the absence (control) or presence of 10 µg/ml CytD with PsVs at 37 °C for 5 h. In two additional conditions, CytD was added 1 h after the PsVs (CytD after 1 h) or 3 h

after PsVs (CytD after 3 h). Then, cells were fixed, and PsVs (magenta) were visualized by click-chemistry (6-FAM Azid) and indirect immunolabeling was used for Itgα6 (green; AlexaFluor™ 594). Cells were scanned with 400 nm steps in the axial direction at confocal resolution, starting at the basal membrane. (B) The PsV distribution throughout the cell sections was calculated. To exclude any scattered light from other cell sections, only the cell sections from the basal membrane, + 800 nm and + 1600 nm were included in this analysis.

4.3 Analysis of the PsV/CD151 and PsV/HS association after CytD wash off

So far it was shown that CytD treatment resulted in PsVs trapped in the ECM area. In the following subsequent experiments, it should be tested if PsVs would continue their journey toward the cell body after CytD removal. Within this experimental setup the relationship between actin-dependent transport and CD151 association in HPV infection should be analyzed, exploring the onset of PsV translocation from the ECM onto the cell body.

4.3.1 Binding of PsVs to detached HaCaT cells

HPV16 presumably binds to HS located at the ECM. In previous experiments it was shown that HPV16 PsVs localize at the ECM when the translocation of PsVs onto the cell body was inhibited. To analyze this effect, the PsV maxima density on the cell body was calculated in control and CytD treated cells (Figure 18A and B). For analysis, rectangular ROIs were placed onto the images that covered the cell body. In CytD treated cells only few PsVs were visible at the cell body (0.14 PsVs/μm^2), whereas a several-fold larger PsV density was observed on the cell body. This is expected, as in the control the PsVs bind to the ECM and translocate to the cell body. But do PsVs directly bind to HSPGs of the cell and glycocalyx? To clarify this, detached HaCaT cells were incubated under constant rotation with PsVs for 1 h at 4 °C. Afterwards, the cells were collected and let sit onto coverslips for 1 h. Then, cells were fixed and antibody stained for L1 (magenta) and F-actin (green) (Figure 18C). The PsV maxima density on the cells was calculated (Figure 18D) and resulted in 1.7 PsV maxima/μm^2.

Taken together, the experiment suggests that PsVs bind more effectively when membrane surface receptors were freely accessible by diffusion as in detached HaCaTs (Figure 18C and D). However, under the assay conditions used throughout the experiments, PsVs cannot easily bypass the translocation step from the ECM to the cell body by directly diffusing to the basal membrane (Figure 18A and B). Consequently, the vast majority of PsVs that successfully entered the cell were initially bound to the ECM, relying on active transport mechanisms for their progression toward the cell body.

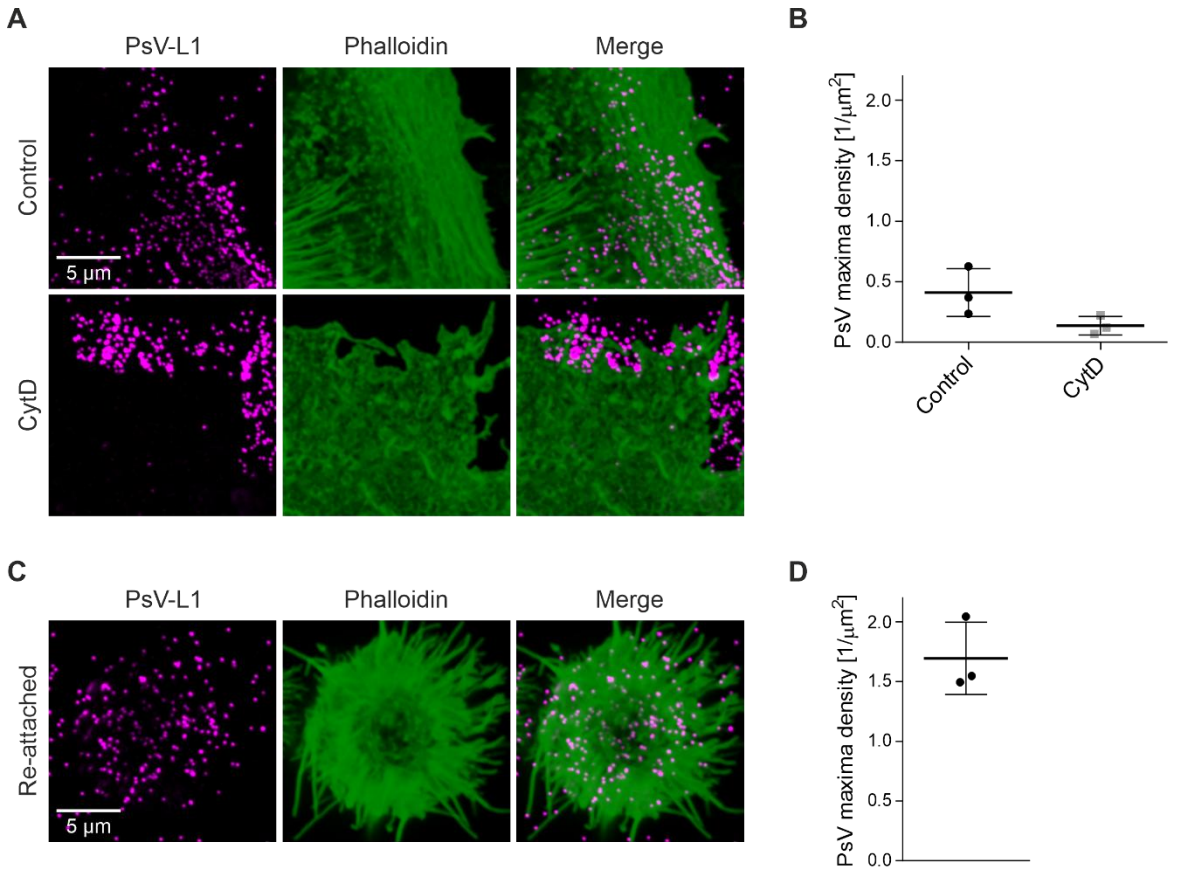

Figure 18. Binding of PsVs to substrate-adhered grown and re-attached HaCaT cells.
(A) HaCaT cells were treated with and without 10 µg/ml CytD for 5 h. Afterwards, cells were fixed and stained by indirect immunofluorescence for L1 (magenta; STAR GREEN) and for F-actin by fluorescent labelled phalloidin (green; iFluor647). For analysis, rectangular ROIs were placed onto the images that covered the cell body. (B) Within these ROIs the PsV maxima density was calculated. (C) HaCaT cells were detached by a 15 min incubation with 10 mM EDTA (in PBS) and incubated with PsVs at 4 °C for 1 h under constant rotation. Afterwards, cells were washed three times with PBS and seeded onto PLL-coated glass coverslips for 1 h. Cells were washed two-times with PBS, fixed and stained by indirect immunofluorescence for L1 (magenta; STAR GREEN) and for F-actin by fluorescent labelled phalloidin (green; iFluor647). PsVs (L1 staining) and F-actin were imaged in the confocal mode of a STED microscope. For analysis, rectangular ROIs were placed onto the images that covered the cell body. (D) Within these ROIs the PsV maxima density was calculated. Values are given as means ± SD (n = 3). Figure and legend taken and modified from reference (Massenberg et al., 2025).

4.3.2 Reversible block of PsV cell entry by CytD

In a previous experiment it was shown that CytD arrests the transport of PsVs to the cell. Additionally, CytD is known to block other actin-dependent processes, which strongly affects the physiology of the cell. Therefore, it was investigated whether PsVs would proceed normally on their infection pathway, after CytD removal followed by an additional incubation step. To this end, HaCaT cells were treated with PsVs and 10 µg/ml CytD for 5 h. After the 5 h incubation, the medium including CytD/PsVs was removed, cells were washed and incubated for another 0 min, 30 min and 60 min. Then, cells were

fixed and antibody stained for L1 (magenta). Additionally, F-Actin was stained with phalloidin iFluor647 (green). The F-actin staining appeared on the whole cell surface including filopodia, while the PsV staining was highly variable and appeared in a spotty pattern (Figure 19A). As observed in previous experiments, CytD conserved the accumulated PsVs at the cell periphery when cells were fixed immediately after CytD/PsV incubation (0 min). When cells were incubated for additional 30 or 60 min a transfer of PsVs onto the cell body was observed (Figure 19A). To further analyze this effect, the PCC between PsVs (L1) and F-actin staining was calculated (Figure 19D; CytD). For analysis, rectangular ROIs were placed onto the images that covered mainly the cell body but included parts of the cell periphery as well. At 0 min the PCC between PsVs and F-actin is -0.05, representing the rather exclusive stainings: PsVs accumulated at the cell periphery and the F-actin staining on the cell body. After 30 min the PCC increases to 0.03 until it reaches 0.09 after 60 min, indicating the transfer of PsVs onto the cell body (Figure 19D; CytD). Since PsVs are bound by electrostatic forces to HS at the primary attachment site in the ECM, the virions cannot simply dissociate and diffuse to the secondary receptor complex. However, the trypsin-like serine protease kallikrein-8 subsequently cleaves L1 which presumably allows access of further proteins. Cyclophilins expose the N-terminal part of L2 and an N-terminal proximal peptide of L2 is cleaved off by furin (Becker et al., 2018, Bienkowska-Haba et al., 2009, Cerqueira et al., 2015, Feng et al., 2024, Richards et al., 2006). Therefore, in additional samples the effect of the KLK8 inhibitor leupeptin and the Furin inhibitor I on the transfer of PsVs from the ECM to the cell body was analyzed. To this end, HaCaT cells were treated with PsVs and 10 µg/ml CytD with either 100 µM leupeptin (Figure 19B) or 5 µM Furin inhibitor I (Figure 19C) for 5 h. After the 5 h incubation, the medium including CytD/inhibitors/PsVs was removed, cells were washed and incubated for another 0 min, 30 min and 60 min. Then, cells were fixed and antibody stained for L1 (magenta). Additionally, F-Actin was stained with phalloidin iFluor647 (green). With addition of the KLK8 inhibitor leupeptin, PsVs remained accumulated at the cell periphery even after removal of CytD and the inhibitor (Figure 19B) and the PCC between PsVs and F-actin ranges between -0.04 and -0.05 at all three time points (Figure 19D; Leupeptin). With addition of Furin inhibitor I, PsVs only remain accumulated at the cell periphery at 0 min with a PCC of -0.06. After 30 and 60 min, many PsVs were found on the cell body (Figure 19C) and the PCC between PsVs and F-actin increases to 0.00 after 30 min and up to 0.05 after 60 min (Figure 19D).

Taken together, after treatment with CytD and Leupeptin with a subsequent removal, PsVs remained accumulated at the cell periphery and the transfer onto the cell body seemed to be blocked. Whereas, with CytD only and CytD with Furin inhibitor I, PsVs were transferred onto the cell body.

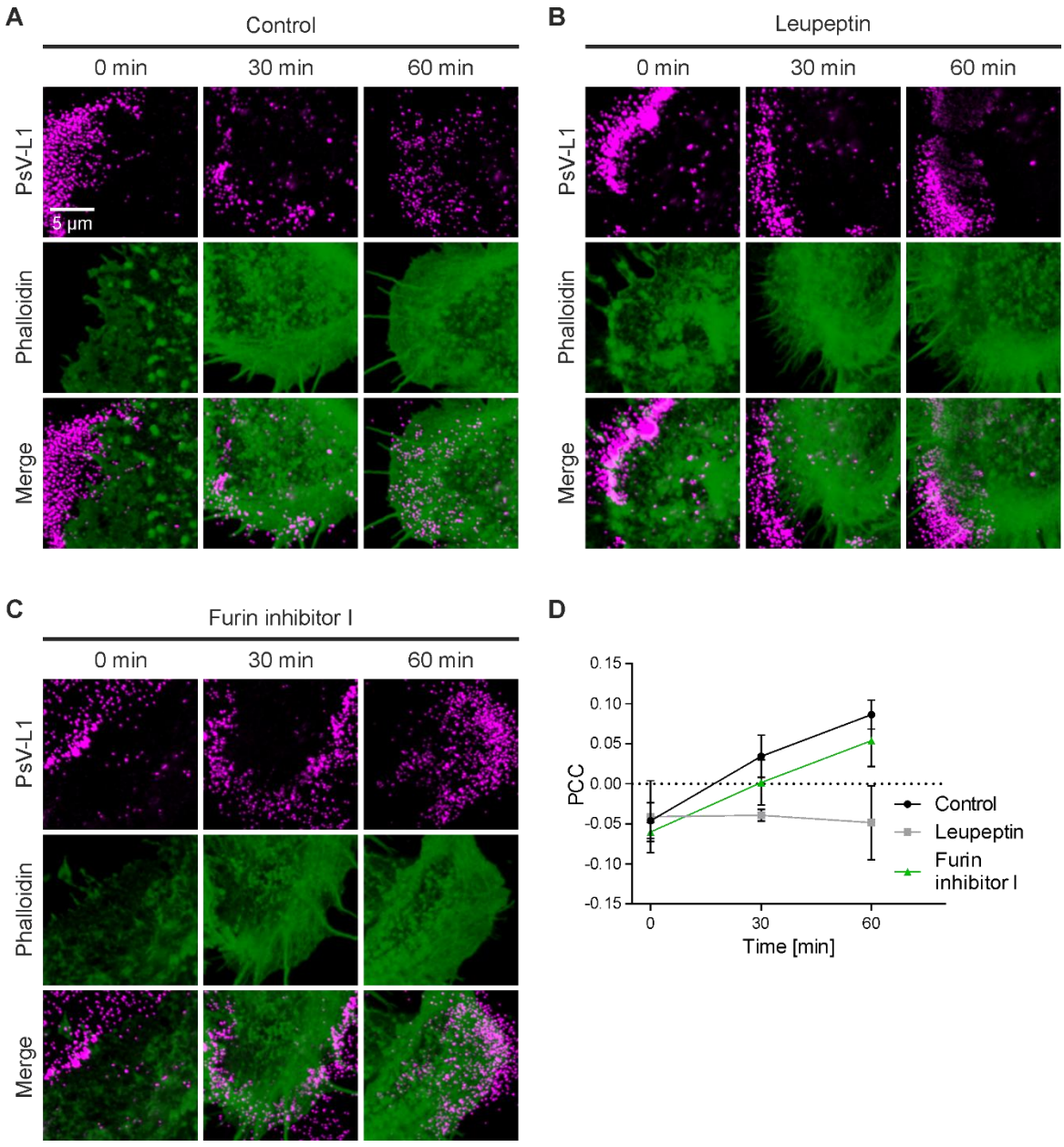

Figure 19. Transfer of PsVs from the ECM onto the cell body.
HaCaT cells were incubated with PsVs at 37 °C for 5 h, in presence of PsVs and (A) 10 µg/ml CytD (CytD) (B) 10 µg/ml CytD and 100 µM Leupeptin (Leupeptin) (C) 10 µg/ml CytD and 5 µM Furin inhibitor I (Furin inhibitor I). Afterwards, cells were washed and incubated without PsVs/CytD/inhibitors further for 0 min, 30 min or 60 min. Cells were fixed and stained by indirect immunofluorescence for L1 (magenta; STAR GREEN) and for F-actin by fluorescent labelled phalloidin (green; iFluor647). PsVs (L1 staining) and F-actin were imaged in the confocal mode of a STED microscope. For analysis, rectangular ROIs were placed onto the images that covered mainly the cell body but included parts of the cell periphery as well. (D) Within these ROIs, the PCC between PsV-L1 (magenta) and F-actin (green) was calculated and plotted over time. Values are given as means ± SD (n = 3). Statistical difference between CytD and CytD/inhibitors was analyzed by using the two-tailed, unpaired student's t-test. Figure and legend taken and modified from reference (Massenberg et al., 2025).

4.3.3 Impact of CytD on protease cleavage and HS

As mentioned before, accumulated virions bound to HS in the ECM cannot dissociate from their primary attachment site. Next to the L1 cleavage by KLK8 and a subsequent cleavage of L2 by Furin, another 'release' mechanism was postulated. However, both models are not mutually exclusive. In the alternative model, virions are released by normal HSPG processing and protease cleavage (Surviladze et al., 2012). Therefore, the potential impact of CytD treatment on protease activity was analyzed. To this end, an antibody was used that specifically recognizes the neo-epitope created after heparinase cleavage (clone 3G10) (David et al., 1992, Yokoyama et al., 1999). HaCaT cells were treated with PsVs and 10 µg/ml CytD for 5 h. As a control, cells were treated with PsVs with the corresponding amount of DMSO. After the 5 h incubation, the medium including CytD/DMSO and PsVs was removed, cells were washed and incubated for another 0 min, 30 min, 60 min and 180 min. Then, cells were fixed and antibody stained for L1 (magenta) and Δ-HS (cyan), Additionally, F-Actin was stained with phalloidin iFluor647 (green). The Δ-HS staining appeared in a spotty pattern scattered across the whole cell in all conditions (Figure 20A). Additionally, no difference in the Δ-HS intensity was observed (Figure 20B).

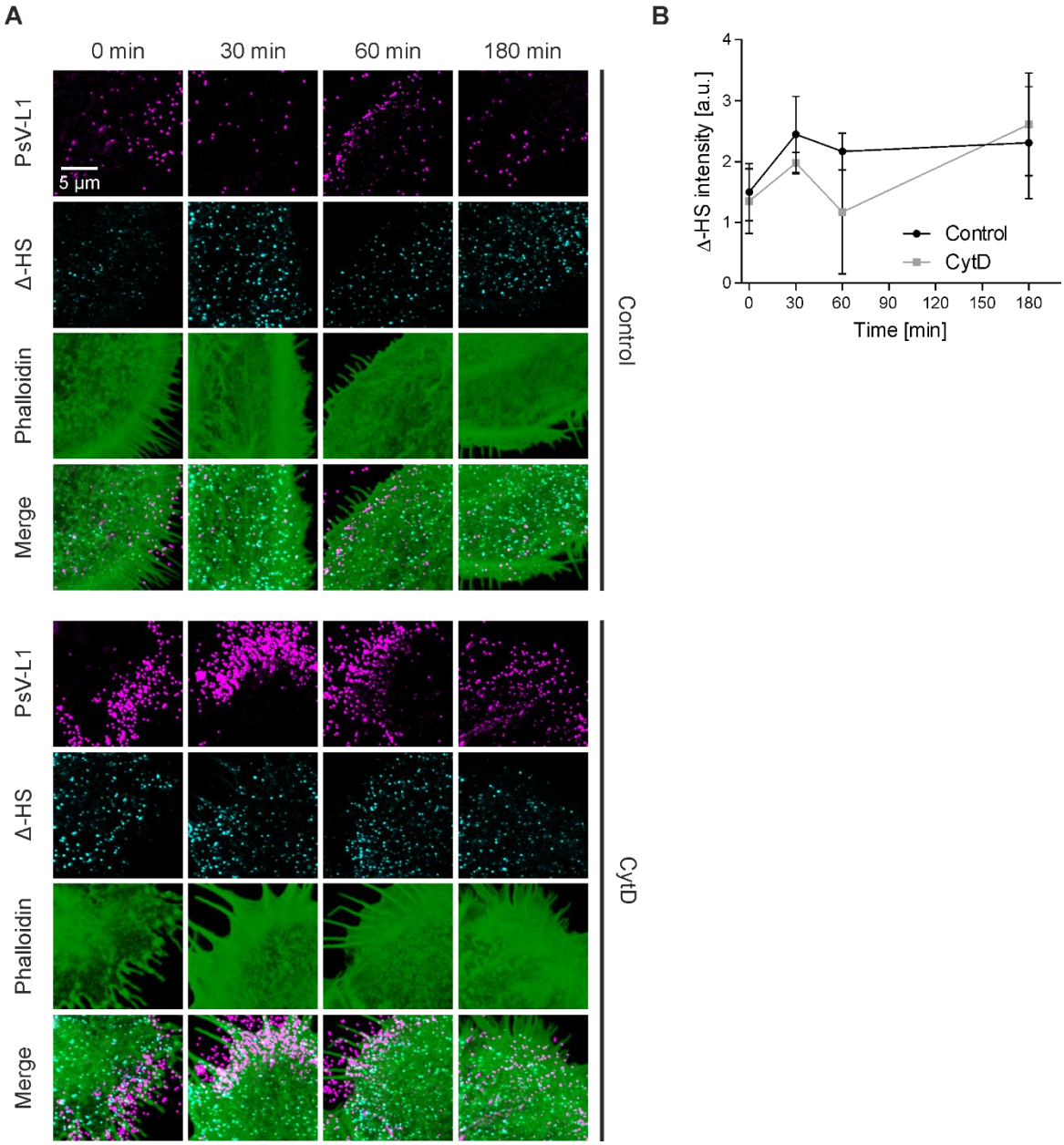

Figure 20. Δ-HS intensity after CytD treatment.
(A) HaCaT cells were incubated with PsVs at 37 °C for 5 h, in the absence (control, upper panels) or presence of 10 µg/ml CytD (CytD, lower panels). Afterwards, cells were washed and incubated further without PsVs/CytD for up to 180 min, before they were fixed and stained. Immunofluorescence was used for L1 (magenta; STAR GREEN) and for Δ-HS (cyan; AlexaFluor 594) staining. F-actin was stained by fluorescent labelled phalloidin (green; iFluor647). PsVs (L1 staining), Δ-HS and F-actin were imaged in the confocal mode of a STED microscope. For analysis, rectangular ROIs were placed onto the images that covered mainly the cell body but included parts of the cell periphery as well. (B) Average Δ-HS intensity over time. Values are given as means ± SD (n = 3). Statistical difference between control and CytD was analyzed with two-tailed, unpaired student's t test. Figure and legend taken and modified from reference (Massenberg et al., 2025).

During ECM processing by proteases and heparanase, HS is cleaved and HS fragments are released (Elkin et al., 2001). In the next experiment it was tested if HS fragments bind to PsVs accumulated in

the ECM. HaCaT cells were treated with and without PsVs and 10 µg/ml CytD for 5 h. As a control, cells were treated with and without PsVs with the corresponding amount of DMSO. Then, cells were fixed and antibody stained for L1 (magenta) and HS (cyan), Additionally, F-Actin was stained with phalloidin iFluor647 (green). The PsV staining was only visible when cells were incubated with PsVs. In control cells the PsVs appeared in a spotty pattern scattered across the cell. In CytD treated cells, the PsVs appeared accumulated at the cell periphery (Figure 21A). The HS staining was variable but mostly located adjacent to the cell (Figure 21A). Furthermore, the HS intensity was calculated. For analysis, rectangular ROIs were placed onto the images that covered mainly the cell body but included parts of the cell periphery as well. In cells treated with PsVs and CytD the HS intensity was significantly higher compared to control cells, while PsVs or CytD treatment alone had no effect (Figure 21B).

In conclusion, CytD treatment had no effect on HS cleavage. Additionally, HS cleavage products may remain on accumulated PsVs trapped in the ECM after CytD treatment.

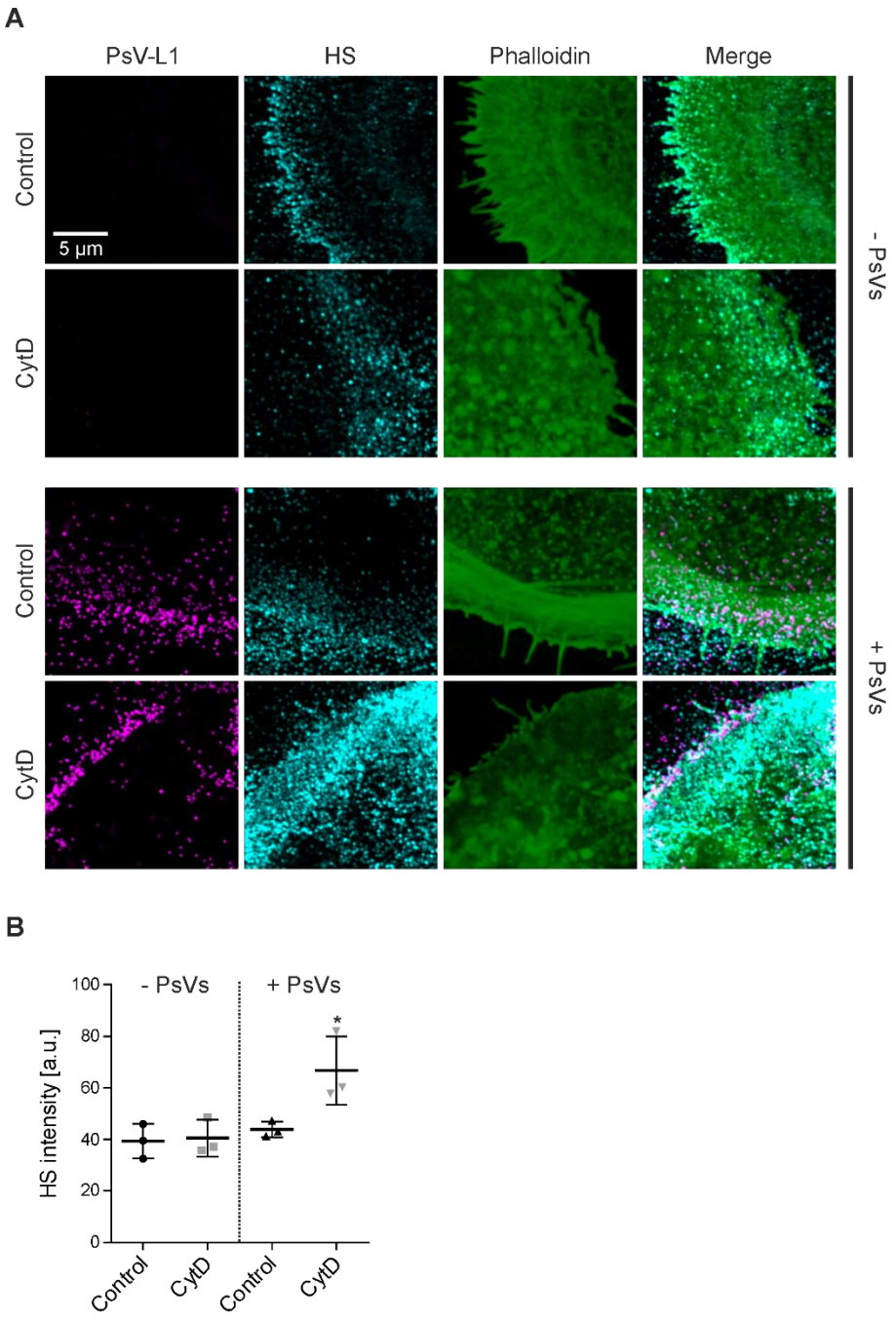

Figure 21. HS intensity after CytD treatment.
HaCaT cells were incubated with and without PsVs at 37 °C for 5 h, in the absence (control, upper panels) or presence of 10 µg/ml CytD (CytD, lower panels). Afterwards, cells were washed, fixed, and stained. Immunofluorescence was used for L1 (magenta; STAR GREEN) and for HS (cyan; AlexaFluor 594) staining. F-actin was stained by fluorescent labelled phalloidin (green; iFluor647). PsVs (L1 staining), HS and F-actin were imaged in the confocal mode of a STED microscope. For analysis, rectangular ROIs were placed onto the images that covered mainly the cell body but included parts of the cell periphery as well. (B) Average HS intensity over time. Values are given as means ± SD (n = 3). Statistical difference between control and CytD was analyzed by using the two-tailed, unpaired student's t test. Figure and legend taken and modified from reference (Massenberg et al., 2025).

4.3.4 Association of PsVs and CD151 after CytD wash off

The association between PsVs and CD151 and the time course of PsV transfer from the ECM to the cell body was analyzed upon CytD treatment and subsequent removal. To this end, HaCaT cells were treated with PsVs and 10 µg/ml CytD for 5 h. As a control, cells were treated with PsVs with the corresponding amount of DMSO. After the 5 h incubation, the medium including CytD/DMSO and PsVs was removed, cells were washed and incubated for another 0 min, 30 min, 60 min and 180 min. Then, cells were fixed and antibody stained for L1 and CD151. Additionally, F-Actin was stained with phalloidin iFluor647. The CD151 staining concentrated in spots scattered across the cell surface. At 180 min/CytD some CD151/PsV agglomerations were observed. (Figure 22A, marked with arrows 180 min/CytD). The antibody staining against PsVs was highly variable. CytD conserved the accumulated PsVs at the cell periphery and at early time points PsVs appeared brighter as observed in previous experiments (Figure 22A). To analyze whether PsVs would continue their infection pathway after CytD removal and translocate onto the cell body, the time-course of the diminishment of accumulated PsVs at the cell border region was analyzed, focusing on PsVs that were very close to or already approached the cell surface. Therefore, the number of PsVs in a defined cell border region (Figure 22B for example) were counted. Compared to the control, CytD treatment resulted in a 3-fold increase of PsVs in the cell border region when cells were immediately fixed after washing off of CytD (0 min time point). After 30 – 60 min this increase was more than halved. After 60 – 180 min the level of the control was reached (Figure 22C). Hence, the half-time of PsV translocation from the cell border region further onto the cell body is about 30 min.

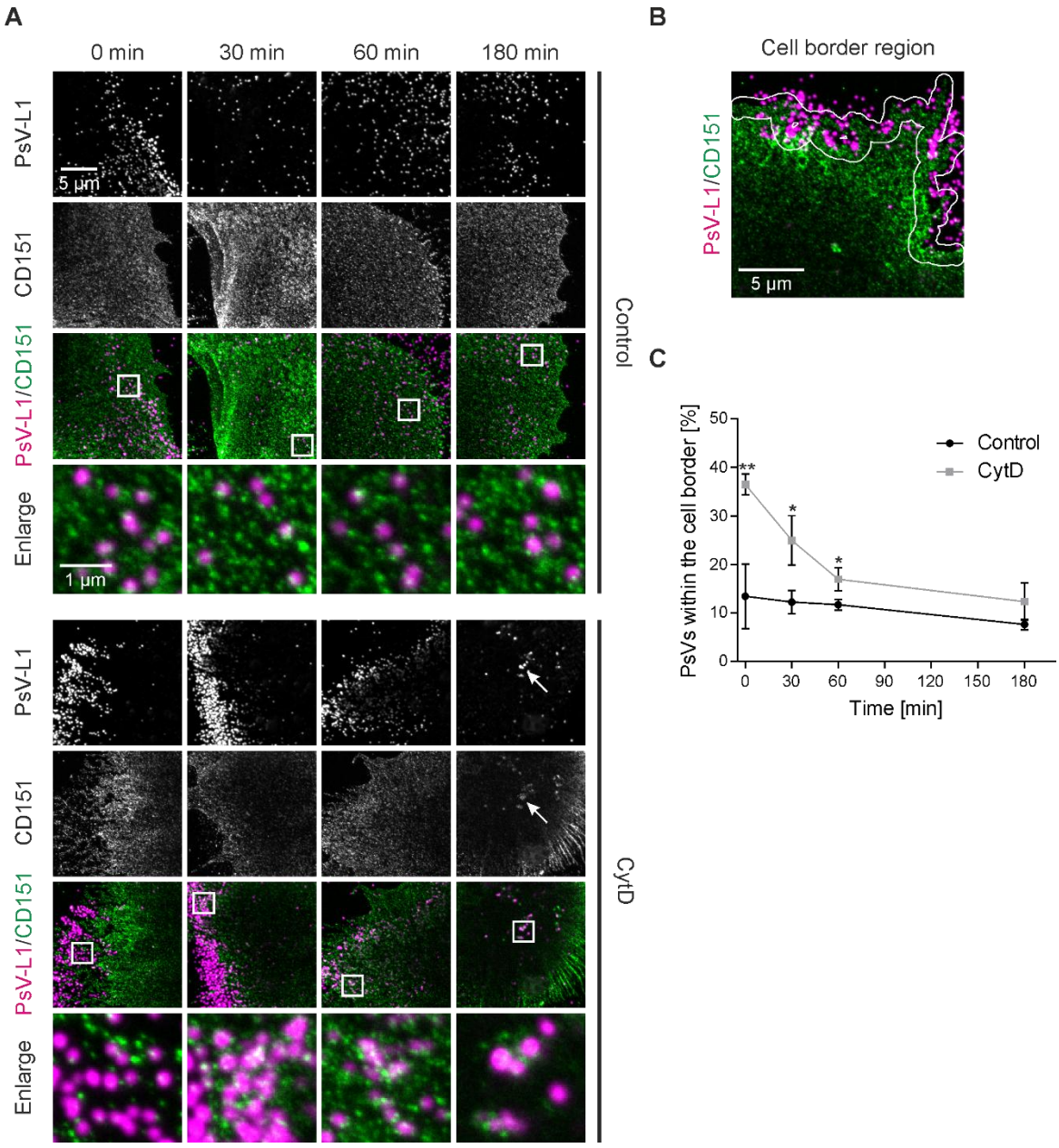

Figure 22. Association between PsVs and CD151.
(A) HaCaT cells were incubated with PsVs at 37 °C for 5 h, in the absence (control, upper panels) or presence of 10 µg/ml CytD (CytD, lower panels). Afterwards, cells were washed and incubated without PsVs/CytD further for 0 min, 30 min, 60 min or 180 min, before they were fixed and stained by indirect immunofluorescence for L1 (magenta; STAR GREEN) and for CD151 (green; AlexaFluor™ 594), and for F-actin by fluorescent labelled phalloidin (iFluor647; here not shown for clarity). The bottom rows show enlarged views of the merged images, from the regions marked by the white boxes. PsVs (L1 staining) and F-actin are imaged in the confocal and CD151 in the STED mode of a STED microscope, respectively. 180 min/CytD, arrows mark presumably endocytic structures in the central cell body region. (B) Based on the CD151 image, a cell border strip was defined and broadened by 20 pixels on each side. The analyzed cell border region covered both sides of the cell border (approximately two thirds inside and one third outside of the cell). (C) Diminishment of PsV maxima from the cell border region over time, expressed as percentage of all PsVs present in the image. Values are given as means ± SD (n = 3). Statistical difference between the same time points of control and CytD was analyzed by using the two-tailed, unpaired student's *t* test. Figure and legend taken and modified from reference

(Massenberg et al., 2025). Data analysis in (B) and (C) was kindly performed by Carl Niklas Schneider (AG Lang).

The CD151 intensity diminished after CytD removal and was halved after 180 min (Figure 23A), whereas no trend for the CD151 intensity was observed in control cells. The PCC between the PsV and CD151 channel was analyzed to study the association between PsVs and CD151. For all samples, the PCC was about 0.1, except for the 0 min/CytD value that was significantly lower and even slightly negative (Figure 23B). The negative PCC of 0 min/CytD reflected the partially mutual exclusion of the two stainings. While the PsV accumulations were located at the cell periphery, the CD151 staining mainly was at the cell body. At 30 min/CytD, the PCC reached the level of 0.1 as in the other conditions. As a control, the PCC was calculated on horizontally and vertically flipped (randomized) images as well (Figure 23D). For the control cells, the PCC was significantly higher at all time points compared to the flipped images (Figure 23E). For CytD treated cells, at 0 min/CytD the PCC of the original and flipped analysis was zero or even slightly negative. After 60 min/CytD the PCC was significantly higher in the original data compared to the flipped images (Figure 23F). Next, the shortest distance between each PsV maximum and its nearest CD151 maximum was calculated. In control cells the shortest distance was about 150 nm. At 0 in/CytD the shortest distance was about 250 nm and significantly higher compared to the control. At 30 min/CytD the shortest distance of the control was reached (Figure 23C).

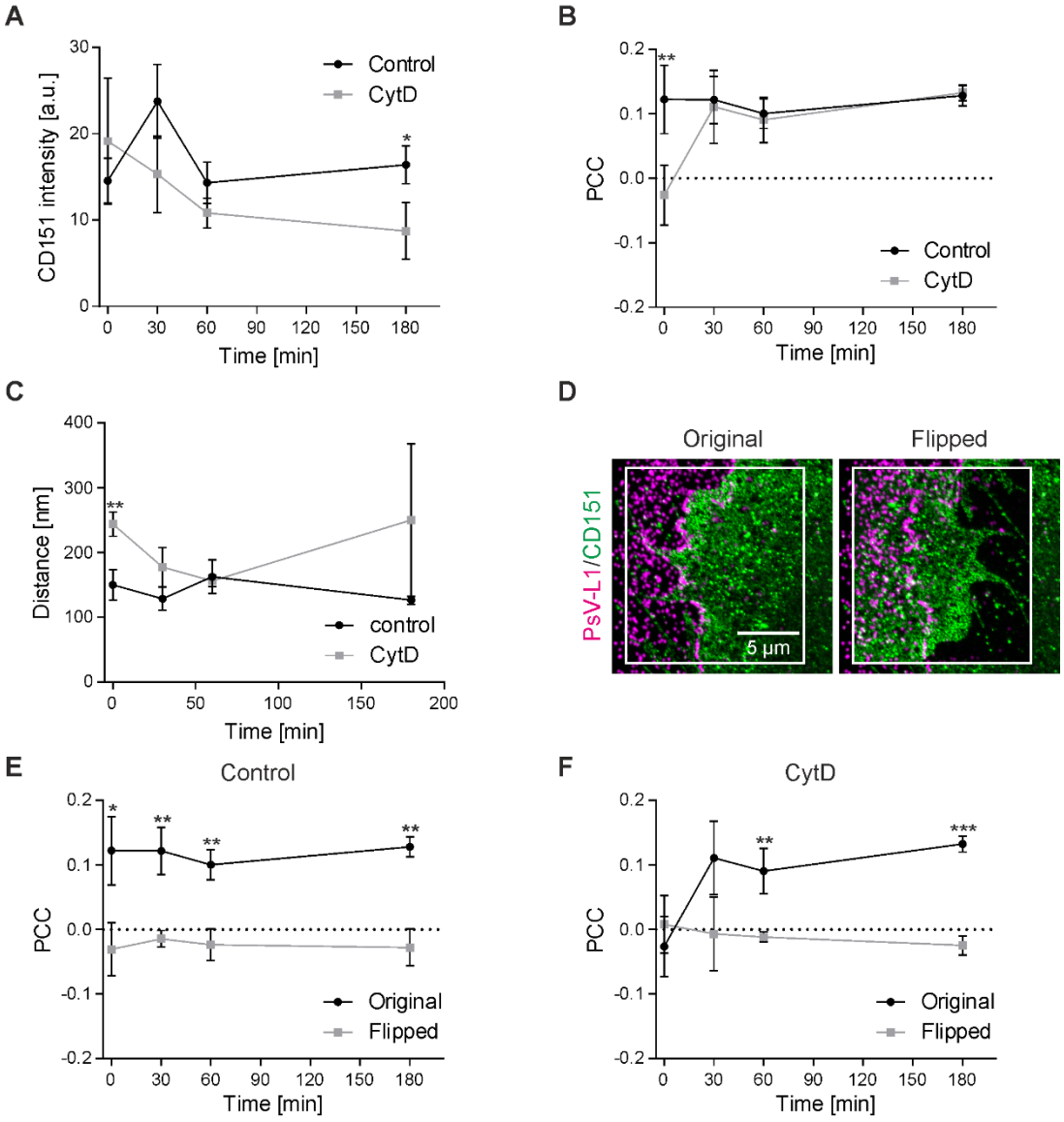

Figure 23. Analysis of the association between PsVs and CD151.
For analysis, rectangular ROIs were placed onto the images that covered mainly the cell body but included parts of the cell periphery as well. (A) Average CD151 intensity over time. (B) The PCC between PsVs and CD151 was calculated and plotted over time. (C) Average shortest distance between a PsV maximum and its next nearest CD151 maximum over time. (D) Example of a flipped CD151 image used as control. Left, original image taken from the 0 min/CytD condition. The ROI selected for analysis is shown as white box. Right, the green image within the ROI is flipped horizontally and vertically. (E) The PCC between PsVs and CD151 of the control condition is shown again, together with the respective PCCs determined on flipped images. (F) The PCC between PsVs and CD151 of the CytD condition is shown again, together with the respective PCCs determined on flipped images. Values are given as means ± SD (n = 3). Statistical difference between the same time points of original and flipped images or control and CytD was analyzed by using the two-tailed, unpaired student's t test. Figure and legend taken and modified from reference (Massenberg et al., 2025).

The fraction of closely associated PsVs with CD151 was calculated. As criterion for close association, a distance of 80 nm between PsV and CD151 maxima was defined, as this value was close to the resolution limit of the used microscope. The same analysis was performed on horizontally and vertically flipped (randomized) images, to identify random background association. In control cells the fraction was about 30% and significantly higher compared to the flipped images with about 20% (Figure 24A). At 0 min/CytD the fraction of closely associated PsVs with CD151 was about 25%. At 60 min/CytD, the level of the control cells was reached with a fraction of 30%. At 180 min/CytD, only 20% of PsVs were closely associated with CD151. In the corresponding flipped control, at 0 min/CytD about 20% of PsVs were closely associated and the fraction lowered to 10% at 180 min/CytD. However, the fraction of closely associated PsVs was significantly higher compared to the flipped images (Figure 24B). For both data sets, control cells and CytD treated cells, the fraction of closely associated PsVs with CD151 in flipped images was often more than halved compared to the original images. However, this demonstrated that a random background association occurred as many of the PsVs had a distance ≤ 80 nm to CD151 merely by chance. It was assumed that the random background association correlated with the CD151 maxima density. Therefore, the fraction of closely associated PsVs of all replicates from the flipped images was plotted against the CD151 maxima density. As assumed, the fraction increased with the maxima density. A linear regression line was fitted onto the data and described how the background association depended on the maxima density. Based on the regression line, the random background association was calculated, for any maxima density in an original image (Figure 24C). The fraction of closely associated PsVs with CD151 was corrected for random background association. In control cells the corrected fraction was about 10% and significantly higher compared to the flipped images with no remaining association (Figure 24D). At 0 min/CytD the fraction of closely associated PsVs with CD151 was about 5%. At 60 min/CytD, the level of the control cells was reached with a fraction of 10%. The fraction of closely associated PsVs was significantly higher compared to the flipped images with no remaining association (Figure 24E). Comparing the corrected fraction of control and CytD treated cells, no significant effect was analyzed as both fractions remained at 10% (Figure 24F). For better visualization of the criterion for close association, examples of the distance between a PsV and its nearest CD151 maximum are shown in Figure 24G, with one example not fulfilling the distance criterion of a distance <= 80 nm (30 min/CytD) and one fulfilling the criterion (60 min/CytD).

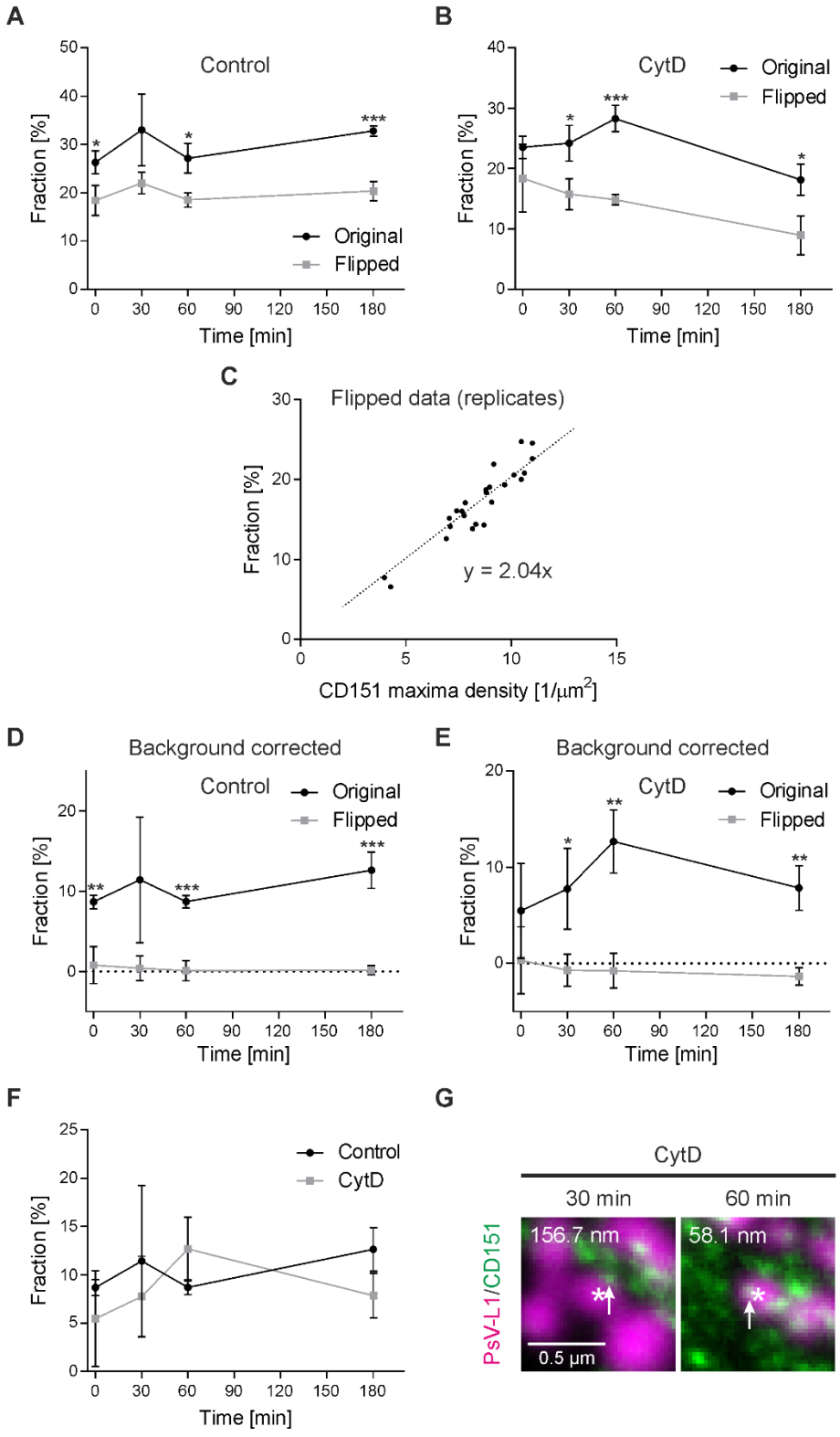

Figure 24. Background correction of the fraction of PsVs closely associated with CD151.
(A) The fraction of closely associated PsVs (PsV maxima with a distance ≤ 80 nm to the next nearest CD151 maximum) in the control was analyzed on original and flipped images. On flipped images, the fractions often were more than half of the original images. This demonstrates that many of the PsVs have a distance ≤ 80 nm to CD151 merely by chance (random background association). (B) Same as (A) for the CytD condition. (C) Each flipped data point in (A) and (B) is the average of three biological

replicates. From the altogether 24 replicates of the flipped images, the fraction of closely associated PsVs was plotted against the CD151 maxima density. As expected, the fraction increased with the maxima density. The fitted linear regression line describes how the background association depends on the maxima density. With the equation of the regression line the random background association can be calculated, for any maxima density in an original image. (D) For each replicate from the original and the flipped images in (A), the background fraction is calculated using the equation of the regression line in (C) and the respective CD151 maxima density and subtracted from the fraction of closely associated PsVs. (E) Same as (D) for the CytD condition. (F) The corrected original of the control and CytD conditions. (G) Two examples of PsVs (each marked by an asterisk) taken from the 30 min/CytD (left) and 60 min/CytD (right) conditions. Number in the upper left, the shortest distance between the PsV maximum and the next nearest CD151 maximum (marked by an arrow) is given in nm. Values are given as means ± SD (n = 3). Statistical difference between the same time points of original and flipped images or control and CytD was analyzed by using the two-tailed, unpaired student's t test. Figure and legend taken and modified from reference (Massenberg et al., 2025).

In this experiment, CD151 (green) was also present at cell protrusions that were rich in F-actin (cyan) and varied strongly in number and shape. The examples shown in Figure 25 were anecdotal images taken from the CytD condition of cells with CD151 positive filopodia. Interestingly, some of the filopodia were spiked with PsVs (magenta) as well. At 0 min/CytD the F-actin staining was weaker compared to the 30 min/CytD time point. This can be explained by the CytD incubation, affecting the F-actin and therefore the staining with a fluorophore-coupled phalloidin. However, already 30 min after CytD removal, the F-Actin recovered from the CytD treatment.

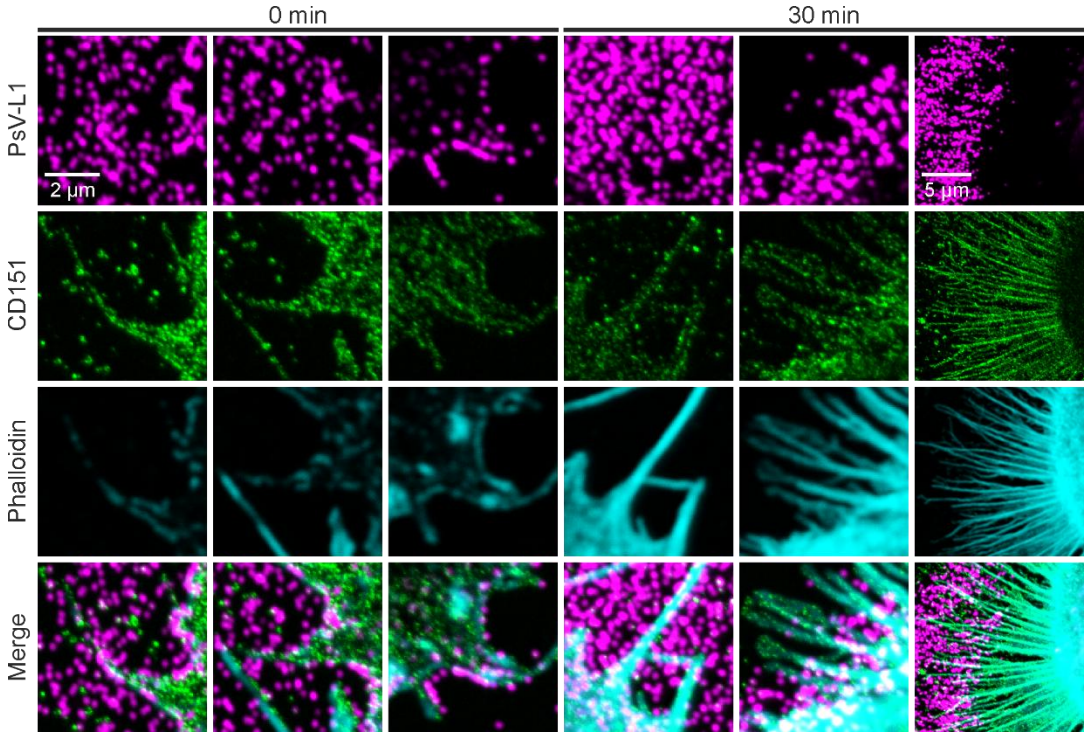

Figure 25. Gallery of images illustrating the variability of filopodia.
Images were taken from the same experiment described above. Many cells have filopodia. However, due to the large variability in number and shape it is impossible to show representative images. Therefore, the shown examples taken from the CytD condition are anecdotal images of cells with

CD151 positive filopodia. Figure and legend taken and modified from reference (Massenberg et al., 2025).

As shown in Figure 22A, large CD151/PsV agglomerations appeared at 180 min/CytD. More examples of agglomerated CD151 (green) that are associated with PsVs (magenta) are shown in Figure 26A. As these agglomerations likely are endocytic structures, cells were scanned with 400 nm steps in the axial direction at confocal resolution, starting at the basal membrane. The structures noticed at the basal membrane as agglomerated CD151/PsV continued deeper into the cell. In some cases, these endocytic structures reached more than a micrometer into the cell (Figure 26B).

Taken together, after a 5 h pre-incubation with PsVs (Figure 24F, control), about 10% of the PsVs were associated closely with CD151 in a time window of 180 min and CytD only diminished the early association at 0 min (Figure 24F, 0 min/CytD). Additionally, the PCC between PsVs and CD151 increased between 0 min and 30 min after CytD removal (Figure 23B). This suggests that PsVs establish contact to CD151 assemblies early in the infection cascade.

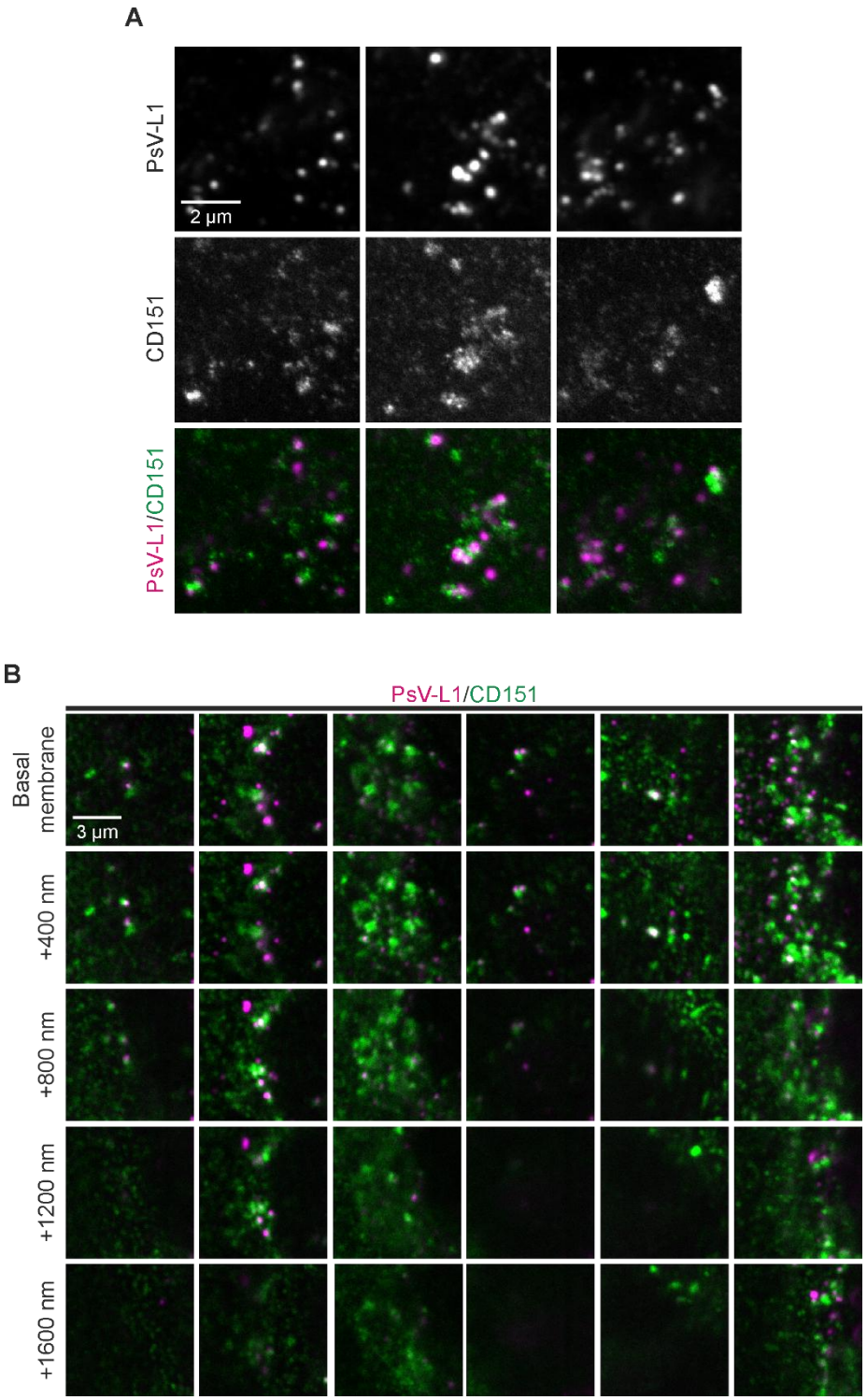

Figure 26. Examples of agglomerated CD151 maxima that are associated with PsVs and presumably are endocytic structures.
(A) More examples from the 180 min/CytD condition of agglomerated CD151 maxima (see green patches) that were associated with PsVs (magenta) and likely are endocytic structures. (B) The same experiment as in (A), but cells were scanned with 400 nm steps in the axial direction at confocal resolution, starting at the basal membrane. The structures noticed in the basal membrane as agglomerated CD151 maxima continue deeper into the cell. In some cases, more than a micrometer (see second example from the left). Figure and legend taken and modified from reference (Massenberg et al., 2025).

4.3.5 Association of PsVs and HS after CytD wash off

It has been previously shown that CytD arrested the transport of PsVs to the cell. After CytD removal, PsVs proceeded onto their infection pathway and after 180 min/CytD endocytic structures were formed consisting of CD151/PsV agglomerations. Next, the association of PsVs and HS was analyzed including a reference staining for the cell body. To this end, HaCaT cells were treated with PsVs and 10 µg/ml CytD for 5 h. As a control, cells were treated with PsVs with the corresponding amount of DMSO. After the 5 h incubation, the medium including CytD/DMSO and PsVs was removed, cells were washed and incubated for another 0 min, 30 min, 60 min and 180 min. Then, cells were fixed and antibody stained for HS (cyan) and Itgα6 (green, cell body marker). Additionally, PsVs were stained by click-chemistry (magenta). PsVs were recorded in the confocal and HS and Itgα6 in the STED mode of the microscope. All three stainings were simultaneously recorded. The Itgα6 staining resulted in a densely spotted pattern (Figure 27A), and the intensity did not change (Figure 28A). The HS staining was variable but mostly located adjacent to the cell. The overlap of HS with both, PsVs and Itgα6 was variable as well (Figure 27A). Moreover, CytD treatment increased the HS intensity. For analysis, rectangular ROIs were placed onto the images that covered mainly the cell body but included parts of the cell periphery as well. At the 0 min time point the intensity in CytD treated cells was two-fold higher compared to the control (Figure 27B). To analyze the PsV association with HS, the PCC between HS and PsVs was calculated. After CytD treatment at 0 min the PCC was 0.18 and decreased over time until it reached the level of the control with a PCC close to zero (Figure 27C). Additionally, the PCC was calculated on horizontally and vertically flipped (randomized) images (Figure 28D). For both the control and CytD treated cells, the PCC of flipped images was close to zero (Figure 28E and F). After CytD treatment at the time points 0 min, 30 min and 60 min was the PCC significantly higher compared to the flipped images (Figure 28F). When analyzing the PCC between HS and PsVs specifically in the cell body region (excluding the cell periphery), a PCC close to zero was found for the control. After treatment with CytD, a trend toward a higher PCC between 0 min and 30 min was observed, followed by a decrease until the control level was reached (Figure 27D). Additionally, the PCC was calculated on horizontally and vertically flipped (randomized) images. For both the control and CytD treated cells, the PCC of flipped images was close to zero (Figure 28G and H).

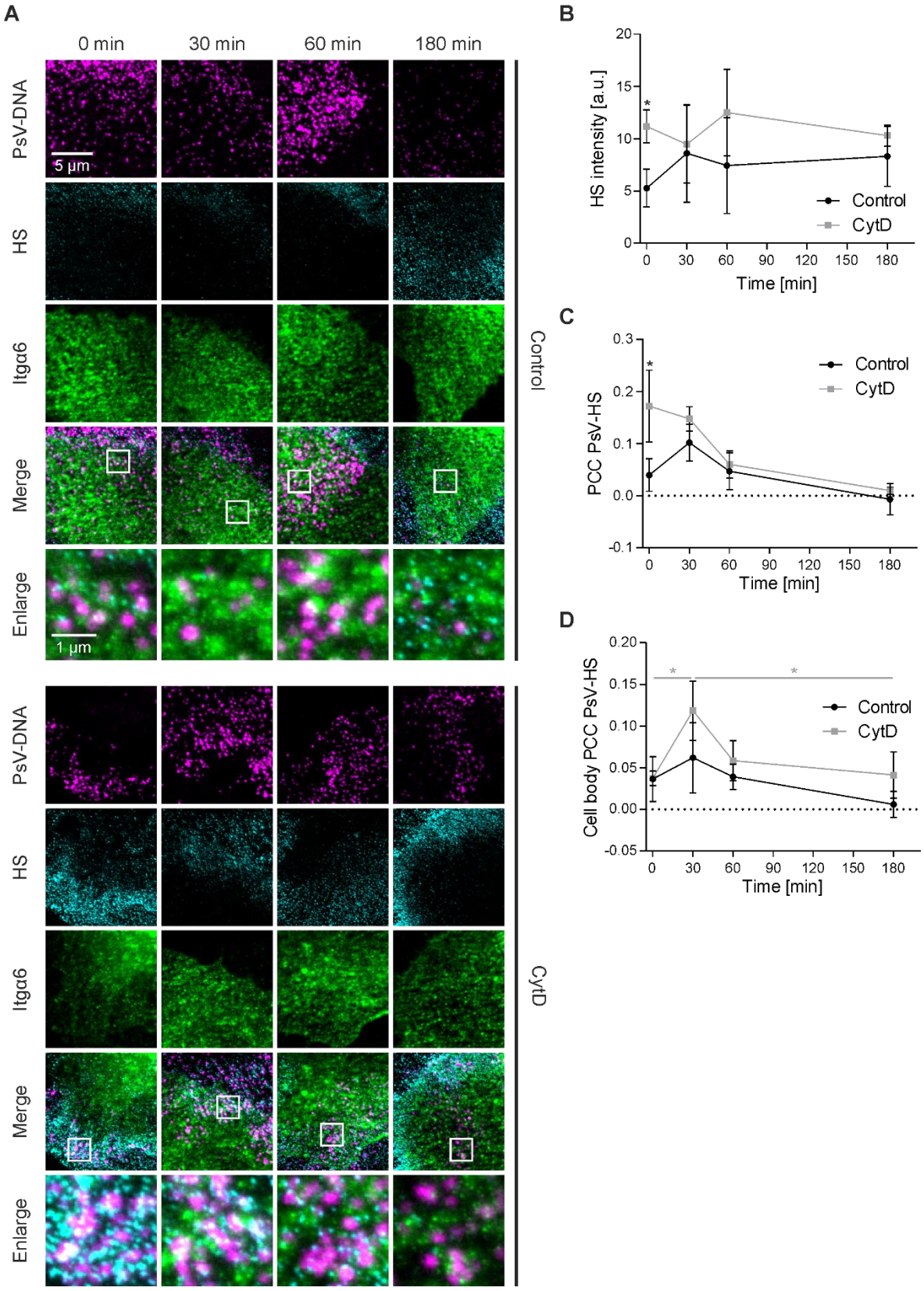

Figure 27. Association between PsVs and HS upon CytD treatment.
(A) HaCaT cells were incubated with PsVs at 37 °C for 5 h, in the absence (control, upper panels) or presence of 10 µg/ml CytD (CytD, lower panels). Afterwards, cells were washed and incubated without PsVs/CytD further for up to 180 min, before they were fixed and stained. PsVs (magenta) were

visualized by click-chemistry (6-FAM Azid) and indirect immunolabeling was used for HS (cyan; AlexaFluor™ 594) and for Itgα6 (green; STAR RED). Shown in the bottom rows are enlarged views of the white boxes in the merged images. PsVs (DNA staining) were imaged in the confocal and HS and Itgα6 in the STED mode of a STED microscope, respectively. For analysis, rectangular ROIs were placed onto the images that covered mainly the cell body but included parts of the cell periphery as well (B) Average HS intensity over time. (C) PCC between PsVs and HS over time. (D) PCC between PsVs and HS in the region of the cell body over time. Values are given as means ± SD (n = 3). Statistical difference between the same time points of control and CytD was analyzed by using the two-tailed, unpaired student's t test and in (D) the difference between CytD/30 min and CytD/0 min or CytD/180 min. Figure and legend taken and modified from reference (Massenberg et al., 2025).

Next, the shortest distance between each PsV maximum and its nearest HS maximum was calculated. In control cells the shortest distance was about 200 nm. At 0 min/CytD the shortest distance was about 130 nm and significantly lower compared to the control. At 180 min/CytD the shortest distance of the control was reached (Figure 28B). The distance between HS and Itgα6 maxima was calculated as well. In control cells the distance was close to 200 nm. When analyzing the shortest distance in CytD treated cells, at 0 min/CytD the shortest distance was about 260 nm and lowered over time until a distance of 180 nm was reached at 180 min/CytD, which was significantly lower compared to the control (Figure 28C).

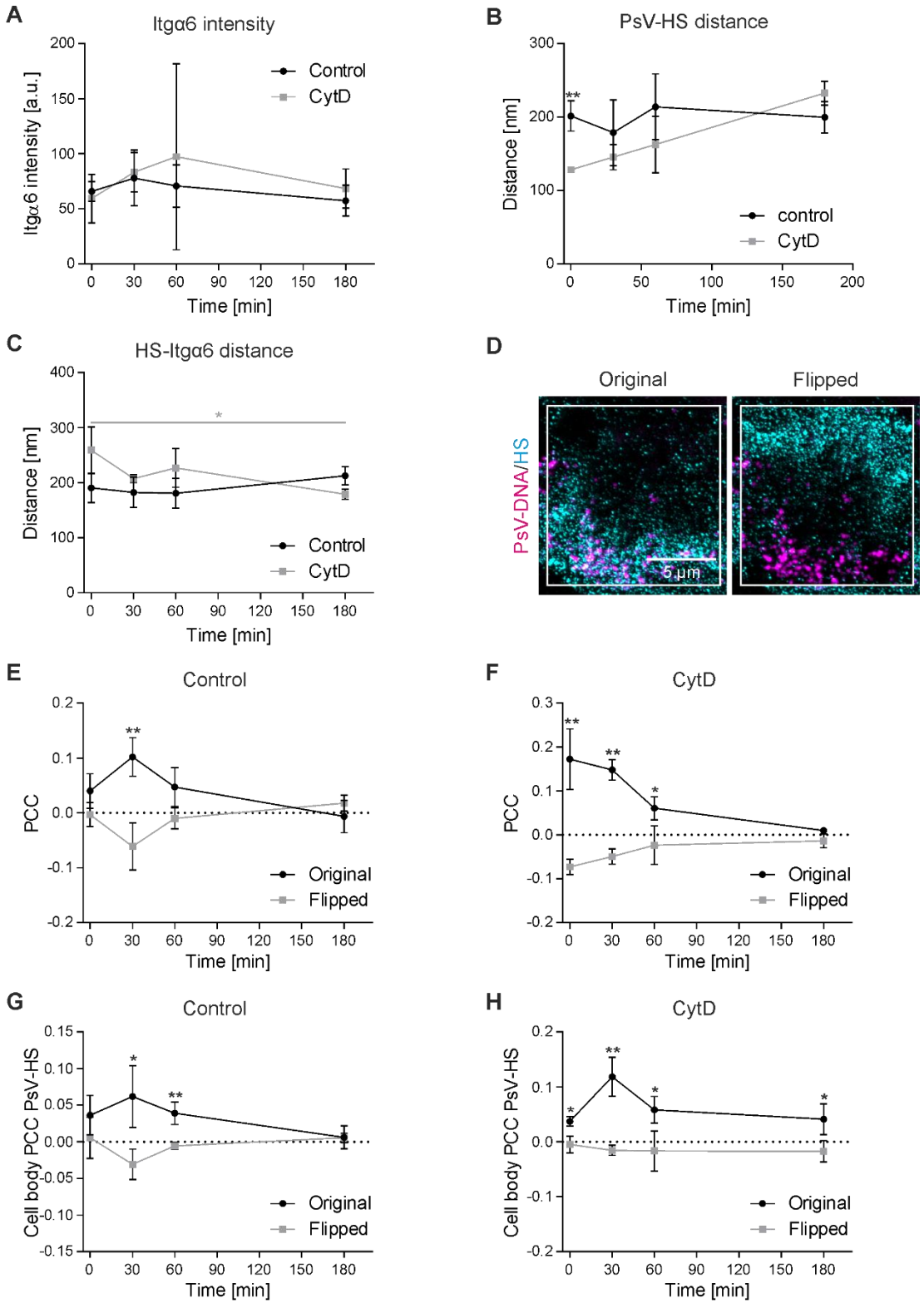

Figure 28. Analysis of the association between PsVs and HS.
(A) Average Itgα6 intensity over time. (B) Average shortest distance between a PsV maximum and its next nearest HS maximum over time. (C) Average shortest distance between a HS maximum and its next nearest Itgα6 maximum over time. (D) Example of flipped HS image. Left, original image taken from the 0 min/CytD condition. The ROI selected for analysis is shown as white box. Right, the cyan image within the ROI is flipped horizontally and vertically. (E) The PCC between PsVs and HS of the

control condition is shown again, together with the respective PCCs determined on flipped images. (F) The PCC between PsVs and HS of the CytD condition is shown again, together with the respective PCCs determined on flipped images. (G) The cell body PCC between PsVs and HS of the control condition is shown again, together with the respective PCCs determined on flipped images. (H) The cell body PCC between PsVs and HS of the CytD condition is shown again, together with the respective PCCs determined on flipped images. Values are given as means ± SD (n = 3). Statistical difference between the same time points of original and flipped images or control and CytD was analyzed by using the two-tailed, unpaired student's t test. Figure and legend taken and modified from reference (Massenberg et al., 2025).

The fraction of closely associated PsVs with HS was calculated. As criterion for close association, a distance of 80 nm between PsV and HS maxima was defined, as this value was close to the resolution limit of the used microscope. The same analysis was performed on horizontally and vertically flipped (randomized) images, to identify random background association. In control cells the fraction was about 20% and higher compared to the flipped images with about 15% (Figure 29A). At 0 min/CytD the fraction of closely associated PsVs with HS was about 30% and lowered over time until the level of the control cells was reached after 180 min. In the corresponding flipped images, about 10% of PsVs were closely associated. At 0 min/CytD and 30 min/CytD the fraction of closely associated PsVs with HS was significantly higher compared to the flipped images (Figure 29B). To correct for a random background association, the fraction of closely associated PsVs of all replicates from the flipped images was plotted against the HS maxima density. A linear regression line was fitted onto the data and described how the background association depended on the HS maxima density. Based on the regression line, the random background association was calculated, for any HS maxima density in an original image (Figure 29C). The fraction of closely associated PsVs with HS was corrected for random background association. In control cells the corrected fraction was about 5% and significantly higher compared to the flipped images with no remaining association (Figure 29D). At 0 min/CytD the fraction of closely associated PsVs with HS was about 15% and lowered over time until a level of 5% was reached after 180 min. The fraction of closely associated PsVs was significantly higher compared to the flipped images with no remaining association (Figure 29E). Comparing the corrected fraction of control and CytD treated cells, at 0 min a significant increase in the fraction of associated PsVs with HS was observed (Figure 29F). For better visualization of the criterion for close association, examples of the distance between a PsV and its nearest HS maximum are shown in Figure 29G, with one example not fulfilling the distance criterion of a distance <= 80 nm and one fulfilling the criterion.

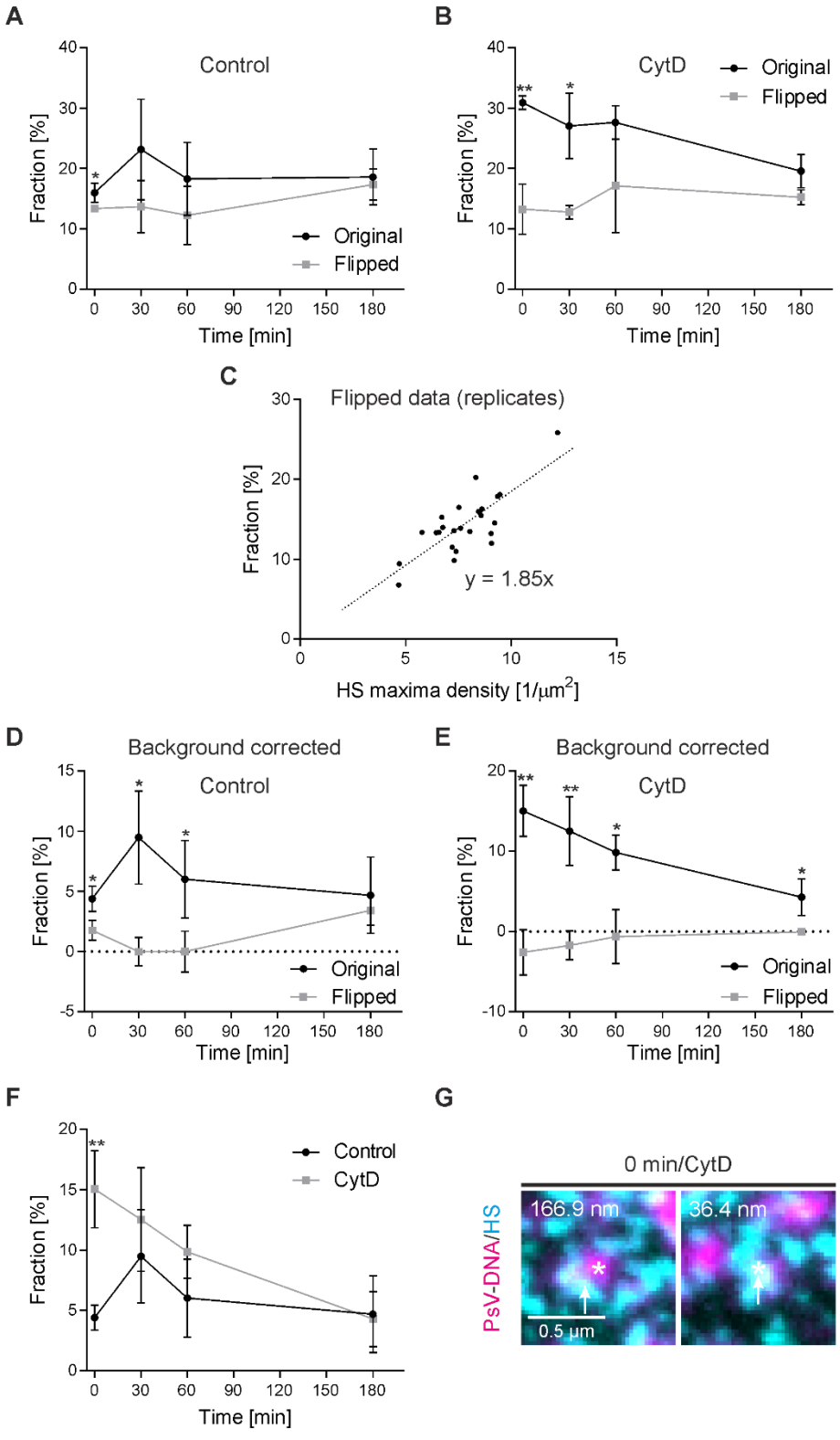

Figure 29. Background correction of the fraction of PsVs closely associated with HS.
(A) The fraction of closely associated PsVs (PsV maxima with a distance ≤ 80 nm to the next nearest HS maximum) in the control, analyzed on original and flipped images. (B) Same as (A) for the CytD condition. (C) From the altogether 24 replicates of the flipped images, the fraction of closely associated PsVs is plotted against the HS maxima density, and a linear regression line is fitted to the data points. (D) For each replicate from the original and the flipped images in (A), the background fraction is

calculated using the equation of the regression line in (C) and the respective HS maxima density and subtracted from the fraction of closely associated PsVs. (E) Same as (D) for the CytD condition. (E) The background corrected original values of the control and CytD condition. (G) Two examples of PsVs (each marked by an asterisk) taken from the 0 min/CytD condition. Number in the upper left indicates the shortest distance in nm between the PsV maximum and the next nearest HS maximum (marked by an arrow). Values are given as means ± SD (n = 3). Statistical difference between the same time points of original and flipped images was analyzed using the two-tailed, unpaired student's t test. Figure and legend taken and modified from reference (Massenberg et al., 2025).

Next, the distance of each PsV to the next nearest Itgα6 maximum was plotted against the distance to the next nearest HS maximum. Four populations were defined: PsVs with a distance to HS < 250 nm and to Itgα6 > 250 nm (green), PsVs with a distance to HS > 250 nm and to Itgα6 < 250 nm (magenta), PsVs with a distance to HS > 250 nm and to Itgα6 > 250 nm (grey) and PsVs with a distance to HS < 250 nm and to Itgα6 < 250 nm (black) (Figure 30A). In control cells, the distances remained unchanged over the entire observation time; 59 – 65% of the PsVs had a short distance (< 250 nm) to both Itgα6 and HS, and another 12 - 15% had a short distance (< 250 nm) to HS but not to Itgα6 (> 250 nm), while 15 – 23% had a short distance (< 250 nm) to Itgα6 but not to HS (Figure 30B). No difference between the distance plots over the whole observation time of 180 min were observed for the control (Figure 30C). In cells treated with CytD, a larger fraction of PsVs had a short distance (< 250 nm) to HS but not to Itgα6 at the 0 min time point compared to the control (46% compared to 12%), as PsVs accumulated at the cell periphery. Over time, the PsVs in the CytD treated cells acquired a larger distance to HS and a shorter distance to Itgα6. After 180 min, the distances were similar to the untreated control (Figure 30B). The changes were observed in the distance plots as well (Figure 30C).

Altogether, the data indicates that CytD treatment increases the PsV association with HS at 0 min, likely because PsVs remain trapped in the ECM. After CytD removal, this association diminishes. However, the transient increase in PCC specifically in the region of the cell body likely reflects the translocation of HS-coated virions to the cell body. Moreover, this association diminishes over the subsequent 150 min, suggesting that an increasing number of PsVs are no longer associated with HS and PsVs may progressively lose their HS coat over time.

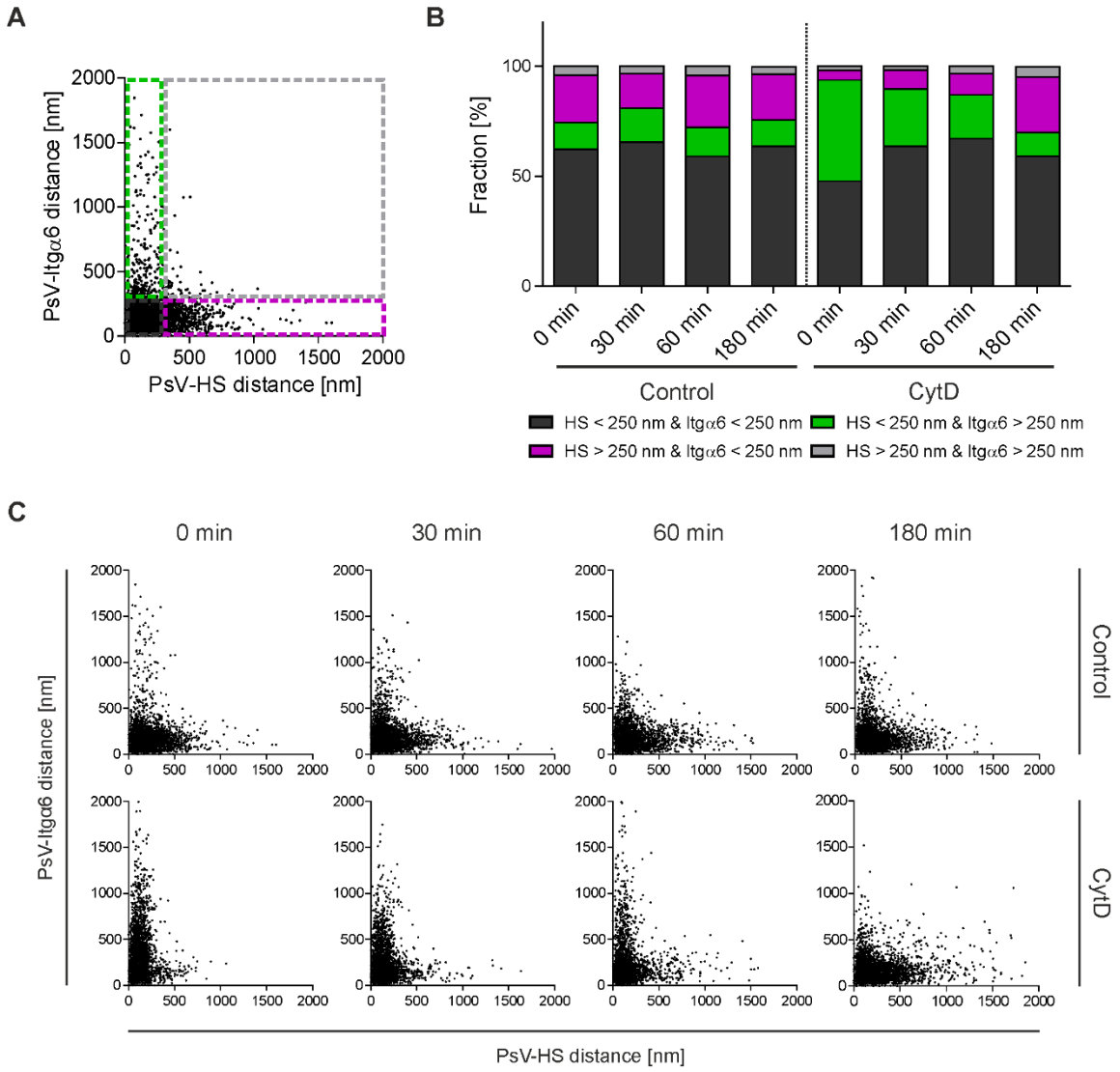

Figure 30. Pattern of PsV-Itgα6 and PsV-HS distances over time.
(A) Definition of four PsV populations. Dashed green rectangle; PsVs with a distance to HS < 250 nm and to Itgα6 > 250 nm. Dashed magenta rectangle; PsVs with a distance to HS > 250 nm and to Itgα6 < 250 nm. Dashed gray square; PsVs with a distance to HS > 250 nm and to Itgα6 > 250 nm. Dashed black square; PsVs with a distance to HS < 250 nm and to Itgα6 < 250 nm. (B) The PsV fraction size (in percent) of the four populations defined in (A) is illustrated using the same colors as in (A). Shown is the mean of the three biological replicates. (C) The same data as in (B), plotting for each PsV the shortest distance to Itgα6 against the shortest distance to HS (pooling the three biological replicates; 3,043 – 4,080 PsVs per plot). Statistical difference between the same time points of control and CytD is shown in table 10. Figure and legend taken and modified from reference (Massenberg et al., 2025).

Table 10. Fraction of PsVs in percent of each of the four distance categories.
Values are means ± SD of the data shown in Figure 30B. For each time point and category, p-values between control and CytD were calculated by using the two-tailed, unpaired student's *t*-test (n = 3). P-values < 0.05 are illustrated in bold. Taken and modified from reference (Massenberg et al., 2025).

Fraction of PsVs [%]	0 min			30 min			60 min			180 min		
	control	CytD	p-value	control	CytD	p-value	control	CytD	p-value	control	CytD	p-value
HS < 250 nm & ltga6 < 250 nm	62.31 ± 5.05	47.83 ±3.26	**0.0271**	65.48 ± 8.35	63.67 ± 1.14	0.7764	59.06 ± 10.64	67.16 ± 9.84	0.4739	63.69 ± 4.27	59.28 ± 3.17	0.3065
HS < 250 nm & ltga6 > 250 nm	12.18 ± 5.51	46.04 ± 3.67	**0.0019**	15.46 ± 3.14	26.12 ± 2.16	**0.0167**	13.25 ± 1.94	19.87 ± 3.12	0.0637	11.97 ± 1.53	10.64 ± 1.15	0.3808
HS > 250 nm & ltga6 < 250 nm	21.59 ± 4.07	4.34 ± 0.37	**0.0040**	15.83 ± 5.73	8.58 ± 2.33	0.1723	23.49 ± 6.55	9.60 ± 4.81	0.0731	20.88 ± 3.31	25.24 ± 1.96	0.1842
HS > 250 nm & ltga6 > 250 nm	3.93 ± 0.30	1.79 ± 0.60	**0.0110**	3.23 ± 0.88	1.63 ± 0.21	0.0675	4.19 ± 2.43	3.38 ± 2.20	0.7425	3.46 ± 0.54	4.84 ± 2.87	0.5393

4.3.6 Association of PsVs and HS after (-)-blebbistatin wash off

As mentioned above, it is assumed that virions migrate by an actin-dependent transport along cell protrusions toward the cell body (Smith et al., 2008, Swift et al., 2012). So far only the effect of the actin inhibitor CytD on PsV migration was tested. Next, the myosin II inhibitor (-)-blebbistatin was evaluated. Blebbistatin is known to lower the affinity of myosin II to actin and thereby inhibits actin retrograde flow (Kovács et al., 2004, Lin et al., 1996, Swift et al., 2012).

The association of PsVs and HS was analyzed upon blebbistatin treatment including a reference staining for the cell body. To this end, HaCaT cells were treated with PsVs and 30 µM blebbistatin for 5 h. As a control, cells were treated with PsVs with the corresponding amount of DMSO. After the 5 h incubation, the medium including blebbistatin/DMSO and PsVs was removed, cells were washed and incubated for another 0 min, 30 min, 60 min and 180 min. Then, cells were fixed and antibody stained for L1 (magenta) and HS (cyan), Additionally, F-Actin was stained with phalloidin iFluor647 (green). In control cells the PsVs appeared in a spotty pattern scattered across the cell. In blebbistatin treated

cells, a PsV accumulation was visible at the cell periphery, but it appeared as if the PsVs already started to translocate onto the cell body and stopped midst way (Figure 31A). The HS staining was variable but mostly located adjacent to the cell (Figure 31A). For analysis, rectangular ROIs were placed onto the images that covered mainly the cell body but included parts of the cell periphery as well. The HS intensity was calculated and blebbistatin treatment slightly increased the HS intensity at 0 min (Figure 31B). Additionally, the PCC between HS and PsVs was calculated to analyze the PsV association with HS. After blebbistatin treatment at 0 min the PCC was 0.09 and decreased over time until it reached the level of the control with a PCC close to 0.04 (Figure 31C). Additionally, the PCC was calculated on horizontally and vertically flipped (randomized) images. For both the control and blebbistatin treated cells, the PCC of flipped images was close to zero (Figure 32A and B). In control cells the PCC was significantly higher after 30 min and 60 min compared to the flipped images (Figure 32B) and after blebbistatin treatment the PCC was significantly higher compared to the flipped images for all time points (Figure 32B). When analyzing the PCC between HS and PsVs specifically in the cell body region (excluding the cell periphery), a PCC close to 0.04 was found for the control. In contrast to a treatment with CytD, after blebbistatin treatment the cell body PCC between PsVs and HS was elevated already after 0 min and decreased over time until the control level was reached (Figure 31D). As a control, the cell body PCC was calculated on horizontally and vertically flipped (randomized) images. For both, the control and blebbistatin treated cells, the PCC of flipped images was close to zero (Figure 32C and D). The cell body was significantly higher compared to the flipped images for all samples except the control/0 min (Figure 32C and D).

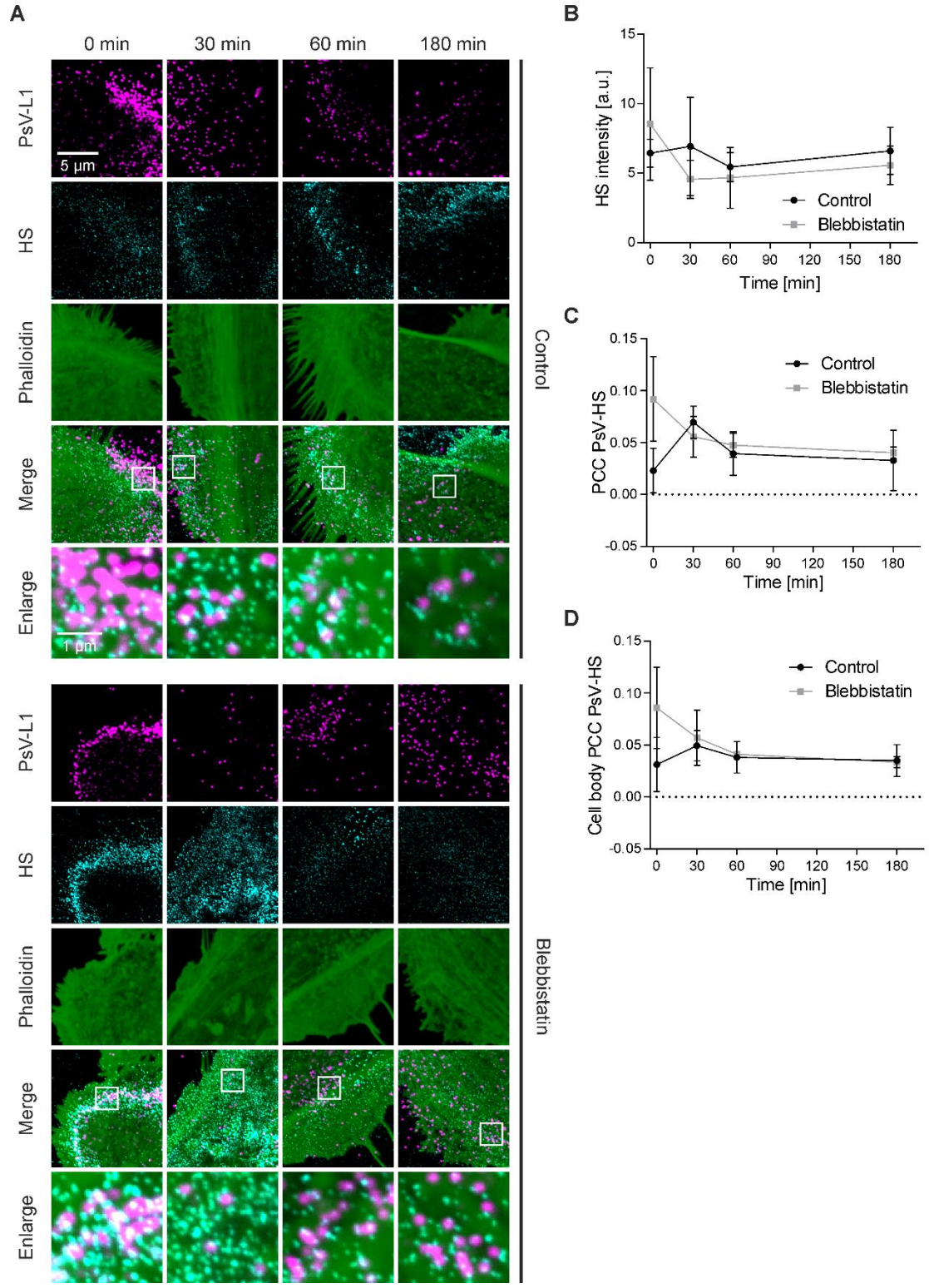

Figure 31. Association between PsVs and HS upon blebbistatin treatment.
(A) HaCaT cells were incubated with PsVs at 37 °C for 5 h, in the absence (control, upper panels) or presence of 30 µM blebbistatin (Blebbistatin, lower panels). Afterwards, cells were washed and incubated without PsVs/blebbistatin further for up to 180 min, before they were fixed and stained. Immunofluorescence was used for L1 (magenta; STAR GREEN) and for HS (cyan; AlexaFluor 594) staining. F-actin was stained by fluorescent labelled phalloidin (green; iFluor647). Shown in the bottom rows are enlarged views of the white boxes in the merged images. PsVs (L1 staining) and F-actin were

imaged in the confocal and HS in the STED mode of a STED microscope, respectively. For analysis, rectangular ROIs were placed onto the images that covered mainly the cell body but included parts of the cell periphery as well. (B) Average HS intensity over time. (C) PCC between PsV-L1 and HS over time. (D) PCC between PsV-L1 and HS in the region of the cell body over time. Values are given as means ± SD (n = 3). Statistical difference between the same time points of control and blebbistatin was analyzed by using the two-tailed, unpaired student's t test. Figure and legend taken and modified from reference (Massenberg et al., 2025).

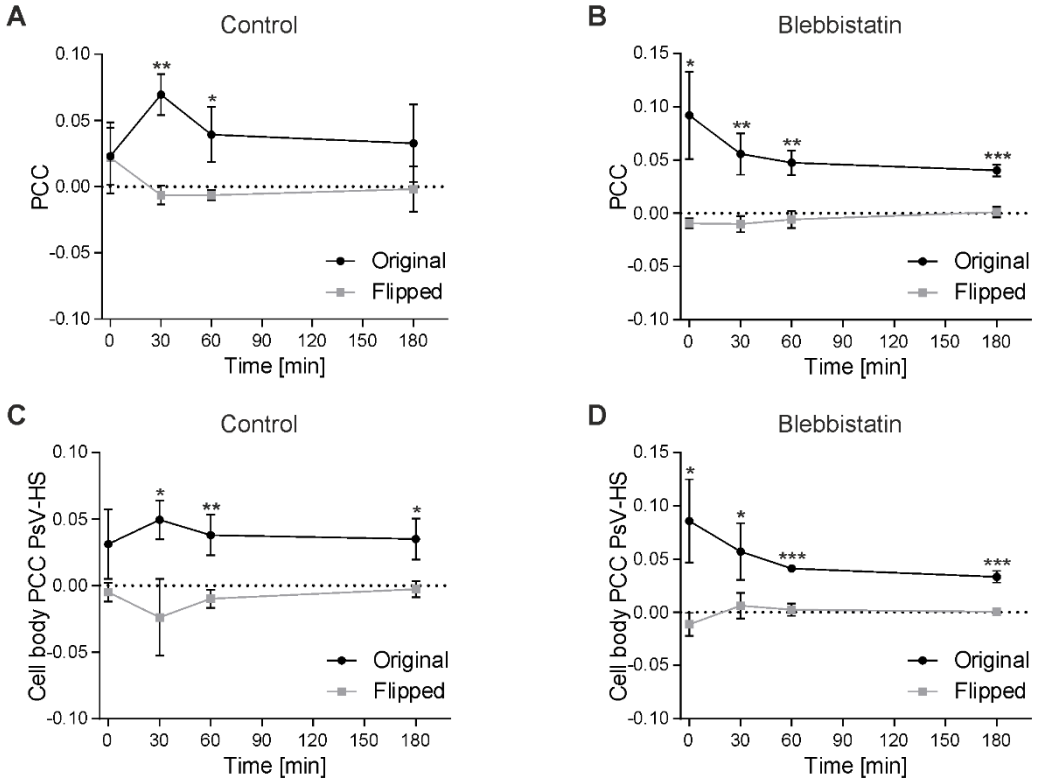

Figure 32. PCC between PsVs and HS after blebbistatin treatment.
(A) The PCC between PsV-L1 and HS of the control condition is shown again, together with the respective PCCs determined on flipped images. (B) The PCC between PsV-L1 and HS of the blebbistatin condition is shown again, together with the respective PCCs determined on flipped images. (C) The cell body PCC between PsV-L1 and HS of the control condition is shown again, together with the respective PCCs determined on flipped images. (D) The cell body PCC between PsV-L1 and HS of the blebbistatin condition is shown again, together with the respective PCCs determined on flipped images. Values are given as means ± SD (n = 3). Statistical difference between the same time points of original and flipped images is analyzed using the two-tailed, unpaired student's t test. Figure and legend taken and modified from reference (Massenberg et al., 2025).

The fraction of closely associated PsVs with HS after blebbistatin treatment was calculated. As criterion for close association, a distance of 80 nm between PsV and HS maxima was defined, as this value was close to the resolution limit of the used microscope. As a control, the same analysis was performed on horizontally and vertically flipped (randomized) images, to identify random background association. In control cells the fraction was about 15% and higher compared to the flipped images with about 10% (Figure 33A). At 0 min/blebbistatin the fraction of closely associated PsVs with HS was

about 17% and lowered to 15%, the level of control cells after 30 min. In the corresponding flipped images, about 10% of PsVs were closely associated with HS. Because of the high variability of the samples only at 30 min/blebbistatin the fraction of closely associated PsVs with HS was significantly higher compared to the flipped images (Figure 33B). To correct for a random background association, the fraction of closely associated PsVs of all replicates from the flipped images was plotted against the HS maxima density. A linear regression line was fitted onto the data and described how the background association depended on the maxima density. Based on the regression line, the random background association was calculated, for any maxima density in an original image (Figure 33C). The fraction of closely associated PsVs with HS was corrected for random background association. In control cells the corrected fraction was about 5% and significantly higher compared to the flipped images with no remaining association (Figure 33D). At 0 min/blebbistatin the fraction of closely associated PsVs with HS was about 8% and lowered to 5% after 30 min. The fraction of closely associated PsVs was significantly higher compared to the flipped images with no remaining association (Figure 33E). Comparing the corrected fraction of control and blebbistatin treated cells, at 0 min an increase in the fraction of associated PsVs with HS was observed after blebbistatin treatment (Figure 33F). For better visualization of the criterion for close association, examples of the distance between a PsV and its nearest HS maximum are shown in Figure 33G, with one example not fulfilling the distance criterion of a distance <= 80 nm and one fulfilling the criterion.

Taken together, blebbistatin treatment did not trap PsVs in the ECM as ongoing actin polymerization pushes actin filaments along with PsVs toward the cell body. However, a subsequent blocking of transport was observed at later time points after blebbistatin treatment. This suggests that myosin II contributes to sustained transport.

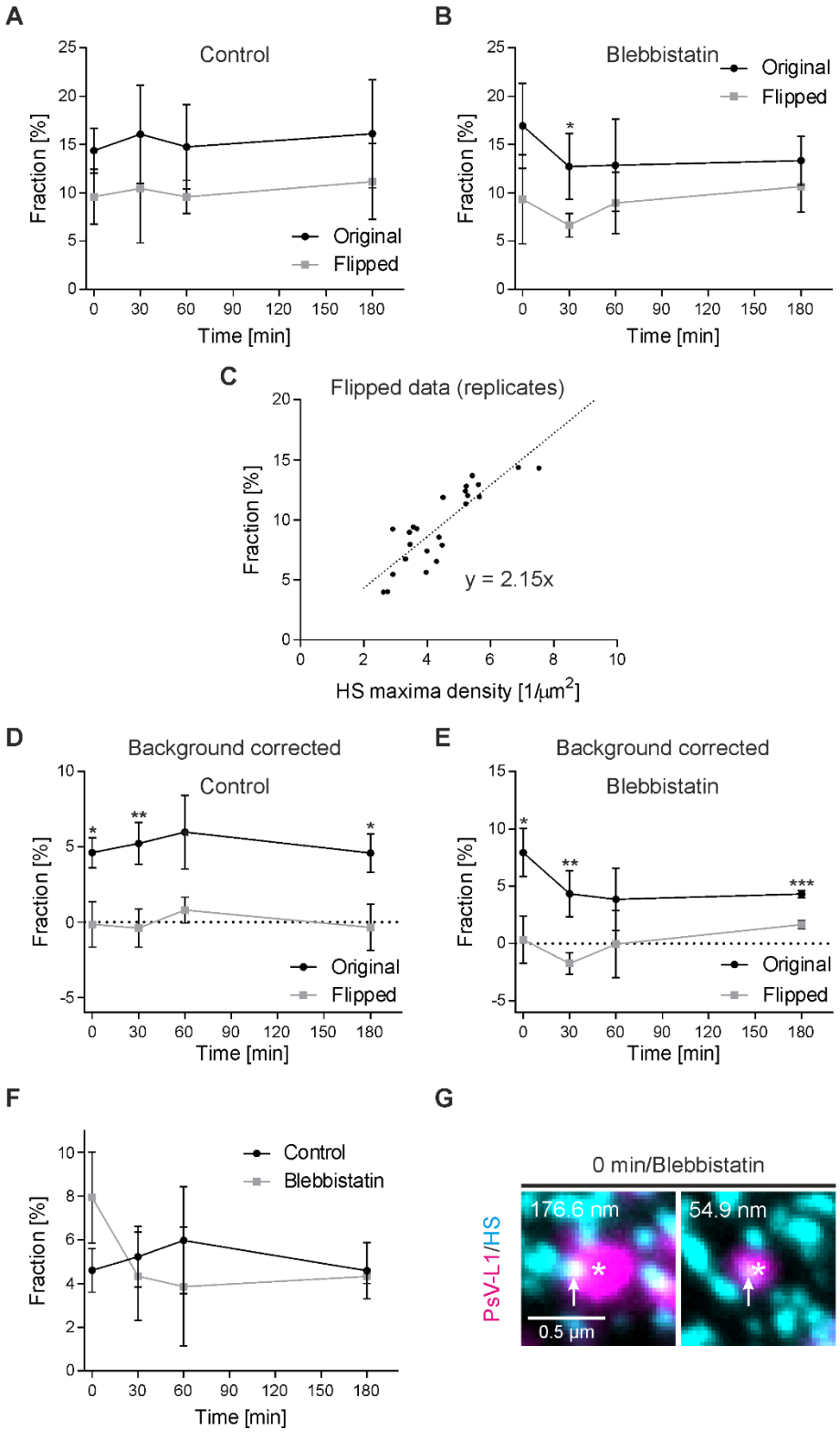

Figure 33. Background correction of the fraction of PsVs closely associated with HS after blebbistatin treatment.

(A) The fraction of closely associated PsVs (PsV maxima with a distance ≤ 80 nm to the next nearest HS maximum) in the control, analyzed on original and flipped images. (B) Same as (A) for the blebbistatin condition. (C) From the altogether 24 replicates of the flipped images, the fraction of closely associated PsVs is plotted against the HS maxima density, and a linear regression line is fitted

to the data points. (D) For each replicate from the original and the flipped images in (A), the background fraction is calculated using the equation of the regression line in (C) and the respective HS maxima density and subtracted from the fraction of closely associated PsVs. (E) Same as (D) for the blebbistatin condition. (E) The background corrected original values of the control and blebbistatin condition. (G) Two examples of PsVs (each marked by an asterisk) taken from the 0 min/blebbistatin condition. Number in the upper left indicates the shortest distance in nm between the PsV maximum and the next nearest HS maximum (marked by an arrow). Values are given as means ± SD (n = 3). Statistical difference between the same time points of original and flipped images was analyzed using the two-tailed, unpaired student's t test. Figure and legend taken and modified from reference (Massenberg et al., 2025).

4.4 Inhibition of PsV infection with therapeutic strategies

So far, the data showed that PsVs primary associate with HS in the ECM, followed by a fast transfer of HS-coated virions from the ECM to CD151. Therapeutic strategies that inhibit single or multiple of these entry steps may be a promising tool to prevent HPV infection.

4.4.1 Effect of the peptide 19-2.5 on the PsV/CD151 association

Several therapeutic strategies are known today to prevent viral infections such as antiviral peptides. One promising candidate is the HSPG-binding peptide 19-2.5 as it was able to inhibit the cell entry of various enveloped viruses so far. However, peptide 19-2.5 was not tested on non-enveloped viruses like HPV16. First experiments with peptide 19-2.5 and HPV16 PsVs, showed a reduced infection and binding efficiency of PsVs when cells were treated with peptide 19-2.5 before PsV incubation (Mikuličić et al., 2025). In the next step, a post-binding experiment should reveal if the PsV association with CD151 during the viral cell entry is affected by peptide 19-2.5. Therefore, HeLa cells were incubated for a total of 4 h with PsVs. After 1 h, 1 µg/ml peptide 19-2.5 or control peptide was added. One sample without peptide addition was taken as well (- peptide). Additionally, one sample was taken 1 h after PsV addition, directly before the peptide addition (direct fix). Samples were fixed and antibody-stained for L1 and CD151. The L1 staining was recorded in the confocal and the CD151 staining in the STED mode of the microscope, respectively. The CD151 staining appeared in a spotty pattern with CD151 concentrated in spots scattered across the whole cell. The PsV staining was variable and PsV spots were scattered across the cell (Figure 34).

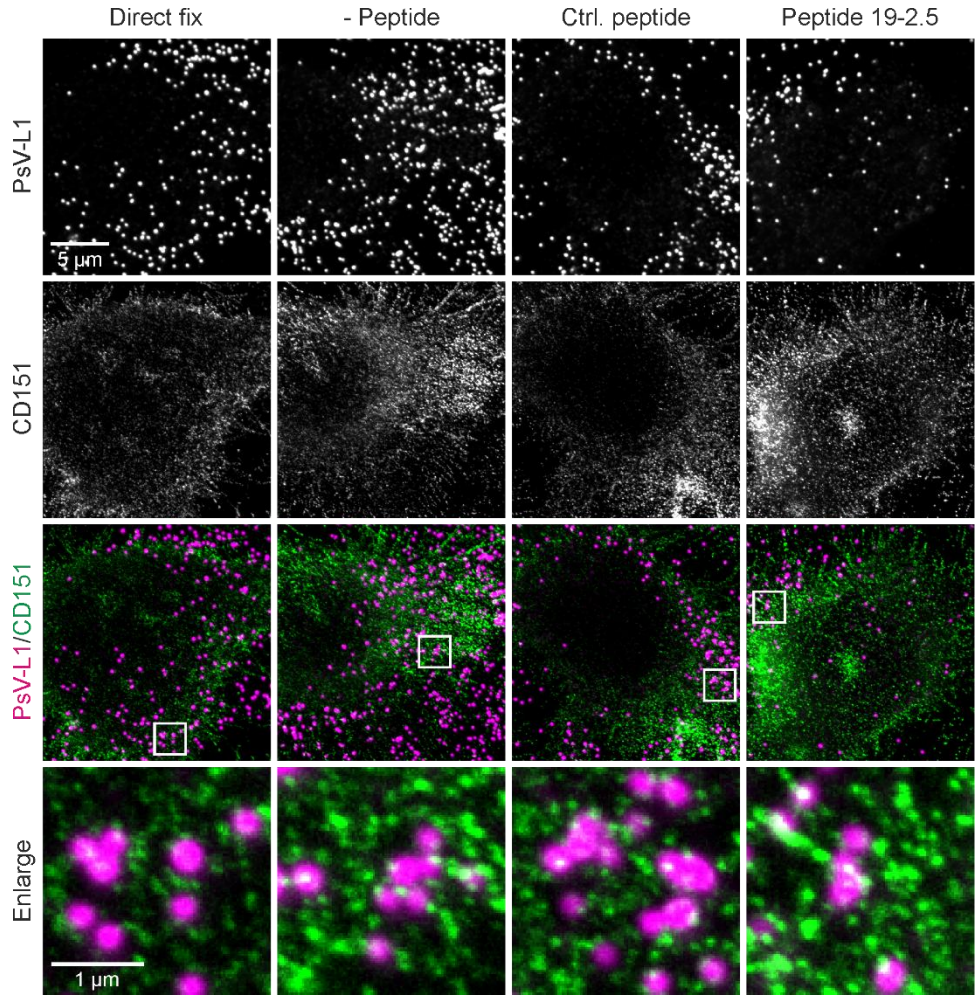

Figure 34. Effect of peptide 19-2.5 on post PsV binding in HeLa cells.
HeLa cells were incubated for a total of 4 hours with PsVs. After 1 hour, they were additionally incubated either without any peptide (−Peptide), with 1 µg/mL of the control peptide (Ctrl. peptide) and peptide 19-2.5 (Peptide 19-2.5) or directly fixed (Direct fix). Then, cells were fixed and surface-stained for L1 (magenta) and CD151 (green). X,Y-scans of L1 in the confocal and CD151 in the STED channel were recorded at the basal membrane. White boxes mark enlarged views of the overlays shown at the bottom. Figure and legend taken and modified from reference (Mikuličić et al., 2025).

For analysis, rectangular ROIs were placed onto the images that covered mainly the cell body. Analyzing the CD151 maxima, no change between the groups was observed regarding the maxima intensity (Figure 35A), maxima density (Figure 35B) and maxima size (Figure 35C). The CD151 maxima intensity was about 20 a.u. in HeLa cells (Figure 35A) and about 4 CD151 maxima/µm^2 were found (Figure 35B). The CD151 maxima were about 150 nm large in size (Figure 35C). To analyze the association of PsVs with CD151, the PCC between PsVs and CD151 was calculated. As a control, the PCC was analyzed on horizontally and vertically flipped images as well. Again, no difference between the four conditions was observed. However, the PCC of all four conditions was significantly higher compared to the flipped control (Figure 35D).

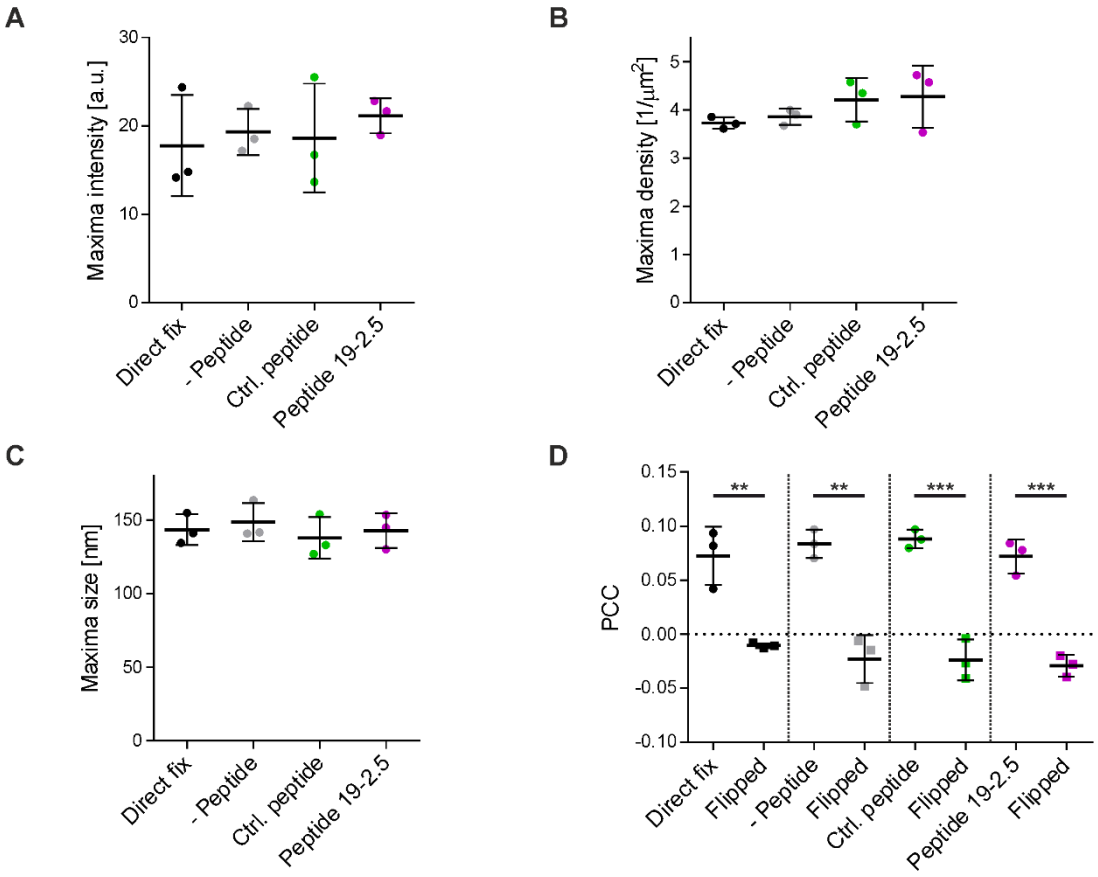

Figure 35. Analysis of the PsV association with CD151 upon peptide 19-2.5 treatment.
Analysis of the CD151 maxima intensity (A), CD151 maxima density (B) and CD151 maxima size (C). (D) PCC analyzed in the ROI between the PsVs and CD151 original and flipped (randomized) images. Values are given as means ± SD (n = 3). Statistical differences between the groups were analyzed using unpaired student's t-test. Figure and legend taken and modified from reference (Mikuličić et al., 2025).

Additionally, the number of the PsV neighbored maxima were counted in a circular 925 nm diameter ROI, placed onto PsV positions. As a control, the same analysis was performed on horizontally and vertically flipped images. The number of CD151 maxima counted in the PsV neighborhood was normalized to the average CD151 maxima density of the corresponding image. At PsV locations with a CD151 maxima density equal to the average CD151 maxima density, an average value of 1 was calculated. If CD151 is enriched at PsV binding sites, a value larger than 1 was calculated. In the original images a right-shifted distribution was obtained, whereas a normal distribution peaking at 1 was obtained from flipped images (Figure 36). However, no difference between the four conditions was observed. The right-shifted distribution in the original images was caused by two populations of PsVs: one with an elevated number of neighbored CD151 maxima and one with a random number (as in the flipped images). To further analyze the two populations of accumulated (dashed lines) and randomized (dotted lines) CD151 maxima, a decomposition of the measured data into two Gaussian

distributions was calculated, yielding the fraction of PsVs with an elevated number of neighbored CD151 maxima (Figure 36).

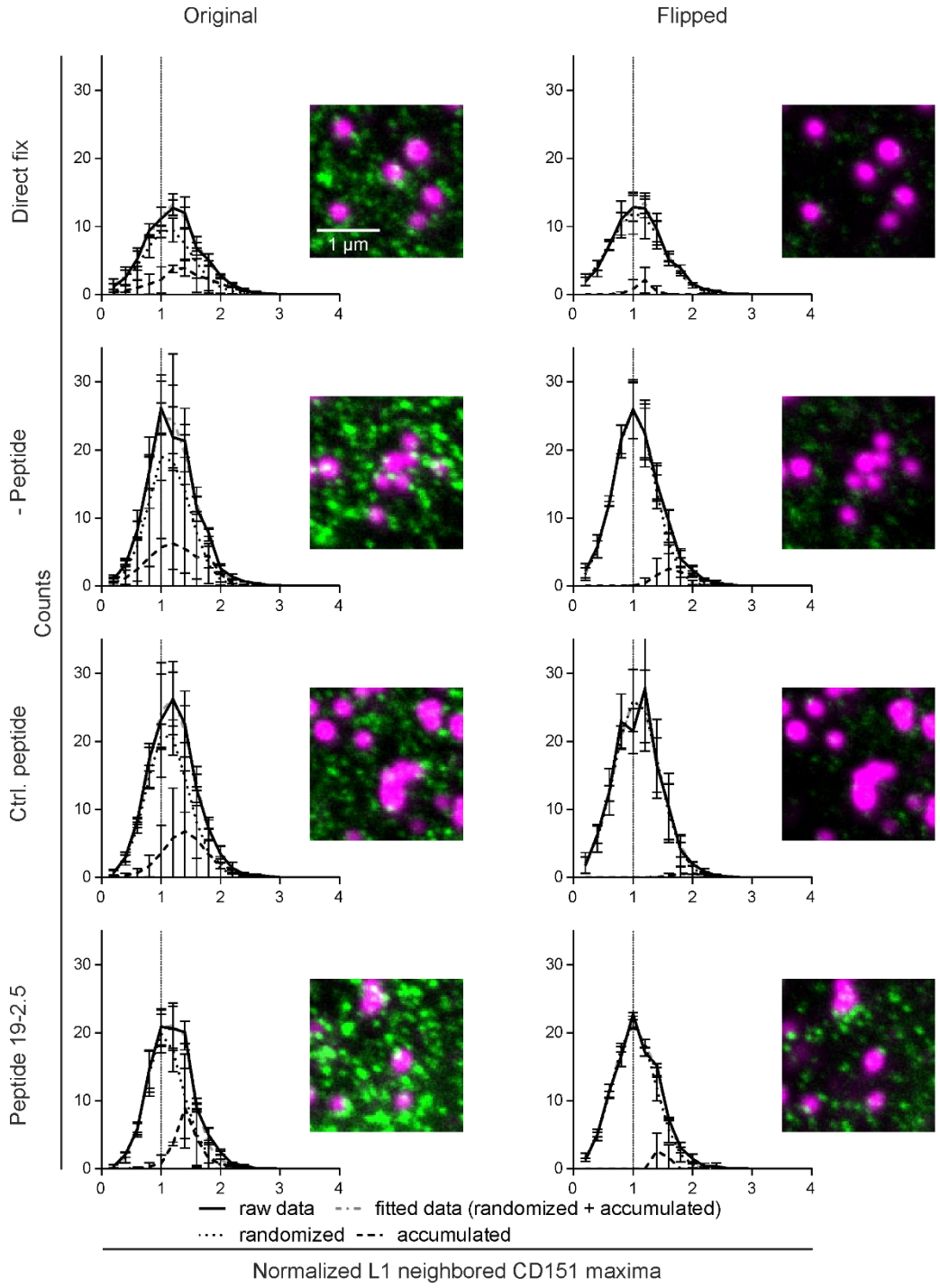

Figure 36. CD151 crowding at PsV-binding sites.
Analysis of the relative normalized PsV neighbored CD151 maxima. At every PsV position, a circular 925 nm ROI was positioned, the CD151 maxima were counted, and the value was normalized to the CD151 average maxima density. The number of PsVs (defined by the L1 signal) is plotted in absolute counts versus the normalized CD151 maxima counts (left panel). At a randomized relationship between L1 and CD151 (horizontally and vertically flipped images; right panel), the analysis yields a Gaussian-like distribution peaking at the value of 1. If CD151 maxima at PsV locations were more

abundant than random, the distribution becomes right shifted, as it contains two Gaussian distributions. For determining the fraction of PsVs located at CD151 crowds, the distribution was decomposed into 2 Gaussian distributions (dotted lines mark random, dotted-dashed lines mark the pool of PsVs at CD151 crowds; grey dotted-dashed lines are the sum of both populations). Figure and legend taken and modified from reference (Mikuličić et al., 2025).

After decomposition of the normalized PsV neighbored CD151 maxima distribution, between 21% and 34% of PsVs had an elevated number of CD151 maxima in the original images. In flipped images only 1 – 7% of PsVs had an elevated number of CD151 maxima (Figure 37A). Additionally, the average number of neighbored CD151 maxima was significantly elevated in the original images compared to the flipped control (Figure 37B). However, no difference between the four conditions was observed.

Taken together, the peptide 19-2.5 had no effect on the association of PsVs with CD151 suggesting that the CD151 mediated PsV entry complex formation is not disturbed by peptide 19-2.5. Therefore, the peptide 19-2.5 may inhibit PsV infection at another step of viral cell entry.

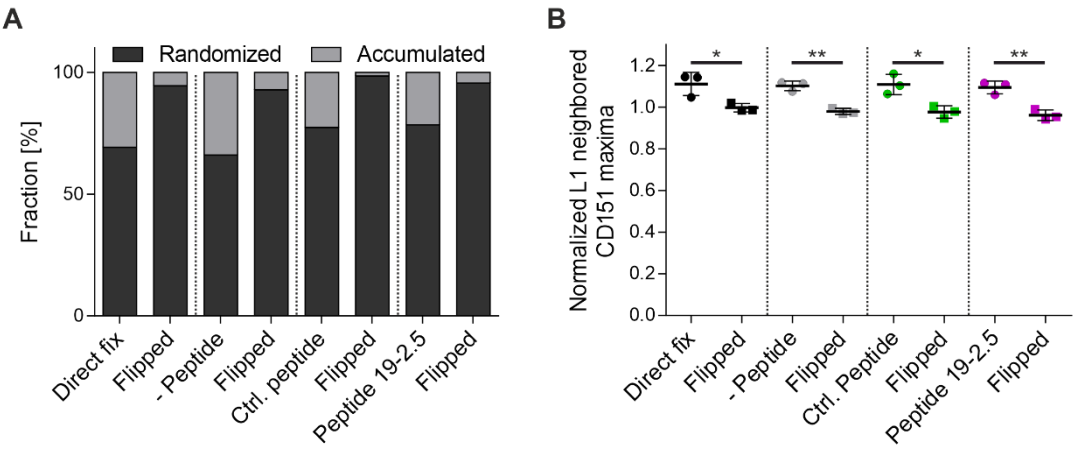

Figure 37. Analysis of CD151 crowding at PsV-binding sites.
(A) Based on the decomposition of the normalized PsV neighbored CD151 maxima into two Gaussians, the fraction of PsVs with randomized and accumulated neighbored CD151 maxima was calculated. (B) Showing the average of the normalized PSV neighbored CD151 maxima comparing original images with flipped images. Values are given as means ± SD (n = 3). Statistical differences between the groups were analyzed using unpaired student's t-test. Figure and legend taken and modified from reference (Mikuličić et al., 2025).

4.4.2 Effect of the peptide 19-2.5 on the PsV cell entry

While imaging the samples of HeLa cells treated with peptide 19-2.5 as described above, large PsV accumulations were observed sitting mostly on top of the cells. Therefore, using the samples as described above, X,Z/Y,Z-confocal micrographs of the cells were recorded to determine the PsV distribution around the cells. Only in a minority of cells, large PsV accumulations were observed. While recording it was specifically searched for cells exhibiting this phenomenon. However, essentially only after treatment with peptide 19-2.5, large distal PsV accumulations were observed (Figure 38).

To further analyze the fraction of distal PsVs, cells were outlined based on the CD151 staining (Figure 39A), and the integrated density of the PsV signal was calculated within the outline and from the total PsV signal. Afterwards, the background corrected signal within the outline was subtracted from the background corrected total signal, yielding the signal of distal PsVs. Example images of each condition with an auto-scaled intensity scaling of the PSV signal are shown in Figure 39B. Two examples were shown for the peptide 19-2.5 condition: one cell resembling cells from the control condition and one cell with very large PsV accumulations, which were typically localized at the top of the cell. Upon treatment with peptide 19-2.5, an almost three-fold increase of the distal PsV fraction was observed (Figure 39C). Additionally, large distances between the PsV accumulations and the cell surface were observed in cells treated with peptide 19-2.5. Some of the PsV accumulations reached up to several micrometers away from the cell surface (Figure 39D).

In conclusion, treatment with peptide 19-2.5 resulted in large PsV accumulations mostly located on top of the cells. This suggests that peptide 19-2.5 interferes with the transfer of PsVs from their primary attachment site to the secondary receptor complex.

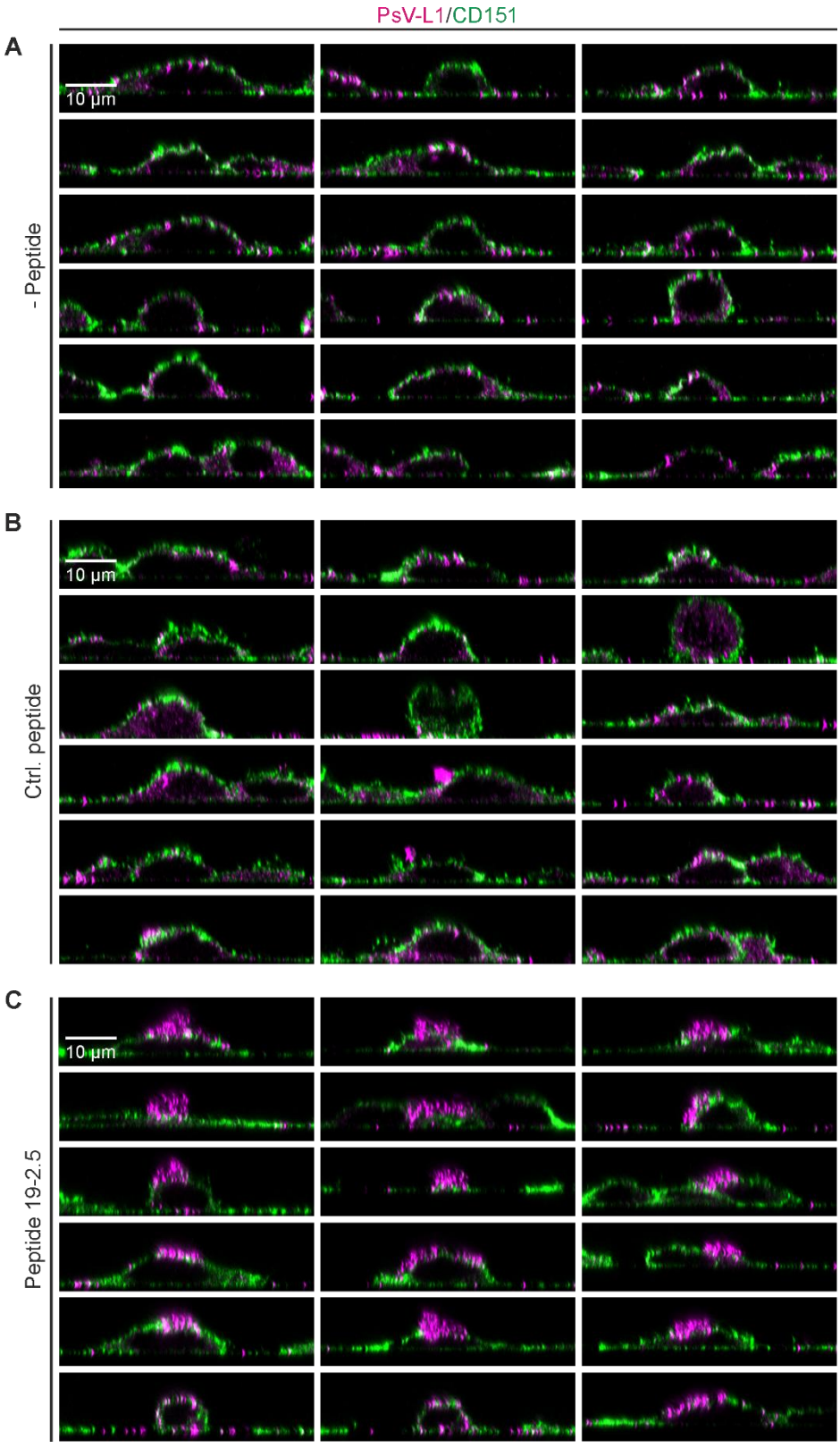

Figure 38. Variation of PsV distribution in HeLa cells.
For 1 replicate analyzed, the first 18 of the 20 recorded images are shown for each condition as overlays, employing intensity autoscaling of the L1 (magenta) and CD151 (green) channels. (A) without any peptide (- Peptide.), (B) with control peptide, and (C) with peptide 19-2.5. Figure and legend taken and modified from reference (Mikuličić et al., 2025).

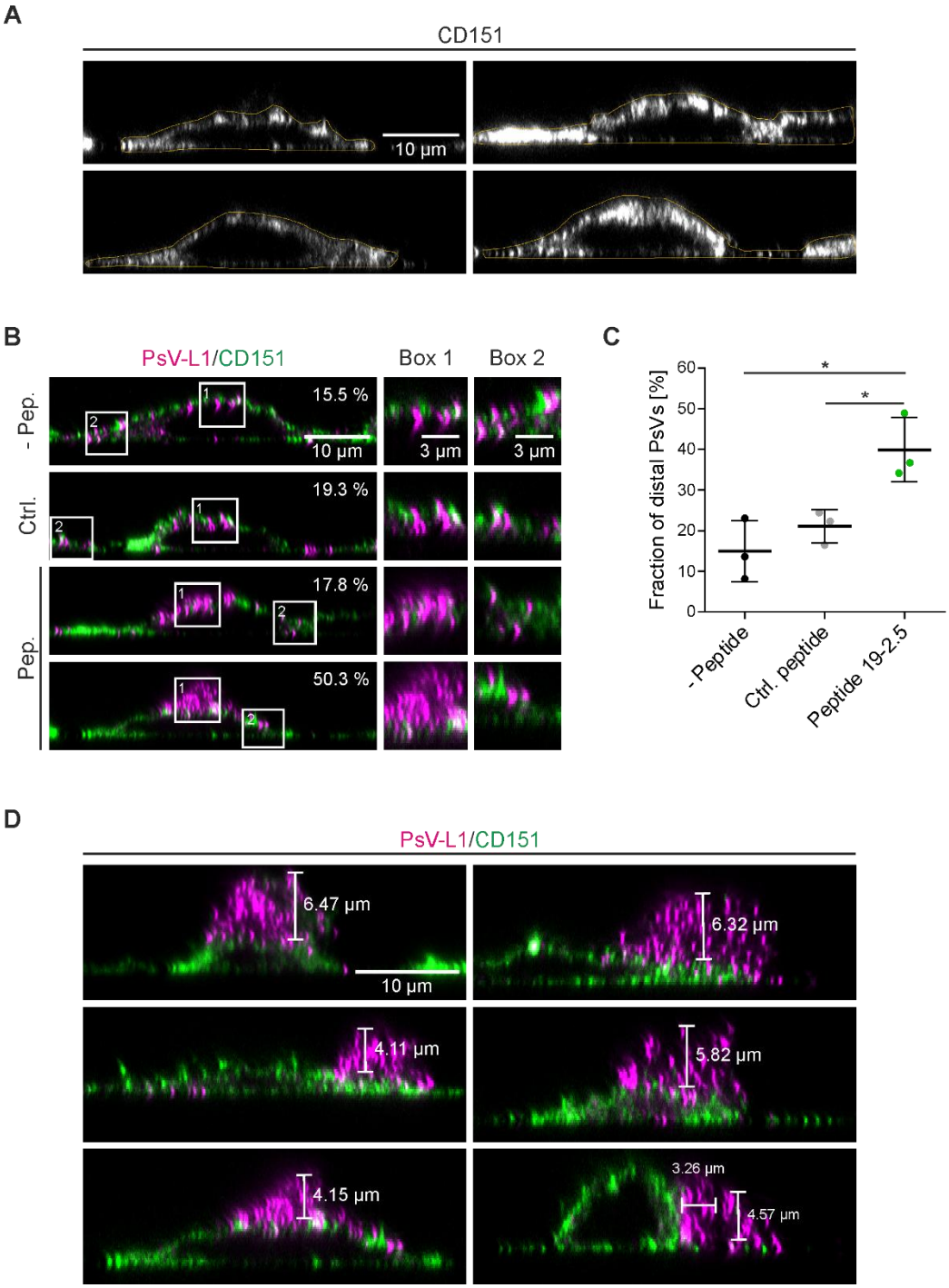

Figure 39. The peptide 19-2.5 induces large extracellular PsV accumulations.
(A) Illustration of outlines used for quantification of the distal PsV fraction. Shown are auto-scaled images. (B) In each condition, X,Z-scans/Y,Z-scans were imaged by confocal microscopy from cells exhibiting the most prominent PsV accumulations. Images of the CD151 (green) and PsV (magenta) channels of the different conditions with auto-scaled PsV intensity are shown. White boxes mark areas of magnified views. Values in the upper right indicate the fraction of distal PsVs. (C) Cells were outlined and the background-corrected PsV signal within the outline was subtracted from the total background-corrected PsV signal, yielding the signal of distal PsVs. Values are given as means ± SD (n = 3). Statistical differences between the groups were analyzed using unpaired student's t-test. (D) Anecdotal images collected from all 3 replicates of the peptide 19-2.5 condition. Overlays of auto-scaled images are shown. Bars illustrate the distance between the most distal PsVs and the cell

surface, as indicated by the CD151 cell surface staining. Figure and legend taken and modified from reference (Mikuličić et al., 2025).

5. Discussion

Human papillomaviruses infect mitotically active cells in the basal layer of the epithelium (Ozbun, Campos, 2021) and primarily bind to HSPGs on the cell surface and the ECM (Giroglou et al., 2001, Knappe et al., 2007, Surviladze et al., 2015). Moreover, the multistep entry process is asynchronous and slow with internalization half-times ranging between 4 h and 15 h (Becker et al., 2018). Beside the primary attachment site consisting of HSPGs, the tetraspanin CD151 plays a key role during the HPV entry process and is co-internalized with the virions (Finke et al., 2020b, Scheffer et al., 2013). However, it is still unclear whether CD151 plays an early role in HPV entry prior to internalization and how the HPVs are transferred from the primary receptor (HSPGs) to the secondary receptor complex. Additionally, the slow and asynchronous HPV uptake makes it difficult to analyze the virus entry by membrane microscopy. In this study, the early stages of HPV infection were investigated. The PsV/CD151 assemblies were broadly analyzed and characterized. Additionally, the actin inhibitor CytD was used to synchronize PsV uptake and revealed a crucial role of actin dynamics in filopodia for the release of viruses from the ECM and the transfer of PsVs to the cell body. Inhibition of actin-dependent processes lead to trapped PsVs in the ECM. After removal of the transfer blockade, a rapid translocation of HS-coated PsVs from the ECM to the cell body and CD151 assemblies was observed. After the transfer onto the cell body, the capsid sheds its HS coat and PsV/CD151 assemblies are endocytosed. In addition, the HSPG-binding peptide peptide 19-2.5 was used to test its potential of inhibiting HPV16 infection and its effect on CD151 assemblies. However, peptide 19-2.5 had no effect on CD151 accumulations but large viral aggregates were found situated several micrometers away from the plasma membrane after peptide 19-2.5 treatment. This visualization of viral release from the cell surface suggested a blocked transition from the primary HSPG attachment site to the secondary entry receptor complex by peptide 19-2.5.

5.1 Characterization of the PsV/CD151 entry complex

So far, the exact components of the secondary receptor complex of HPV16 infection remain unknown. However, there is evidence for a signaling-activated assembly of tetraspanin-enriched microdomains consisting of different tetraspanins, such as CD151 and CD63, integrins and growth factor receptors (Finke et al., 2020b, Florin, Lang, 2018, Mikuličić et al., 2019, Ozbun, Campos, 2021, Spoden et al., 2008). One of the key components of the secondary receptor complex is supposed to be the tetraspanin CD151 (Florin, Lang, 2018), which colocalizes with viral particles during infection (Spoden et al., 2008). Additionally, viral particles are only internalized when associated with CD151 assemblies (Scheffer et al., 2013). In this study the PsV/CD151 assemblies were analyzed and characterized to gain a better insight into HPV16 cell entry. In previous studies, large CD151 agglomerations were

observed after CD151-GFP overexpression, which colocalized with viral particles (Finke et al., 2020b). However, it remains unclear whether these large CD151 agglomerations are induced by viral particles. To clarify this question, CD151-GFP overexpressed HaCaT cells were incubated with and without PsVs and compared to untransfected HaCaTs. Membrane sheets were generated and CD151 was stained with a mAb and PsVs with a pAb against the capsid protein L1. The antibody used for immunostaining of CD151 has been shown to reliably stain endogenous CD151 and overexpressed CD151-GFP (Finke et al., 2020b). The CD151 distribution at the basal membrane was analyzed and the CD151 maxima were characterized (Figure 10). A CD151 overexpression led to a higher CD151 maxima intensity and size, independent of a PsV incubation (Figure10B and C). However, the maxima density of CD151 was slightly lower when CD151-GFP was overexpressed (Figure 10D). Therefore, overexpressed CD151 seems to merge into existing CD151 maxima (assemblies), which results in brighter and larger CD151 maxima. The increased size of CD151 maxima in CD151-GFP overexpressed cells results in a modest decrease in maxima density, presumably because adjacent maxima merge into a single maximum that cannot be resolved within the resolution limit of the microscope. No difference between cells incubated with and without PsVs was observed, indicating a PsV-independent formation of large CD151 agglomerations after CD151-GFP overexpression. When analyzing the colocalization of CD151 and PsVs by determining the PCC between PsVs and CD151, no difference between CD151-GFP overexpressed and control cells is detectable. However, for both conditions, the association is significantly higher compared to horizontally and vertically flipped (randomized) images, indicating a specific PsV/CD151 association (Figure 10E). This is line with a previous study (Finke et al., 2020b). Additionally, the PsV/CD151 association was studied in more detail (Figure 11). The PsV maxima appeared slightly larger and brighter in CD151-GFP overexpressed cells (Figure 10A). Plotting the fraction of PsVs against the PsV maxima intensity, the curve is right-shifted toward higher maxima intensities in CD151-GFP overexpressed cells (Figure 11A). One explanation could be that more PsVs can bind to the enlarged CD151 maxima in CD151-GFP overexpressed cells. However, these PsVs cannot be resolved into single maxima because of the resolution limit of the microscope and therefore merge to brighter PsV maxima. In addition, the area around a PsV maximum was analyzed for CD151 maxima. In control and CD151-GFP overexpressed cells, more maxima were found in original images compared to flipped images with significantly more CD151 maxima around PsVs in CD151-GFP overexpressed cells compared to flipped images (Figure 11B) indicating that either PsVs bind preferentially to areas with an increased number of CD151 maxima or PsVs recruit CD151 maxima toward their binding site. In addition, the shortest distance between a PsV maximum and its next nearest CD151 maximum was analyzed. In both control and CD151-GFP overexpressed cells the average distance was significantly lower compared to flipped images with a distance of 80 nm in

control cells and 100 nm in CD151-GFP overexpressed cells (Figure 11C). Therefore, the shortest distance between PsVs and CD151 in CD151-GFP overexpressed cells is significantly higher compared to control cells. Moreover, the fraction of PsVs closely associated with CD151 (distance ≤ 80 nm) is significantly lower in CD151-GFP overexpressed cells (43%) to control cells (59%). However, for both conditions, the fraction was significantly higher compared to flipped images, indicating a specific close association between PsVs and CD151 (Figure 11D). The difference in the shortest distance and the fraction of close association between untransfected control cells and CD151-GFP overexpressed cells can be explained by the lower CD151 maxima density and larger CD151 maxima size in CD151-GFP overexpressed cells. When analyzing the effect of CD151 expression levels in intact cells, large CD151 aggregates formed independent of PsV incubation (Figure 12). Additionally, the CD151 aggregates often had a three-dimensional extension into the cell (Figure 12A, intracellular) and likely represent CD151 positive endocytic structures. Nevertheless, this characterization and analysis give new insights into the PsV/CD151 association. The formation of large CD151 aggregates depends on the CD151 expression level and is a PsV independent process.

5.2 ErbB2 inhibition does not affect HPV16 entry platform formation

Next to tetraspanins, the annexin A2 heterotetramer and integrins, the epidermal growth factor receptor EGFR (also known as ErbB1) plays an important role during the HPV16 cell entry (Dziduszko, Ozbun, 2013, Finke et al., 2020b, Mikuličić et al., 2019, Ozbun, Campos, 2021, Spoden et al., 2008, Woodham et al., 2012). ErbB2, another member of the growth factor receptor family, is known to interact with EGFR on the cell surface (Ho et al., 2017). Additionally, ErbB2 was identified as a central component in a recent proteome network analysis related to internalized HPV16 PsVs (Mikuličić et al., 2024). However, it was still unclear at which stage in HPV infection ErbB2 is involved. In a recent study, the Florin lab could show, that ErbB2 plays a role in the regulation of HPV promotor activity by influencing the downstream Akt and ERK signaling pathways (Mikuličić et al., 2024). As part of the study, the role of ErbB2 during HPV16 entry platform formation was investigated. Therefore, the impact of the ErbB2 inhibitor tucatinib and modulation of the ErbB2 expression level by ErbB2 targeting siRNA on the platform formation of PsVs with CD151 was analyzed (Figure 13 and 14). Previous observations suggested that PsV surrounding CD151 patches have a local density of about 4 CD151 maxima/µm^2 in STED-microscopy (Finke et al., 2020b). When ErbB2 was inhibited by tucatinib or depleted by ErbB2 targeting siRNA about 3 – 4 CD151 maxima/µm^2 at PsV binding sites were found (Figure 13C and 14C), independent of ErbB2 inhibition or depletion. Additionally, there was no difference in the PCC between PsVs and CD151 after ErbB2 inhibition or depletion (Figure 13B and 14B). Taken together, the data suggested the inhibition or depletion of ErbB2 has no effect on CD151

crowding at PsV binding sites, or in other words: the absence of ErbB2 has no effect on HPV16 entry platform formation (Mikuličić et al., 2024).

5.3 Effect of the actin inhibitor CytD on PsV infection

Actin-dependent endocytosis is essential for the internalization of HPV16, which uses a unique, non-classical pathway distinct from clathrin- or caveolin-mediated mechanisms. HPV16 entry depends on dynamic actin polymerization rather than signaling via Rho-family GTPases or actomyosin contractility (Mikuličić, Florin, 2019, Schelhaas et al., 2012). Actin facilitates vesicle scission within uncoated, inward-budding membrane invaginations, generating small vesicles that carry virions into the cell. This process involves Na^+/H^+ exchangers, tyrosine kinases, and the actin nucleation-promoting factors WAVE and WASH, which drive branched actin assembly and vesicle formation (Brinkert et al., 2025, Fernandez et al., 2025, Schelhaas et al., 2012). Thus, HPV16 hijacks actin remodeling to enable efficient viral uptake and infection progression. To block and explore the actin-dependent transport and endocytosis of HPV16 PsVs, the cell permeable mycotoxin and actin polymerization inhibitor CytD was used. CytD is a fungal metabolite and potent inhibitor of actin polymerization that profoundly alters cellular architecture and motility. It binds with high affinity to the barbed (plus) ends of filamentous actin, blocking the addition of new monomers and thus preventing further filament elongation. This capping action arrests both actin polymerization and depolymerization, destabilizing existing filaments and disrupting the integrity of cytoskeletal networks (Mitani et al., 2025, Schliwa, 1982). In living cells, CytD induces fragmentation of stress fibers, formation of actin aggregates, and inhibition of cytokinesis due to loss of contractile ring function. Additionally, it interferes with the binding of actin-modulating proteins such as cofilin, further reducing filament turnover and remodeling (Shoji et al., 2012). Based on these effects, CytD has become an important research tool for exploring actin-dependent processes including cell migration, vesicular trafficking, and viral entry. As CytD broadly effects actin dynamics in the cell, in the first experiment, the effect of CytD on HaCaT cell shape was analyzed. Therefore, HaCaT cells were treated with CytD, and their cell shape was compared to untreated cells. Confocal images of HaCaT cells, taken in X,Y and X,Z direction (Figure X), revealed a comparable size of the basal membrane (Figure 15, compare X,Y). However, comparing images of cells taken in the X,Z direction, some differences were observed. Whereas control cells looked more regular and convex shaped with an evenly distributed cytoplasm, CytD treated cells were composed of a narrower cytoplasm with a protruded nucleus sitting on top of it (Figure 15, compare X,Z). Alterations in cell shape and cell rounding after CytD treatment has been observed in other cell types as well such as smooth muscle cells (Bruijns, Bult, 2001) and chondrocytes (Loty et al., 1995). However, the size of the basal membrane in HaCaTs seems to be unimpacted by CytD treatment. In the next step, the effect of CytD on actin-dependent PsV transport was studied at the basal membrane. Blocking of actin-

mediated transport by CytD for a total of 5 h, led to PsV accumulations at the cell periphery as PsVs were not translocated further onto the cell body (Figure 16). In control cells, PsVs were evenly distributed over the cell body. Nevertheless, it should be noted that even in control cells occasional PsV accumulations at the periphery were observed, indicating a high variability within the data. However, such cells were more frequently observed after CytD. Notably, PsV accumulations at the cell periphery were also observed when CytD was added after 1 hour, whereas addition after 3 hours resulted in PsVs primarily localized on the cell body (Figure 16A). These findings suggest that inhibition of actin dynamics by CytD prevents PsV translocation from the ECM toward the cell body and PsVs remain accumulated in the ECM area. Additionally, complete PsV binding and translocation takes longer than 1 h but presumably not longer than 3 h, as PsVs still remained accumulated in the ECM area when CytD was added after 1 h but when CytD was added after 3 h PsVs already translocated onto the cell body. In the last step, the effect of CytD on actin-dependent PsV endocytosis was analyzed (Figure 17). When CytD was added for 5 h most PsVs were visibly at the basal membrane and almost no PsV signal was visible in higher cell sections, indicating an inhibition of PsV endocytosis. Blocked PsV endocytosis upon CytD treatment in HaCaT cells was observed previously (Schelhaas et al., 2012). When CytD was added after 1 h, an increase in PsV signal in a section +1600 nm into the cell was observed (Figure 17B). Additionally, large PsVs accumulations in this cell section were mainly visible when CytD was added after 1 h (Figure 17A, compare +1600 nm), leading to the assumption that PsVs were trapped in this cell section due to the inhibited endocytosis. Previous studies showed large PsV filled invaginations upon CytD treatment (Schelhaas et al., 2012). However, when CytD was added after 3 hours, only individual PsVs were visible in the +1600 nm section, likely because endocytosis had progressed further, and the PsVs had been trafficked deeper into the cell, beyond the imaged cell sections. Taken together, CytD alters HaCaT cell morphology and, importantly, inhibits the translocation of PsVs from the ECM area to the cell body resulting in remaining PsV accumulations at the cell periphery.

5.4 CytD reversibly blocks the translocation of PsVs from the ECM to the cell body

CytD not only inhibits the translocation of PsVs to the cell body but is also known to inhibit various other actin-dependent processes that significantly affect cell physiology (Blase et al., 2009, Miranda et al., 1974). Consequently, to assess whether PsVs can continue their infection pathway normally once CytD is removed, the effects of CytD washout on PsV translocation was investigated. This approach should determine whether the blockade of actin dynamics is reversible and if PsV trafficking and internalization can resume once the actin cytoskeleton recovers. Previous studies have shown that after CytD removal, cells often undergo cytoskeletal recovery, with reassembly of actin filaments

enabling resumed cellular functions that depend on actin, such as vesicle transport and endocytosis (Miranda et al., 1974). Thus, washing off CytD provides a useful experimental strategy to evaluate if PsV trafficking and entry beyond the extracellular matrix region can proceed post-inhibition. In infection assays, a simultaneous PsV/CytD incubation for 5 h with a subsequent washout reduced PsV infection rate moderately by 29% compared to control cells (Massenberg et al., 2025). A certain degree of reduced infectivity is expected because PsVs have approximately 20% less time to complete the infection process compared to untreated cells. This shortened time window likely limits the efficiency of viral entry and intracellular trafficking, leading to decreased overall infectivity. This is in line with known effects of CytD, which disrupts actin-dependent steps critical for PsV infection, thereby slowing or partially blocking viral progression within the host cell and incubation of PsVs with CytD over the whole incubation time resulted in no infection (Massenberg et al., 2025, Schelhaas et al., 2008, Selinka et al., 2002, Selinka et al., 2007). However, the only moderately reduced infection rate after CytD washout suggests that CytD treatment is reversible and only slightly harmful, if at all (Massenberg et al., 2025). Additionally, it has been shown that PsVs translocate to the cell body with a half-time of approximately 15 minutes after CytD wash out (Massenberg et al., 2025). Analyzing the onset of PsV translocation after CytD wash off (Figure 19A and D) suggests a translocation recovery within 30 min after CytD removal. When analyzing the PCC between PsV and F-actin staining, after 5 h CytD, PsVs accumulate at the cell periphery and the edge of the F-actin staining as observed in previous experiments. This results in a negative PCC at 0 min after CytD removal as the distal PsVs and the F-actin staining partially exclude each other. However, 30 min and 60 min after CytD washout an overlap in PsV and F-actin staining can be observed, resulting in a positive PCC (Figure 19A and D). The PsV translocation recovery could take longer than 30 min “if cell spreading is in part responsible for the translocation of PsVs onto the cell body. However, this is rather unlikely, as cell spreading would increase the PCC between PsVs and F-actin under a condition where filopodia mediated transport is blocked but not cell spreading as well, which is not the case”[1] (Figure 19B and D, CytD/leupeptin). “Furthermore, CytD pre-treatment appears to synchronize uptake”[1]: Endocytic structures are more frequently observed after CytD treatment (Figure 22A and 26) “and the CD151 intensity diminishes over time only after the CytD treatment”[1] (Figure 23A). It can be therefore concluded “that the processing of the PsVs in the ECM is contributing to desynchronization and is largely completed after the 5 h pre-incubation with CytD”[1]. More PsVs “translocate to the cell surface in a coordinated fashion after CytD removal, which likely enhances the number of endocytic events compared to untreated controls”[1]. In conclusion, the CytD-mediated block of actin dynamics and PsV translocation is reversible upon CytD removal. Additionally, after CytD removal PsVs translocate onto the cell body in

[1] text passages in quotation marks taken and modified from Massenberg et al. (2025).

a more synchronized fashion, making this experimental set up a useful experimental strategy to analyze early events in PsV infection.

5.5 Subconfluent HaCaT cells as an ideal model system to analyze early entry events in HPV infection

Cell surface HS is the primary attachment site for many viruses including herpes simplex virus type 1, human cytomegalovirus, human immunodeficiency virus type 1, adenovirus type 2, dengue virus, hepatitis B virus, and vaccinia virus (Cagno et al., 2019, Giroglou et al., 2001, Tian et al., 2021). However, HPVs are somewhat unique in their primary attachment as they also bind to HS present in the ECM and extracellular basement membrane, particularly *in vivo* during the wounding and healing processes which are essential for infection. This interaction with HS in the basement membrane facilitates initial viral attachment before the virus transfers to specific cell surface receptors for cell entry (Day, Schelhaas, 2014, Kines et al., 2009, Ozbun, Campos, 2021, Schiller et al., 2010). However, many studies about HPV infection relied on non-keratinocyte cell lines or non-polarized cells, where PsVs can circumvent primary binding to HS in the ECM and can directly bind to HS on the cell surface (Ozbun, Campos, 2021). Therefore, an *in vitro* system where PsVs do not directly bind to HS at the cell surface would be a desirable model system to study especially early events in HPV infection. In previous studies it has been shown that "inhibition of HPV16 PsV transport diminishes infection only of subconfluent but not of confluent HaCaT cells by about 50% (Schelhaas et al., 2008) and merely increases the exposure of cells to virions (Smith et al., 2008). However, this increased exposure could be relevant *in vivo*, as wounding of the epidermis results in upregulation of filopodia formation (Vasioukhin et al., 2000)"[2]. Filopodia play a significant role in HPV infection by facilitating virion transport and enhancing the likelihood of reaching their target cells during wound healing. Specifically, research indicates that HPV utilizes filopodia not only for initial attachment but also for active movement toward the cell body, which increases infection efficiency. Filopodia are induced upon viral contact, driven by signaling pathways involving the GTPase Cdc42, and actin retrograde flow appears to be crucial during this process (Biondo, Meneses, 2022, Chang et al., 2016). The actin-driven transport along filopodia might be more important for HPV than previously thought, particularly during initial infection stages *in vivo*. This supports the idea that actin-dependent virion transport along filopodia could be a critical factor for efficient HPV infection, especially during wound healing where these cellular protrusions are more abundant. Filopodia formation in HaCaT cells predominantly occurs in subconfluent cultures, where cells are less densely packed and actively migrating or spreading. Live cell imaging studies show that in subconfluent HaCaT cells, dynamic actin-

[2] text passages in quotation marks taken and modified from Massenberg et al. (2025).

rich protrusions such as filopodia assemble at the leading-edge during migration or wound healing. In contrast, confluent monolayers exhibit reduced filopodia, as cells establish stable contacts and reduce motility. Consequently, filopodia preferentially form in HaCaT cells under subconfluent, migratory conditions rather than in dense, confluent monolayers (Ozawa et al., 2010). Therefore, "sub-confluent HaCaT cells, or even better single HaCaT cells, would be an ideal model system"[3] to study the "very early infection steps that involve ECM attachment and subsequent filopodia-dependent transport"[3]. HaCaT cells are composed of many binding sites for the HPV16 PsVs (Figure 19C and D). "However, as they are polarized and the binding receptors are only at the basal membrane, they remain relatively inaccessible by diffusion (Figure 19A and B). Therefore, the ECM binding that is also observed *in vivo* (Day, Schelhaas, 2014) and subsequent transport via filopodia are used upon infection of HaCaT cells that locate at the periphery of cell patches"[3] in subconfluent HaCaTs. "Here, PsVs bind to the ECM"[3] which has been shown to strongly enhance "infection of primary keratinocytes (Bienkowska-Haba et al., 2018). In contrast, HPV can readily bind to HSPGs on the cell surface of nonpolarized cells, and by this bypasses ECM mediated virus priming and the filopodia dependency"[3]. Taken together, "HaCaT cells are a valuable system for studying the very early events in HPV infection that allows for dissecting capsid interaction with ECM resident priming factors and cell surface receptors"[3].

5.6 The role of actin-mediated transport in HPV infection

Actin dynamics play a critical role in the cell entry of HPV16, facilitating a unique, clathrin- and caveolin-independent endocytic pathway. Upon attachment to host cells, HPV16 induces localized actin polymerization that helps generate membrane invaginations for viral internalization (Schelhaas et al., 2012). This process involves coordination of nucleation-promoting factors like WAVE and WASH, that mediate branched actin filament formation, enabling vesicle scission from the plasma membrane (Brinkert et al., 2025, Fernandez et al., 2025). Importantly, HPV16 entry requires healthy actin turnover, as disruption of actin polymerization inhibits infection. Contrary to classical endocytosis, HPV16 entry is independent of Rho GTPase signaling and actomyosin contractility, distinguishing it as a noncanonical, actin-mediated internalization route. The virus also exploits retrograde actin flow along filopodia, that can be inhibited by CytD, to reach the cell body, enhancing infectious uptake (Schelhaas et al., 2008, Schelhaas et al., 2012). During viral cell entry, HPV16 binds to HS in the ECM by forming a strong electrostatic bond. Therefore, for the viral release from the ECM, some processing is necessary, either through capsid rearrangements or HS cleavage. However, HS processing and KLK8 are likely not inhibited by CytD (Jamieson et al., 2021) and levels of cleaved HS (Figure 20) are unaffected by CytD treatment. Therefore, it can be assumed that PsV are primed after 5 h of

[3] text passages in quotation marks taken and modified from Massenberg et al. (2025).

incubation with CytD. The primed PsVs "may remain associated via weaker interactions"[4] in the ECM, "and actin-driven transport is required for pulling the HS-coated virions out of the sticky matrix toward the cell body"[4]. Similar sticky aggregated HS/PsV structures released from the surface of HeLa cells were observed after post-binding incubation with peptide 19-2.5, where the subsequent entry pathway was blocked (Figures 38 and 39) (Mikuličić et al., 2025). Alternatively, ECM-bound virions may encounter processing factors sequentially rather than simultaneously, requiring gradual migration through the ECM to interact with each enzyme involved. Once fully processed, virions reach the cell surface and detachment from the ECM may be facilitated by the formation of new bonds with cell surface receptors. At this stage, the PsVs and their associated receptors are transported toward the central cell body through intracellular dynamics, resulting in CD151 accumulation at viral binding sites and endocytosis (Figure 22A and 26) (Massenberg et al., 2025). When inhibiting different actin-dependent processes with either CytD (actin polymerization and depolymerization inhibition) and blebbistatin (myosin II inhibitor), both "increase PsV-HS colocalization, but blebbistatin allows partial translocation"[4] (compare Figure 27C and Figure 31C as well as Figure 27D and Figure 31D), "indicating that actin retrograde flow initiates movement, while myosin II contributes to sustained transport. As a result, virus movement can proceed to some extent after blebbistatin treatment. However, the subsequent blocking of transport at later time points reflects the inhibition of myosin II, which eventually disrupts the cytoskeletal dynamics and force generation that is necessary for sustained transport. In contrast, CytD directly interferes with actin polymerization, leading to an earlier and more persistent blocking of virus transport due to structural disruption of the filopodial tracks themselves"[4]. These findings are in line with previous studies demonstrating that HPV exploits filopodia to facilitate cell entry migrating along actin-rich protrusions at rates of several micrometers per minute (Schelhaas et al., 2008, Smith et al., 2008). Compared to the whole infection process which can take up to several hours, the translocation along actin-rich filopodia is fast and can therefore not "largely contribute to the asynchronous HPV uptake"[4]. Taken together, "the actin-driven virion transport plays a decisive role in HPV infection of isolated HaCaT cells, which cannot be modelled in nonpolarized cells, where PsVs can bind to the entire cell surface"[4].

5.7 Translocating PsVs are coated with HS, which they gradually shed during their progression toward the cell body

As described above, during the 5 h incubation with CytD, proteases within the ECM are expected to cleave HS chains. These cleavage fragments would normally diffuse out of the ECM, unless they may remain associated with PsVs. It has been previously suggested that PsVs associate with HS cleavage

[4] text passages in quotation marks taken and modified from Massenberg et al. (2025).

products (Ozbun, Campos, 2021, Surviladze et al., 2012). In line with these observations an increase in the HS signal was observed after CytD treatment (Figure 21B and 27B). However, stronger HS staining can be observed at PsVs and as well at PsV-free areas (Figure 27A). It should be noted that without the 5 h CytD incubation blocking step, "PsVs may only briefly reside in the ECM and as a result are less decorated with HS"[5]. Therefore, in the assay condition with CytD block, HS decoration of PsVs is likely enhanced compared to other experimental setups where the virus remains a shorter time associated with the ECM. When analyzing the PsVs closely associating with HS, at 0 min, treatment with CytD increases the fraction of PsVs associated with HS more than 3-fold. "At the 0 min time point post-CytD, 15% of the PsVs are closely associated with HS"[5] (Figure 29F), "but this fraction declines to 4.3% by 180 min. Considering the important role of HS as a primary attachment site, the fraction of 15% appears unexpectedly small. There are multiple possible explanations for underestimating the number of PsVs closely associated with HS. One contributing factor may be that accumulated PsVs are not well-resolved, which results in an underestimation of HS associated PsVs in particular at 0 min/CytD. Other explanations include that the HS antibody does not reach all HS epitopes in the dense matrix. Yet, another explanation could be that PsV binding to HS and antibody binding to HS is sometimes mutually exclusive, a hypothesis which is supported by data showing that the HPV capsid possesses multiple HS binding sites (Dasgupta et al., 2011, Richards et al., 2013)"[5]. Next to the increased fraction of PsVs closely associated with HS at 0 min/CytD, the PCC between PsVs and HS is increased as well at 0 min/CytD (Figure 27C). Altogether, the analysis of the fraction of PsVs closely associated with HS (Figure 29F), along with the PCC between HS and PsVs (Figure 27C), reveals that CytD treatment increases the HS/PsV association at 0 min, likely because PsVs remain accumulated in the ECM. When CytD is removed this association diminishes over time. Additionally, the PCC between PsVs and HS transiently increases specifically in the cell body region at 30 min and diminishes over the next 150 min (Figure 27D). This likely reflects the translocation of HS-coated virions to the cell body with a subsequent shedding of the HS-coat over time, potentially upon capsid rearrangement or receptor binding. Alternatively, HS-coated PsVs are internalized. However, when plotting for each PsV its distance to the next nearest HS and Itgα6 maximum, between 60 min/CytD and 180 min/CytD, the fraction of PsVs with a large distance (> 250 nm) to HS and a short distance (< 250 nm) to Itgα6 increases from 9.6% to 25.2% (Figure 30B, magenta). This fraction represents PsVs at the cell body without HS. This is inconsistent with the idea of internalized HS-coated PsVs as this would only diminish short distances to Itgα6 but not create long distances to HS as observed in this analysis. The shortening of the distance between HS and Itgα6 over time after CytD removal (Figure 28C) suggests the movement of HS toward the cell body, indirectly indicating that PsVs remain coated with HS during

[5] text passages in quotation marks taken and modified from Massenberg et al. (2025).

this translocation process. This is in line with a previous study where a reduced HS colocalization during productive infection was observed (Selinka et al., 2007). “The initial HS-coat may facilitate the formation of a complex with PsVs and cell surface receptors such as integrins or GFRs (Ballut et al., 2013, Pellegrini, 2001). This could facilitate receptor clustering and engagement as shown previously for coronavirus infection (Bugatti et al., 2025, Clausen et al., 2020, Zhang et al., 2023), as well as the binding of signaling molecules to the cell surface (Miladinova et al., 2022). Here, CD151 may support receptor clustering by binding to both integrins and GFRs (Hemler, 2005, Mikuličić et al., 2019). In addition, earlier studies suggested that cofactors like laminin-332 and growth factors further stabilize these interactions (Culp et al., 2006, Mikuličić et al., 2019, Richards et al., 2014, Surviladze et al., 2012). Furthermore, the HPV capsid has multiple binding sites for distinct functions (Richards et al., 2013) which supports the idea that HS fulfills several roles during viral entry”[6]. First, “by promoting capsid attachment, then inducing conformational changes, and finally by assisting in receptor engagement and clustering. However, HS cleavage alone is not sufficient for ECM release; active transport and capsid priming remain essential”[6] (see leupeptin effect in Figure 19B and D). “Diffusion may account for some virion movement, but filopodia-mediated transport dominates in this context”[6].

5.8 An early contact at the cell surface during HPV entry is the association with CD151

Tetraspanin CD151 is a key mediator in HPV16 cell entry, functioning as an essential component of viral entry complexes on the host cell surface. HPV16 particles co-localize with CD151 in TEMs, which organize the clustering of viral receptors such as laminin-binding integrins (Scheffer et al., 2013, Spoden et al., 2008). The interactions between CD151, integrins, and other co-receptors create a specialized entry complex that is vital for viral uptake and subsequent intracellular trafficking. When analyzing the fraction of PsVs closely associated with CD151 about 10% were closely associated at all post-translocation time points. At CytD/0 min the fraction was lower (Figure 24F). Additionally, the PCC between PsVs and CD151 was decreased at CytD/0 min as well (Figure 23B). These results suggest that “actin disruption impairs initial CD151 engagement”[6]. However, “PsVs establish contact to CD151 assemblies shortly after translocation to the cell surface, and from then on, the fraction of closely associated PsVs remains constant”[6]. This may suggest that “after the initial formation of the PsV-CD151 assemblies, they do not change in nature”[6]. Nonetheless, agglomerated, locally patched CD151 maxima that were close to PsVs were observed at later time points, especially after CytD (Figure 22A and 26). These structures likely represent endocytic structures as they continue into the cell (Figure 26). Additionally, the CD151 intensity decreased only after CytD removal (Figure 23A) suggesting a

[6] text passages in quotation marks taken and modified from Massenberg et al. (2025).

more synchronized co-internalization with endocytosed PsVs. This is supported by the observation of the large CD151 agglomerations formed at CytD/180 min that overlap with PsVs and have a clear three-dimensional extension. These likely represent tubular structures filled with several PsVs as described previously by electron microscopy (Schelhaas et al., 2012). The formation of these agglomerations cannot be detected in the analysis as only the next nearest CD151 assembly is determined. “Some further CD151 reorganization into larger entry complexes has been previously observed (Florin, Lang, 2018). This is in accordance with the observation that virions enter the cell in crowds with many of them occupying one endocytic organelle (Schelhaas et al., 2012)”[7]. However, for the fraction of “PsVs closely associated with CD151, one may have expected a larger fraction than 10%. Given that PsVs are not supposed to bind directly to CD151 and that CD151 is likely part of a larger membrane structure, like a tetraspanin enriched microdomain, the ≤ 80 nm distance criteria may be too short”[7] resulting in an underestimation of the association. Altogether, the results suggest an early contact between PsVs, and an assembly defined by CD151 at the cell surface that relies on actin-dynamics. Additionally, the early and consistent association between PsVs and CD151 across all observed time points after CytD removal suggests that PsVs preferentially bind to preformed CD151 assemblies at the cell surface, rather than recruiting CD151 to their binding site.

5.9 Therapeutic strategies to inhibit HPV16 infection

About 5% of all human cancer burdens are caused by HPV, including cervical, vulvar, vaginal, penile, anal, head and neck cancer (Baba et al., 2025, Haręża et al., 2022, Jensen et al., 2024). So far, different vaccines and screening methods have been established to prevent HPV induced cancers. However, in low- and middle-income countries the burden of HPV induced malignancies still exists due to limited access to prevention, screening and treatment (Zhang et al., 2025). Therefore, additional therapeutic approaches to reduce the global burden of HPV-associated diseases are needed. A promising therapeutic approach against a wide range of RNA and DNA viruses are antiviral peptides, that target several stages of viral infection (Mikuličić et al., 2025, Vilas Boas et al., 2019). A new class of broad-spectrum antiviral peptides known as synthetic anti-lipopolysaccharide peptides (SALPs) has been shown to inhibit entry of several viruses like herpes simplex virus (HSV) 1 and 2, HIV-1, hepatitis B, and hepatitis C to their respective host cells. SALPs bind to heparan sulfate moieties on the cell surface and thereby effectively block the attachment, and as a result, the infection of human pathogenic viruses. Additionally, to their high antiviral efficiency, they exhibit low cytotoxicity to the host cells (Hoffmann et al., 2014, Krepstakies et al., 2012). The peptide 19-2.5 is capable to inhibit the cell entry of various enveloped viruses by binding to HSPGs and sialic acids on the plasma membrane. So far it

[7] text passages in quotation marks taken and modified from Massenberg et al. (2025).

is suggested that the positively charged amino acids within peptide 19-2.5 compete with the virus for the binding to the negatively charged plasma membrane components of the host cell (Hoffmann et al., 2014, Krepstakies et al., 2012, Mikuličić et al., 2025). In this study, the influence of peptide 19-2.5 on the non-enveloped virus HPV16 was investigated by analyzing its effect on HPV cell entry complex formation. First experiments with peptide 19-2.5 and HPV 16 PsVs, showed a reduced infection and binding efficiency of PsVs when cells were treated with peptide 19-2.5 before PsV incubation (Mikuličić et al., 2025). In the next step, a post-binding experiment should reveal if the PsV association with CD151 during the viral cell entry is affected by the peptide 19-2.5. Therefore, HeLa cells were incubated for a total of 4 h with PsVs. After 1 h, peptide 19-2.5 or control peptide (Ctrl. Peptide) was added. One sample without peptide addition was taken as well (- Peptide). Additionally, one sample was taken 1 h after PsV addition, directly before peptide addition (Direct fix). When analyzing the CD151 entry complex formation, no difference between the four conditions was observed (Figure 34,35, 36 and 37). Hence, peptide 19-2.5 has no effect on the association of PsVs with CD151. However, another peptide 19-2.5 dependent effect on PsVs was observed. “Interestingly, while peptide 19-2.5 did not disrupt CD151 accumulations, further imaging revealed large viral aggregates situated away from the plasma membrane in peptide 19-2.5-treated cells. This is the first direct visualization of viral release from the cell surface following attachment, suggesting a blockade of the transition from primary HSPG attachment to interaction with the secondary receptor”[8] (Figure 38 and 39). So far, two models have been proposed to explain the transition of PsVs from HSPG attachment sites to secondary receptor engagement, that mutually are not exclusive. The so called priming model “suggests that HSPG binding induces conformational changes in capsid proteins, reducing their affinity for HSPGs and allowing transfer to the secondary receptor (Bano et al., 2024, Richards et al., 2013). The second model suggests that cleavage of HSPGs by matrix metalloproteinases liberates soluble viral complexes, which can then engage the secondary receptor (Surviladze et al., 2012). Our findings support a mixed model in which the virus is released by HSPG cleavage, and peptide 19-2.5 likely interferes with HPV infection by preventing further interactions with HSPGs, thereby inhibiting the structural activation required for effective binding to the second receptor”[8]. In another study, the dispirotripiperazine (DSTP) derivative, an HSPG-binding drug, “induced the formation of large virus aggregates and non-infectious internalization, further supporting the idea that post-binding interactions to additional HSPG moieties on the cell surface are required for the viral transfer to entry receptor molecules (Selinka et al., 2007)”[8]. Taken together, peptide 19-2.5 interferes with virus binding to HSPGs and additionally “induces the release of cell-surface bound virus particles, most likely by disrupting viral transfer to secondary receptors”[8]. Thereby it efficiently prevents HPV16 PsV

[8] text passages in quotation marks taken and modified from Mikuličić et al. (2025).

infection. “In the context of current HPV prevention strategies, peptide 19-2.5 offers a promising alternative or complement to existing measures. Importantly, the potency of peptide 19-2.5 in post-binding HPV inactivation suggests its potential as a topical microbicide capable of preventing HPV infection during or directly after sexual intercourse”[9]. In conclusion, this study underscores “the potential of peptide 19-2.5 as a preventative agent against HPV infection and provide insights into the early stages of the unconventional HPV16 entry pathway. Further research will be needed to fully elucidate its exact mechanism of action and optimize its use in clinical settings”[9].

5.10 Integrating the data into the HPV cell entry cascade

A series of coordinated steps is essential for successful HPV infection. Starting point is the initial attachment of virions to HS on the ECM or glycocalyx, mediated by electrostatic and polar interactions (Dasgupta et al., 2011, Richards et al., 2013). This binding induces conformational changes in the viral capsid (Cerqueira et al., 2015, Feng et al., 2024) and cleavage of HS chains (Surviladze et al., 2015), facilitating virion release from the ECM or glycocalyx. The virions then associate with a secondary receptor complex that forms on the cell surface over time, promoting their uptake via endocytosis. Once internalized, the viral particles are trafficked through the endosomal pathway, and the viral genome is delivered to the nucleus, where replication initiates in the dividing basal epithelial cells (Mikuličić et al., 2021, Ozbun, Campos, 2021). As outlined above, two mutually non-exclusive models are discussed regarding the transition from the primary attachment site to cell surface binding. In the priming model KLK8 (Cerqueira et al., 2015) and furin (Richards et al., 2006) subsequently cleave the capsid proteins. Afterwards, the structurally modified capsid can dissociate from the primary HS attachment site. Indeed, KLK8 inhibition blocks PsV translocation from the ECM to the cell body, whereas furin inhibition has some effects that, however, are visible in the images and not detectable in this type of analysis (Figure 19). This suggests that furin is important at later steps in the cell entry and infection cascade. This has been previously observed in studies about the role of cell surface furin in the HPV16 cell entry (Day et al., 2008, Day, Schiller, 2009, Surviladze et al., 2015). In the second model, HS cleavage promotes dissociation from primary HS attachment sites (Surviladze et al., 2012, Surviladze et al., 2015). A transfer of HS-coated PsVs from the ECM to the cell body can be observed (Figure 27, 28, 29 and 30), suggesting that PsVs associate with HS cleavage products. Taken together, the results are in line with both models of primary attachment site detachment.

Integrating the data in the cell entry cascade suggests “that after 5 h of CytD treatment, glycan-induced structural activation as well as capsid processing by proteases such as KLK8 of the capsid and HS cleavage essentially are completed ((i) in Figure 40). Subsequently, (ii) the HS decorated virion is

[9] text passages in quotation marks taken and modified from Mikuličić et al. (2025).

transported from the ECM to the cell body on filopodia, which takes about 15 min. In a time window of 30 min, PsV-CD151 association occurs. (iii) In the samples recorded 30 – 180 min after CytD removal, a loss of the HS-coat can be observed, and individual PsV-CD151 assemblies seem to merge into larger structures that are subsequently endocytosed. This model highlights the role of ECM interactions, actin dynamics, and receptor engagement in HPV16 entry"[10].

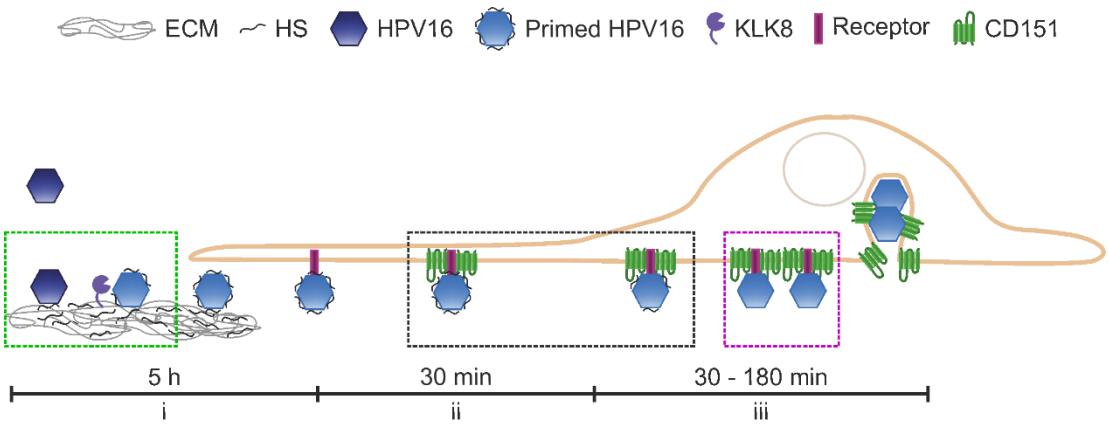

Figure 40. Model of ECM events, actin transport, and receptor engagement in HPV16 entry.
(i) During incubation with CytD for 5 h, the PsVs bind to HS of the ECM, are primed, and become coated with HS cleavage products, enabling for cell surface receptor engagement. (ii) After CytD removal, within 15 min, HS-decorated viruses move along filopodia to the cell body and associate with CD151 assemblies (completed within 30 min), likely located at the filopodia. (iii) Eventually, PsVs lose their HS coat, and individual PsV-CD151 assemblies agglomerate into larger structures (complexes), which are subsequently endocytosed. Dashed rectangles mark PsVs representing populations as defined in Figure 30. Dashed green rectangle, PsVs with a distance to HS < 250 nm and to Itgα6 > 250 nm. Dashed black rectangle, PsVs with a distance to HS < 250 nm and to Itgα6 < 250 nm. Dashed magenta rectangle, PsVs with a distance to HS > 250 nm and to Itgα6 < 250 nm. Figure and legend taken and modified from reference (Massenberg et al., 2025).

5.11 Outlook

Despite many years of research, the molecular details of HPV16 cell entry are not completely understood. While key factors such as HS attachment, secondary receptor engagement, and tetraspanin-mediated uptake have been identified, substantial gaps persist in defining the precise molecular complex that controls entry, uncoating, and trafficking toward the nucleus.

One of the foremost uncertainties is the exact molecular pathway of HPV16 internalization. Studies have shown that HPV16 uptake occurs independently of classical clathrin and caveolin endocytosis, yet the exact molecular identity of this pathway remains unknown. Although evidence supports the involvement of TEMs and actin-dependent plasma membrane invaginations, the signaling events and

[10] text passages in quotation marks taken and modified from Massenberg et al. (2025).

structural intermediates driving vesicle formation are poorly defined. Additionally, the relative contributions of noncanonical endocytic routes, such as macropinocytosis-like processes, are debated, since some experimental outcomes suggest a hybrid mechanism that overlaps with known endocytic pathways (Day, Schelhaas, 2014, Horvath et al., 2010, Sapp, Bienkowska-Haba, 2009).

Moreover, it is still unclear how HPV16 transitions from initial binding to HS to secondary receptors on the keratinocyte surface. While conformational changes exposing L2 and integrin-binding domains have been characterized, the timing, recruitment sequence, and identity of the functional secondary receptor complex remain unknow. Some studies propose the participation of laminin-binding integrins and tetraspanins such as CD151, but the molecular details of receptor handoff and its linkage to endocytosis need clarification (Day, Schelhaas, 2014, Ozbun, Campos, 2021). Actin remodeling is essential for HPV16 endocytosis, yet the mechanistic coordination between actin polymerization and vesicle scission is still unknown. The involvement of actin nucleation-promoting factors like WAVE and WASH has been demonstrated, but their recruitment signals and interactions with tetraspanin scaffolds require further investigation (Brinkert et al., 2025, Fernandez et al., 2025). It is also unclear how actin dynamics couple with endosomal maturation processes controlling viral trafficking toward perinuclear regions.

6. References

Aggarwal, S.; Agarwal, P.; Singh, A. K. Human papilloma virus vaccines: A comprehensive narrative review. *Cancer treatment and research communications* 2023, *37*, 100780. DOI: 10.1016/j.ctarc.2023.100780.

Aranda-Rivera, A. K.; Cruz-Gregorio, A.; Briones-Herrera, A.; Pedraza-Chaverri, J. Regulation of autophagy by high- and low-risk human papillomaviruses. *Reviews in medical virology* 2021, *31* (2), e2169. DOI: 10.1002/rmv.2169.

Aydin, I.; Villalonga-Planells, R.; Greune, L.; Bronnimann, M. P.; Calton, C. M.; Becker, M.; Lai, K.-Y.; Campos, S. K.; Schmidt, M. A.; Schelhaas, M. A central region in the minor capsid protein of papillomaviruses facilitates viral genome tethering and membrane penetration for mitotic nuclear entry. *PLoS pathogens* 2017, *13* (5), e1006308. DOI: 10.1371/journal.ppat.1006308.

Aydin, I.; Weber, S.; Snijder, B.; Samperio Ventayol, P.; Kühbacher, A.; Becker, M.; Day, P. M.; Schiller, J. T.; Kann, M.; Pelkmans, L.; Helenius, A.; Schelhaas, M. Large scale RNAi reveals the requirement of nuclear envelope breakdown for nuclear import of human papillomaviruses. *PLoS pathogens* 2014, *10* (5), e1004162. DOI: 10.1371/journal.ppat.1004162.

Baba, S. K.; Alblooshi, S. S. E.; Yaqoob, R.; Behl, S.; Al Saleem, M.; Rakha, E. A.; Malik, F.; Singh, M.; Macha, M. A.; Akhtar, M. K.; Houry, W. A.; Bhat, A. A.; Al Menhali, A.; Zheng, Z.-M.; Mirza, S. Human papilloma virus (HPV) mediated cancers: an insightful update. *Journal of translational medicine* 2025, *23* (1), 483. DOI: 10.1186/s12967-025-06470-x.

Baker, T. S.; Newcomb, W. W.; Olson, N. H.; Cowsert, L. M.; Olson, C.; Brown, J. C. Structures of bovine and human papillomaviruses. Analysis by cryoelectron microscopy and three-dimensional image reconstruction. *Biophysical journal* 1991, *60* (6), 1445–1456. DOI: 10.1016/S0006-3495(91)82181-6.

Ballut, L.; Sapay, N.; Chautard, E.; Imberty, A.; Ricard-Blum, S. Mapping of heparin/heparan sulfate binding sites on αvβ3 integrin by molecular docking. *Journal of molecular recognition : JMR* 2013, *26* (2), 76–85. DOI: 10.1002/jmr.2250.

Bano, F.; Soria-Martinez, L.; van Bodegraven, D.; Thorsteinsson", K.; Brown, A. M.; Fels, I.; Snyder, N. L.; Bally, M.; Schelhaas, M. Site-specific sulfations regulate the physicochemical properties of papillomavirus-heparan sulfate interactions for entry. *Science advances* 2024, *10* (40), eado8540. DOI: 10.1126/sciadv.ado8540.

Becker, M.; Greune, L.; Schmidt, M. A.; Schelhaas, M. Extracellular Conformational Changes in the Capsid of Human Papillomaviruses Contribute to Asynchronous Uptake into Host Cells. *Journal of virology* 2018, *92* (11). DOI: 10.1128/jvi.02106-17.

Bienkowska-Haba, M.; Luszczek, W.; Myers, J. E.; Keiffer, T. R.; DiGiuseppe, S.; Polk, P.; Bodily, J. M.; Scott, R. S.; Sapp, M. A new cell culture model to genetically dissect the complete human papillomavirus life cycle. *PLoS pathogens* 2018, *14* (3), e1006846. DOI: 10.1371/journal.ppat.1006846.

Bienkowska-Haba, M.; Patel, H. D.; Sapp, M. Target cell cyclophilins facilitate human papillomavirus type 16 infection. *PLoS pathogens* 2009, *5* (7), e1000524. DOI: 10.1371/journal.ppat.1000524.

Bienkowska-Haba, M.; Sapp, M. The cytoskeleton in papillomavirus infection. *Viruses* 2011, *3* (3), 260–271. DOI: 10.3390/v3030260.

Biondo, A.; Meneses, P. I. The Process of Filopodia Induction during HPV Infection. *Viruses* 2022, *14* (6). DOI: 10.3390/v14061150.

Blase, C.; Becker, D.; Kappel, S.; Bereiter-Hahn, J. Microfilament dynamics during HaCaT cell volume regulation. *European journal of cell biology* 2009, *88* (3), 131–139. DOI: 10.1016/j.ejcb.2008.10.003.

Boccardo, E. New approaches for infective HPV detection, quantification and inactivation: Preventing accidental virus transmission in medical settings. *EBioMedicine* 2021, *64*, 103222. DOI: 10.1016/j.ebiom.2021.103222.

Boukamp, P.; Petrussevska, R. T.; Breitkreutz, D.; Hornung, J.; Markham, A.; Fusenig, N. E. Normal keratinization in a spontaneously immortalized aneuploid human keratinocyte cell line. *The Journal of cell biology* 1988, *106* (3), 761–771. DOI: 10.1083/jcb.106.3.761.

Brinkert, P.; Krebs, L.; Samperio Ventayol, P.; Greune, L.; Bannach, C.; Amakiri, C.; Bucher, D.; Kollasser, J.; Dersch, P.; Boulant, S.; Stradal, T. E. B.; Schelhaas, M. The actin nucleation promoting factor WASH facilitates clathrin-independent endocytosis of human papillomaviruses. *EMBO reports* [Online] 2025.

Bruening, J.; Lasswitz, L.; Banse, P.; Kahl, S.; Marinach, C.; Vondran, F. W.; Kaderali, L.; Silvie, O.; Pietschmann, T.; Meissner, F.; Gerold, G. Hepatitis C virus enters liver cells using the CD81 receptor complex proteins calpain-5 and CBLB. *PLoS pathogens* 2018, *14* (7), e1007111. DOI: 10.1371/journal.ppat.1007111.

Bruijns, R. H.; Bult, H. Effects of local cytochalasin D delivery on smooth muscle cell migration and on collar-induced intimal hyperplasia in the rabbit carotid artery. *British journal of pharmacology* 2001, *134* (3), 473–483. DOI: 10.1038/sj.bjp.0704281.

Buck, C. B.; Cheng, N.; Thompson, C. D.; Lowy, D. R.; Steven, A. C.; Schiller, J. T.; Trus, B. L. Arrangement of L2 within the papillomavirus capsid. *Journal of virology* 2008, *82* (11), 5190–5197. DOI: 10.1128/JVI.02726-07.

Buck, C. B.; Pastrana, D. V.; Lowy, D. R.; Schiller, J. T. Efficient intracellular assembly of papillomaviral vectors. *Journal of virology* 2004, *78* (2), 751–757. DOI: 10.1128/jvi.78.2.751-757.2004.

Bugatti, A.; Zani, A.; Bardelli, M.; Giovanetti, M.; Ravelli, C.; Ciccozzi, M.; Caruso, A.; Caccuri, F. Heparan sulfate proteoglycans remodel SARS-CoV-2 spike conformation to allow integrin interaction and infection of endothelial cells. *Frontiers in cellular and infection microbiology* 2025, *15*, 1552116. DOI: 10.3389/fcimb.2025.1552116.

Cagno, V.; Tseligka, E. D.; Jones, S. T.; Tapparel, C. Heparan Sulfate Proteoglycans and Viral Attachment: True Receptors or Adaptation Bias? *Viruses* 2019, *11* (7). DOI: 10.3390/v11070596.

Calton, C. M.; Bronnimann, M. P.; Manson, A. R.; Li, S.; Chapman, J. A.; Suarez-Berumen, M.; Williamson, T. R.; Molugu, S. K.; Bernal, R. A.; Campos, S. K. Translocation of the papillomavirus L2/vDNA complex across the limiting membrane requires the onset of mitosis. *PLoS pathogens* 2017, *13* (5), e1006200. DOI: 10.1371/journal.ppat.1006200.

Cerqueira, C.; Samperio Ventayol, P.; Vogeley, C.; Schelhaas, M. Kallikrein-8 Proteolytically Processes Human Papillomaviruses in the Extracellular Space To Facilitate Entry into Host Cells. *Journal of virology* 2015, *89* (14), 7038–7052. DOI: 10.1128/JVI.00234-15.

Chang, K.; Baginski, J.; Hassan, S. F.; Volin, M.; Shukla, D.; Tiwari, V. Filopodia and Viruses: An Analysis of Membrane Processes in Entry Mechanisms. *Frontiers in microbiology* 2016, *7*, 300. DOI: 10.3389/fmicb.2016.00300.

Charrin, S.; Jouannet, S.; Boucheix, C.; Rubinstein, E. Tetraspanins at a glance. *Journal of cell science* 2014, *127* (Pt 17), 3641–3648. DOI: 10.1242/jcs.154906.

Charrin, S.; Le Naour, F.; Silvie, O.; Milhiet, P.-E.; Boucheix, C.; Rubinstein, E. Lateral organization of membrane proteins: tetraspanins spin their web. *The Biochemical journal* 2009, *420* (2), 133–154. DOI: 10.1042/BJ20082422.

Chen, H.; Guo, K.; Bai, Z.; Lu, L.; Liu, B.; Zhang, J.; Zhong, M.; Xu, C.; Chen, W.; Huang, A.; Ding, Y. Advances in the Prevention of Cervical Cancer by Anti-Human Papillomavirus Agents. *Cancer medicine* 2025, *14* (7), e70847. DOI: 10.1002/cam4.70847.

Clausen, T. M.; Sandoval, D. R.; Spliid, C. B.; Pihl, J.; Perrett, H. R.; Painter, C. D.; Narayanan, A.; Majowicz, S. A.; Kwong, E. M.; McVicar, R. N.; Thacker, B. E.; Glass, C. A.; Yang, Z.; Torres, J. L.;

Golden, G. J.; Bartels, P. L.; Porell, R. N.; Garretson, A. F.; Laubach, L.; Feldman, J.; Yin, X.; Pu, Y.; Hauser, B. M.; Caradonna, T. M.; Kellman, B. P.; Martino, C.; Gordts, P. L. S. M.; Chanda, S. K.; Schmidt, A. G.; Godula, K.; Leibel, S. L.; Jose, J.; Corbett, K. D.; Ward, A. B.; Carlin, A. F.; Esko, J. D. SARS-CoV-2 Infection Depends on Cellular Heparan Sulfate and ACE2. *Cell* 2020, *183* (4), 1043-1057.e15. DOI: 10.1016/j.cell.2020.09.033.

Culp, T. D.; Budgeon, L. R.; Marinkovich, M. P.; Meneguzzi, G.; Christensen, N. D. Keratinocyte-secreted laminin 5 can function as a transient receptor for human papillomaviruses by binding virions and transferring them to adjacent cells. *Journal of virology* 2006, *80* (18), 8940–8950. DOI: 10.1128/JVI.00724-06.

Dasgupta, J.; Bienkowska-Haba, M.; Ortega, M. E.; Patel, H. D.; Bodevin, S.; Spillmann, D.; Bishop, B.; Sapp, M.; Chen, X. S. Structural basis of oligosaccharide receptor recognition by human papillomavirus. *The Journal of biological chemistry* 2011, *286* (4), 2617–2624. DOI: 10.1074/jbc.m110.160184.

David, G.; Bai, X. M.; van der Schueren, B.; Cassiman, J. J.; van den Berghe, H. Developmental changes in heparan sulfate expression: in situ detection with mAbs. *The Journal of cell biology* 1992, *119* (4), 961–975. DOI: 10.1083/jcb.119.4.961.

Day, P. M.; Gambhira, R.; Roden, R. B. S.; Lowy, D. R.; Schiller, J. T. Mechanisms of human papillomavirus type 16 neutralization by l2 cross-neutralizing and l1 type-specific antibodies. *Journal of virology* 2008, *82* (9), 4638–4646. DOI: 10.1128/JVI.00143-08.

Day, P. M.; Schelhaas, M. Concepts of papillomavirus entry into host cells. *Current opinion in virology* 2014, *4*, 24–31. DOI: 10.1016/j.coviro.2013.11.002.

Day, P. M.; Schiller, J. T. The role of furin in papillomavirus infection. *Future microbiology* 2009, *4* (10), 1255–1262. DOI: 10.2217/fmb.09.86.

Della Fera, A. N.; Warburton, A.; Coursey, T. L.; Khurana, S.; McBride, A. A. Persistent Human Papillomavirus Infection. *Viruses* 2021, *13* (2). DOI: 10.3390/v13020321.

DiGiuseppe, S.; Bienkowska-Haba, M.; Sapp, M. Human Papillomavirus Entry: Hiding in a Bubble. *Journal of virology* 2016, *90* (18), 8032–8035. DOI: 10.1128/JVI.01065-16.

Domingo, E. Introduction to virus origins and their role in biological evolution. *Virus as Populations*; Elsevier, 2020; pp 1–33. DOI: 10.1016/B978-0-12-816331-3.00001-5.

Doorbar, J.; Egawa, N.; Griffin, H.; Kranjec, C.; Murakami, I. Human papillomavirus molecular biology and disease association. *Reviews in medical virology* 2015, *25 Suppl 1* (Suppl Suppl 1), 2–23. DOI: 10.1002/rmv.1822.

Doorbar, J.; Ely, S.; Sterling, J.; McLean, C.; Crawford, L. Specific interaction between HPV-16 E1-E4 and cytokeratins results in collapse of the epithelial cell intermediate filament network. *Nature* 1991, *352* (6338), 824–827. DOI: 10.1038/352824a0.

Doorbar, J.; Gallimore, P. H. Identification of proteins encoded by the L1 and L2 open reading frames of human papillomavirus 1a. *Journal of virology* 1987, *61* (9), 2793–2799. DOI: 10.1128/JVI.61.9.2793-2799.1987.

Dreer, M.; van de Poel, S.; Stubenrauch, F. Control of viral replication and transcription by the papillomavirus E8^E2 protein. *Virus research* 2017, *231*, 96–102. DOI: 10.1016/j.virusres.2016.11.005.

Dziduszko, A.; Ozbun, M. A. Annexin A2 and S100A10 regulate human papillomavirus type 16 entry and intracellular trafficking in human keratinocytes. *Journal of virology* 2013, *87* (13), 7502–7515. DOI: 10.1128/jvi.00519-13.

Earnest, J. T.; Hantak, M. P.; Park, J.-E.; Gallagher, T. Coronavirus and influenza virus proteolytic priming takes place in tetraspanin-enriched membrane microdomains. *Journal of virology* 2015, *89* (11), 6093–6104. DOI: 10.1128/JVI.00543-15.

Ebrahimi, N.; Yousefi, Z.; Khosravi, G.; Malayeri, F. E.; Golabi, M.; Askarzadeh, M.; Shams, M. H.; Ghezelbash, B.; Eskandari, N. Human papillomavirus vaccination in low- and middle-income countries: progression, barriers, and future prospective. *Frontiers in immunology* 2023, *14*, 1150238. DOI: 10.3389/fimmu.2023.1150238.

Elkin, M.; Ilan, N.; Ishai-Michaeli, R.; Friedmann, Y.; Papo, O.; Pecker, I.; Vlodavsky, I. Heparanase as mediator of angiogenesis: mode of action. *FASEB journal : official publication of the Federation of American Societies for Experimental Biology* 2001, *15* (9), 1661–1663. DOI: 10.1096/fj.00-0895fje.

Evander, M.; Frazer, I. H.; Payne, E.; Qi, Y. M.; Hengst, K.; McMillan, N. A. Identification of the alpha6 integrin as a candidate receptor for papillomaviruses. *Journal of virology* 1997, *71* (3), 2449–2456. DOI: 10.1128/JVI.71.3.2449-2456.1997.

Feng, Y.; van Bodegraven, D.; Kádek, A.; L B Munguira, I.; Soria-Martinez, L.; Nentwich, S.; Saha, S.; Chardon, F.; Kavan, D.; Uetrecht, C.; Schelhaas, M.; Roos, W. H. Glycan-induced structural activation softens the human papillomavirus capsid for entry through reduction of intercapsomere flexibility. *Nature communications* 2024, *15* (1), 10076. DOI: 10.1038/s41467-024-54373-0.

Fermin, G. Host Range, Host–Virus Interactions, and Virus Transmission. *Viruses*; Elsevier, 2018; pp 101–134. DOI: 10.1016/B978-0-12-811257-1.00005-X.

Fernandez, D. J.; Cheng, S.; Prins, R.; Hamm-Alvarez, S. F.; Kast, W. M. Human Papillomavirus Type 16 Stimulates WAVE1- and WAVE2-Dependent Actin Protrusions for Endocytic Entry. *Viruses* 2025, *17* (4). DOI: 10.3390/v17040542.

Finch, J. T.; Klug, A. The structure of viruses of the papilloma-polyoma type 3. Structure of rabbit papilloma virus, with an appendix on the topography of contrast in negative-staining for electron-microscopy. *Journal of molecular biology* 1965, *13* (1), 1–12. DOI: 10.1016/S0022-2836(65)80075-4.

Finke, J.; Hitschler, L.; Boller, K.; Florin, L.; Lang, T. HPV caught in the tetraspanin web? *Medical microbiology and immunology* 2020a, *209* (4), 447–459. DOI: 10.1007/s00430-020-00683-1.

Finke, J.; Mikuličić, S.; Loster, A.-L.; Gawlitza, A.; Florin, L.; Lang, T. Anatomy of a viral entry platform differentially functionalized by integrins α3 and α6. *Scientific reports* 2020b, *10* (1), 5356. DOI: 10.1038/s41598-020-62202-9.

Florin, L.; Lang, T. Tetraspanin Assemblies in Virus Infection. *Frontiers in immunology* 2018, *9*, 1140. DOI: 10.3389/fimmu.2018.01140.

Giroglou, T.; Florin, L.; Schäfer, F.; Streeck, R. E.; Sapp, M. Human papillomavirus infection requires cell surface heparan sulfate. *Journal of virology* 2001, *75* (3), 1565–1570. DOI: 10.1128/JVI.75.3.1565-1570.2001.

Goetschius, D. J.; Hartmann, S. R.; Subramanian, S.; Bator, C. M.; Christensen, N. D.; Hafenstein, S. L. High resolution cryo EM analysis of HPV16 identifies minor structural protein L2 and describes capsid flexibility. *Scientific reports* 2021, *11* (1), 3498. DOI: 10.1038/s41598-021-83076-5.

Graham, S. V. Keratinocyte Differentiation-Dependent Human Papillomavirus Gene Regulation. *Viruses* 2017a, *9* (9). DOI: 10.3390/v9090245.

Graham, S. V. The human papillomavirus replication cycle, and its links to cancer progression: a comprehensive review. *Clinical science (London, England : 1979)* 2017b, *131* (17), 2201–2221. DOI: 10.1042/CS20160786.

Gräßel, L.; Fast, L. A.; Scheffer, K. D.; Boukhallouk, F.; Spoden, G. A.; Tenzer, S.; Boller, K.; Bago, R.; Rajesh, S.; Overduin, M.; Berditchevski, F.; Florin, L. The CD63-Syntenin-1 Complex Controls Post-Endocytic Trafficking of Oncogenic Human Papillomaviruses. *Scientific reports* 2016, *6*, 32337. DOI: 10.1038/srep32337.

Guion, L.; Bienkowska-Haba, M.; DiGiuseppe, S.; Florin, L.; Sapp, M. PML nuclear body-residing proteins sequentially associate with HPV genome after infectious nuclear delivery. *PLoS pathogens* 2019, *15* (2), e1007590. DOI: 10.1371/journal.ppat.1007590.

Hantak, M. P.; Qing, E.; Earnest, J. T.; Gallagher, T. Tetraspanins: Architects of Viral Entry and Exit Platforms. *Journal of virology* 2019, *93* (6). DOI: 10.1128/JVI.01429-17.

Haręża, D. A.; Wilczyński, J. R.; Paradowska, E. Human Papillomaviruses as Infectious Agents in Gynecological Cancers. Oncogenic Properties of Viral Proteins. *International journal of molecular sciences* 2022, *23* (3). DOI: 10.3390/ijms23031818.

Hartmann, S. R.; Goetschius, D. J.; Hu, J.; Graff, J. J.; Bator, C. M.; Christensen, N. D.; Hafenstein, S. L. Cryo EM Analysis Reveals Inherent Flexibility of Authentic Murine Papillomavirus Capsids. *Viruses* 2021, *13* (10). DOI: 10.3390/v13102023.

Hemler, M. E. Specific tetraspanin functions. *The Journal of cell biology* 2001, *155* (7), 1103–1107. DOI: 10.1083/jcb.200108061.

Hemler, M. E. Tetraspanin functions and associated microdomains. *Nature reviews. Molecular cell biology* 2005, *6* (10), 801–811. DOI: 10.1038/nrm1736.

Ho, J.; Moyes, D. L.; Tavassoli, M.; Naglik, J. R. The Role of ErbB Receptors in Infection. *Trends in microbiology* 2017, *25* (11), 942–952. DOI: 10.1016/j.tim.2017.04.009.

Hochdorfer, D.; Florin, L.; Sinzger, C.; Lieber, D. Tetraspanin CD151 Promotes Initial Events in Human Cytomegalovirus Infection. *Journal of virology* 2016, *90* (14), 6430–6442. DOI: 10.1128/jvi.00145-16.

Hochheimer, N.; Sies, R.; Aschenbrenner, A. C.; Schneider, D.; Lang, T. Classes of non-conventional tetraspanins defined by alternative splicing. *Scientific reports* 2019, *9* (1), 14075. DOI: 10.1038/s41598-019-50267-0.

Hoffmann, J.; Schneider, C.; Heinbockel, L.; Brandenburg, K.; Reimer, R.; Gabriel, G. A new class of synthetic anti-lipopolysaccharide peptides inhibits influenza A virus replication by blocking cellular attachment. *Antiviral research* 2014, *104*, 23–33. DOI: 10.1016/j.antiviral.2014.01.015.

Horvath, C. A. J.; Boulet, G. A. V.; Renoux, V. M.; Delvenne, P. O.; Bogers, J.-P. J. Mechanisms of cell entry by human papillomaviruses: an overview. *Virology journal* 2010, *7*, 11. DOI: 10.1186/1743-422X-7-11.

Jamieson, R. R.; Stasiak, S. E.; Polio, S. R.; Augspurg, R. D.; McCormick, C. A.; Ruberti, J. W.; Parameswaran, H. Stiffening of the extracellular matrix is a sufficient condition for airway hyperreactivity. *Journal of applied physiology (Bethesda, Md. : 1985)* 2021, *130* (6), 1635–1645. DOI: 10.1152/japplphysiol.00554.2020.

Jensen, J. E.; Becker, G. L.; Jackson, J. B.; Rysavy, M. B. Human Papillomavirus and Associated Cancers: A Review. *Viruses* 2024, *16* (5). DOI: 10.3390/v16050680.

Joyce, J. G.; Tung, J. S.; Przysiecki, C. T.; Cook, J. C.; Lehman, E. D.; Sands, J. A.; Jansen, K. U.; Keller, P. M. The L1 major capsid protein of human papillomavirus type 11 recombinant virus-like particles interacts with heparin and cell-surface glycosaminoglycans on human keratinocytes. *The Journal of biological chemistry* 1999, *274* (9), 5810–5822. DOI: 10.1074/jbc.274.9.5810.

Kines, R. C.; Thompson, C. D.; Lowy, D. R.; Schiller, J. T.; Day, P. M. The initial steps leading to papillomavirus infection occur on the basement membrane prior to cell surface binding. *Proceedings of the National Academy of Sciences of the United States of America* 2009, *106* (48), 20458–20463. DOI: 10.1073/pnas.0908502106.

Kloc, M.; Uosef, A.; Wosik, J.; Kubiak, J. Z.; Ghobrial, R. M. Virus interactions with the actin cytoskeleton-what we know and do not know about SARS-CoV-2. *Archives of virology* 2022, *167* (3), 737–749. DOI: 10.1007/s00705-022-05366-1.

Knappe, M.; Bodevin, S.; Selinka, H.-C.; Spillmann, D.; Streeck, R. E.; Chen, X. S.; Lindahl, U.; Sapp, M. Surface-exposed amino acid residues of HPV16 L1 protein mediating interaction with cell surface

heparan sulfate. *The Journal of biological chemistry* 2007, *282* (38), 27913–27922. DOI: 10.1074/jbc.M705127200.

Kovács, M.; Tóth, J.; Hetényi, C.; Málnási-Csizmadia, A.; Sellers, J. R. Mechanism of blebbistatin inhibition of myosin II. *The Journal of biological chemistry* 2004, *279* (34), 35557–35563. DOI: 10.1074/jbc.M405319200.

Kreimer, A. R.; Clifford, G. M.; Boyle, P.; Franceschi, S. Human papillomavirus types in head and neck squamous cell carcinomas worldwide: a systematic review. *Cancer epidemiology, biomarkers & prevention : a publication of the American Association for Cancer Research, cosponsored by the American Society of Preventive Oncology* 2005, *14* (2), 467–475. DOI: 10.1158/1055-9965.EPI-04-0551.

Krepstakies, M.; Lucifora, J.; Nagel, C.-H.; Zeisel, M. B.; Holstermann, B.; Hohenberg, H.; Kowalski, I.; Gutsmann, T.; Baumert, T. F.; Brandenburg, K.; Hauber, J.; Protzer, U. A new class of synthetic peptide inhibitors blocks attachment and entry of human pathogenic viruses. *The Journal of infectious diseases* 2012, *205* (11), 1654–1664. DOI: 10.1093/infdis/jis273.

Lauber, C.; Seitz, S. Opportunities and Challenges of Data-Driven Virus Discovery. *Biomolecules* 2022, *12* (8). DOI: 10.3390/biom12081073.

Laurie, C.; El-Zein, M.; Botting-Provost, S.; Tota, J. E.; Tellier, P.-P.; Coutlée, F.; Burchell, A. N.; Franco, E. L. Efficacy and safety of a self-applied carrageenan-based gel to prevent human papillomavirus infection in sexually active young women (CATCH study): an exploratory phase IIB randomised, placebo-controlled trial. *EClinicalMedicine* 2023, *60*, 102038. DOI: 10.1016/j.eclinm.2023.102038.

Lin, C. H.; Espreafico, E. M.; Mooseker, M. S.; Forscher, P. Myosin drives retrograde F-actin flow in neuronal growth cones. *Neuron* 1996, *16* (4), 769–782. DOI: 10.1016/s0896-6273(00)80097-5.

Ling, K.; Yang, L.; Yang, N.; Chen, M.; Wang, Y.; Liang, S.; Li, Y.; Jiang, L.; Yan, P.; Liang, Z. Gene Targeting of HPV18 E6 and E7 Synchronously by Nonviral Transfection of CRISPR/Cas9 System in Cervical Cancer. *Human gene therapy* 2020, *31* (5-6), 297–308. DOI: 10.1089/hum.2019.246.

Loty, S.; Forest, N.; Boulekbache, H.; Sautier, J. M. Cytochalasin D induces changes in cell shape and promotes in vitro chondrogenesis: a morphological study. *Biology of the cell* 1995, *83* (2-3), 149–161. DOI: 10.1016/0248-4900(96)81303-7.

Lowe, J.; Panda, D.; Rose, S.; Jensen, T.; Hughes, W. A.; Tso, F. Y.; Angeletti, P. C. Evolutionary and structural analyses of alpha-papillomavirus capsid proteins yields novel insights into L2 structure and interaction with L1. *Virology journal* 2008, *5*, 150. DOI: 10.1186/1743-422X-5-150.

Lu, Y.; Xie, Z.; Luo, G.; Yan, H.; Qian, H.-Z.; Fu, L.; Wang, B.; Huang, R.; Cao, F.; Lin, H.; You, R.; Tan, L.; Yu, T.; Chen, M.; Li, C.; Liu, X.; Lei, W.; Zou, H. Global burden of oropharyngeal cancer attributable to human papillomavirus by anatomical subsite and geographic region. *Cancer epidemiology* 2022, *78*, 102140. DOI: 10.1016/j.canep.2022.102140.

Mahajan, I.; Kadam, A.; McCann, L.; Ghose, A.; Wakeham, K.; Dhillon, N. S.; Stanway, S.; Boussios, S.; Banerjee, S.; Priyadarshini, A.; Sirohi, B.; Torode, J. S.; Mitra, S. Early adoption of innovation in HPV prevention strategies: closing the gap in cervical cancer. *Ecancermedicalscience* 2024, *18*, 1762. DOI: 10.3332/ecancer.2024.1762.

Martel, C. de; Plummer, M.; Vignat, J.; Franceschi, S. Worldwide burden of cancer attributable to HPV by site, country and HPV type. *International journal of cancer* 2017, *141* (4), 664–670. DOI: 10.1002/ijc.30716.

Massenberg, A.; Homsi, Y.; Schneider, C. N.; Mikuličić, S.; Döring, T.; Florin, L.; Lang, T. *A rapid transfer of virions coated with heparan sulfate from the ECM to CD151 defines an early step in the human papillomavirus infection cascade* 2025. DOI: 10.1101/2025.04.17.649398.

McBride, A. A. Mechanisms and strategies of papillomavirus replication. *Biological chemistry* 2017, *398* (8), 919–927. DOI: 10.1515/hsz-2017-0113.

McBride, A. A. Human papillomaviruses: diversity, infection and host interactions. *Nature reviews. Microbiology* 2022, *20* (2), 95–108. DOI: 10.1038/s41579-021-00617-5.

McBride, A. A.; Oliveira, J. G.; McPhillips, M. G. Partitioning viral genomes in mitosis: same idea, different targets. *Cell cycle (Georgetown, Tex.)* 2006, *5* (14), 1499–1502. DOI: 10.4161/cc.5.14.3094.

McIntosh, P. B.; Laskey, P.; Sullivan, K.; Davy, C.; Wang, Q.; Jackson, D. J.; Griffin, H. M.; Doorbar, J. E1--E4-mediated keratin phosphorylation and ubiquitylation: a mechanism for keratin depletion in HPV16-infected epithelium. *Journal of cell science* 2010, *123* (Pt 16), 2810–2822. DOI: 10.1242/jcs.061978.

Mikuličić, S.; Finke, J.; Boukhallouk, F.; Wüstenhagen, E.; Sons, D.; Homsi, Y.; Reiss, K.; Lang, T.; Florin, L. ADAM17-dependent signaling is required for oncogenic human papillomavirus entry platform assembly. *eLife* 2019, *8. DOI:* 10.7554/eLife.44345.

Mikuličić, S.; Florin, L. The endocytic trafficking pathway of oncogenic papillomaviruses. *Papillomavirus research (Amsterdam, Netherlands)* 2019, *7*, 135–137. DOI: 10.1016/j.pvr.2019.03.004.

Mikuličić, S.; Massenberg, A.; Döring, T.; Brandenburg, K.; Lang, T.; Florin, L. HSPG-binding peptide Pep19-2.5 is a potent inhibitor of HPV16 infection. *Antimicrobial agents and chemotherapy* 2025, *69* (2), e0157524. DOI: 10.1128/aac.01575-24.

Mikuličić, S.; Shamun, M.; Massenberg, A.; Franke, A.-L.; Freitag, K.; Döring, T.; Strunk, J.; Tenzer, S.; Lang, T.; Florin, L. ErbB2/HER2 receptor tyrosine kinase regulates human papillomavirus promoter activity. *Frontiers in immunology* 2024, *15*, 1335302. DOI: 10.3389/fimmu.2024.1335302.

Mikuličić, S.; Strunk, J.; Florin, L. HPV16 Entry into Epithelial Cells: Running a Gauntlet. *Viruses* 2021, *13* (12). DOI: 10.3390/v13122460.

Miladinova, E.; Lilkova, E.; Krachmarova, E.; Malinova, K.; Petkov, P.; Ilieva, N.; Nacheva, G.; Litov, L. Heparan Sulfate Facilitates Binding of hIFNγ to Its Cell-Surface Receptor hIFNGR1. *International journal of molecular sciences* 2022, *23* (16). DOI: 10.3390/ijms23169415.

Miranda, A. F.; Godman, G. C.; Tanenbaum, S. W. Action of cytochalasin D on cells of established lines. II. Cortex and microfilaments. *The Journal of cell biology* 1974, *62* (2), 406–423. DOI: 10.1083/jcb.62.2.406.

Mitani, T.; Takeda, S.; Oda, T.; Narita, A.; Maéda, Y.; Honda, H.; Fujiwara, I. Microscopic and structural observations of actin filament capping and severing by cytochalasin D. *Proceedings of the National Academy of Sciences of the United States of America* 2025, *122* (29), e2502164122. DOI: 10.1073/pnas.2502164122.

Mo, Y.; Ma, J.; Zhang, H.; Shen, J.; Chen, J.; Hong, J.; Xu, Y.; Qian, C. Prophylactic and Therapeutic HPV Vaccines: Current Scenario and Perspectives. *Frontiers in cellular and infection microbiology* 2022, *12*, 909223. DOI: 10.3389/fcimb.2022.909223.

Moody, C. A.; Laimins, L. A. Human papillomavirus oncoproteins: pathways to transformation. *Nature reviews. Cancer* 2010, *10* (8), 550–560. DOI: 10.1038/nrc2886.

Münger, K.; Phelps, W. C.; Bubb, V.; Howley, P. M.; Schlegel, R. The E6 and E7 genes of the human papillomavirus type 16 together are necessary and sufficient for transformation of primary human keratinocytes. *Journal of virology* 1989, *63* (10), 4417–4421. DOI: 10.1128/JVI.63.10.4417-4421.1989.

Ni, H.; Huang, C.; Ran, Z.; Li, S.; Kuang, C.; Zhang, Y.; Yuan, K. Targeting HPV for the prevention, diagnosis, and treatment of cervical cancer. *Journal of molecular cell biology* 2025, *16* (10). DOI: 10.1093/jmcb/mjae046.

Okun, M. M.; Day, P. M.; Greenstone, H. L.; Booy, F. P.; Lowy, D. R.; Schiller, J. T.; Roden, R. B. L1 interaction domains of papillomavirus l2 necessary for viral genome encapsidation. *Journal of virology* 2001, *75* (9), 4332–4342. DOI: 10.1128/JVI.75.9.4332-4342.2001.

Ozawa, T.; Tsuruta, D.; Jones, J. C. R.; Ishii, M.; Ikeda, K.; Harada, T.; Aoyama, Y.; Kawada, A.; Kobayashi, H. Dynamic relationship of focal contacts and hemidesmosome protein complexes in live cells. *The Journal of investigative dermatology* 2010, *130* (6), 1624–1635. DOI: 10.1038/jid.2009.439.

Ozbun, M. A. Extracellular events impacting human papillomavirus infections: Epithelial wounding to cell signaling involved in virus entry. *Papillomavirus research (Amsterdam, Netherlands)* 2019, *7*, 188–192. DOI: 10.1016/j.pvr.2019.04.009.

Ozbun, M. A.; Campos, S. K. The long and winding road: human papillomavirus entry and subcellular trafficking. *Current opinion in virology* 2021, *50*, 76–86. DOI: 10.1016/j.coviro.2021.07.010.

Pang, C. L.; Thierry, F. Human papillomavirus proteins as prospective therapeutic targets. *Microbial pathogenesis* 2013, *58*, 55–65. DOI: 10.1016/j.micpath.2012.11.002.

Pellegrini, L. Role of heparan sulfate in fibroblast growth factor signalling: a structural view. *Current opinion in structural biology* 2001, *11* (5), 629–634. DOI: 10.1016/s0959-440x(00)00258-x.

Plummer, M.; Martel, C. de; Vignat, J.; Ferlay, J.; Bray, F.; Franceschi, S. Global burden of cancers attributable to infections in 2012: a synthetic analysis. *The Lancet. Global health* 2016, *4* (9), e609-16. DOI: 10.1016/S2214-109X(16)30143-7.

Ramirez-Martínez, G. Editorial: Reviews in virus and host. *Frontiers in cellular and infection microbiology* 2024, *14*, 1445721. DOI: 10.3389/fcimb.2024.1445721.

Richards, K. F.; Bienkowska-Haba, M.; Dasgupta, J.; Chen, X. S.; Sapp, M. Multiple heparan sulfate binding site engagements are required for the infectious entry of human papillomavirus type 16. *Journal of virology* 2013, *87* (21), 11426–11437. DOI: 10.1128/JVI.01721-13.

Richards, K. F.; Mukherjee, S.; Bienkowska-Haba, M.; Pang, J.; Sapp, M. Human papillomavirus species-specific interaction with the basement membrane-resident non-heparan sulfate receptor. *Viruses* 2014, *6* (12), 4856–4879. DOI: 10.3390/v6124856.

Richards, R. M.; Lowy, D. R.; Schiller, J. T.; Day, P. M. Cleavage of the papillomavirus minor capsid protein, L2, at a furin consensus site is necessary for infection. *Proceedings of the National Academy of Sciences of the United States of America* 2006, *103* (5), 1522–1527. DOI: 10.1073/pnas.0508815103.

Ritsch, M.; Cassman, N. A.; Saghaei, S.; Marz, M. Navigating the Landscape: A Comprehensive Review of Current Virus Databases. *Viruses* 2023, *15* (9). DOI: 10.3390/v15091834.

Roman, A.; Munger, K. The papillomavirus E7 proteins. *Virology* 2013, *445* (1-2), 138–168. DOI: 10.1016/j.virol.2013.04.013.

Rommel, O.; Dillner, J.; Fligge, C.; Bergsdorf, C.; Wang, X.; Selinka, H.-C.; Sapp, M. Heparan sulfate proteoglycans interact exclusively with conformationally intact HPV L1 assemblies: basis for a virus-like particle ELISA. *Journal of medical virology* 2005, *75* (1), 114–121. DOI: 10.1002/jmv.20245.

Rothman, A. L. Immunity to dengue virus: a tale of original antigenic sin and tropical cytokine storms. *Nature reviews. Immunology* 2011, *11* (8), 532–543. DOI: 10.1038/nri3014.

Rumschlag-Booms, E.; Rong, L. Influenza a virus entry: implications in virulence and future therapeutics. *Advances in virology* 2013, *2013*, 121924. DOI: 10.1155/2013/121924.

Sapp, M.; Bienkowska-Haba, M. Viral entry mechanisms: human papillomavirus and a long journey from extracellular matrix to the nucleus. *The FEBS journal* 2009, *276* (24), 7206–7216. DOI: 10.1111/j.1742-4658.2009.07400.x.

Scheffer, K. D.; Berditchevski, F.; Florin, L. The tetraspanin CD151 in papillomavirus infection. *Viruses* 2014, *6* (2), 893–908. DOI: 10.3390/v6020893.

Scheffer, K. D.; Gawlitza, A.; Spoden, G. A.; Zhang, X. A.; Lambert, C.; Berditchevski, F.; Florin, L. Tetraspanin CD151 mediates papillomavirus type 16 endocytosis. *Journal of virology* 2013, *87* (6), 3435–3446. DOI: 10.1128/JVI.02906-12.

Schelhaas, M.; Ewers, H.; Rajamäki, M.-L.; Day, P. M.; Schiller, J. T.; Helenius, A. Human papillomavirus type 16 entry: retrograde cell surface transport along actin-rich protrusions. *PLoS pathogens* 2008, *4* (9), e1000148. DOI: 10.1371/journal.ppat.1000148.

Schelhaas, M.; Shah, B.; Holzer, M.; Blattmann, P.; Kühling, L.; Day, P. M.; Schiller, J. T.; Helenius, A. Entry of human papillomavirus type 16 by actin-dependent, clathrin- and lipid raft-independent endocytosis. *PLoS pathogens* 2012, *8* (4), e1002657. DOI: 10.1371/journal.ppat.1002657.

SCHERER, W. F.; SYVERTON, J. T.; GEY, G. O. Studies on the propagation in vitro of poliomyelitis viruses. IV. Viral multiplication in a stable strain of human malignant epithelial cells (strain HeLa) derived from an epidermoid carcinoma of the cervix. *The Journal of experimental medicine* 1953, *97* (5), 695–710. DOI: 10.1084/jem.97.5.695.

Schiffman, M.; Doorbar, J.; Wentzensen, N.; Sanjosé, S. de; Fakhry, C.; Monk, B. J.; Stanley, M. A.; Franceschi, S. Carcinogenic human papillomavirus infection. *Nature reviews. Disease primers* 2016, *2*, 16086. DOI: 10.1038/nrdp.2016.86.

Schiller, J. T.; Day, P. M.; Kines, R. C. Current understanding of the mechanism of HPV infection. *Gynecologic oncology* 2010, *118* (1 Suppl), S12-7. DOI: 10.1016/j.ygyno.2010.04.004.

Schliwa, M. Action of cytochalasin D on cytoskeletal networks. *The Journal of cell biology* 1982, *92* (1), 79–91. DOI: 10.1083/jcb.92.1.79.

Schmidt, S. C.; Massenberg, A.; Homsi, Y.; Sons, D.; Lang, T. Microscopic clusters feature the composition of biochemical tetraspanin-assemblies and constitute building-blocks of tetraspanin enriched domains. *Scientific reports* 2024, *14* (1), 2093. DOI: 10.1038/s41598-024-52615-1.

Selinka, H.-C.; Florin, L.; Patel, H. D.; Freitag, K.; Schmidtke, M.; Makarov, V. A.; Sapp, M. Inhibition of transfer to secondary receptors by heparan sulfate-binding drug or antibody induces noninfectious uptake of human papillomavirus. *Journal of virology* 2007, *81* (20), 10970–10980. DOI: 10.1128/JVI.00998-07.

Selinka, H.-C.; Giroglou, T.; Sapp, M. Analysis of the infectious entry pathway of human papillomavirus type 33 pseudovirions. *Virology* 2002, *299* (2), 279–287. DOI: 10.1006/viro.2001.1493.

Shanmugasundaram, S.; You, J. Targeting Persistent Human Papillomavirus Infection. *Viruses* 2017, *9* (8). DOI: 10.3390/v9080229.

Shoji, K.; Ohashi, K.; Sampei, K.; Oikawa, M.; Mizuno, K. Cytochalasin D acts as an inhibitor of the actin-cofilin interaction. *Biochemical and biophysical research communications* 2012, *424* (1), 52–57. DOI: 10.1016/j.bbrc.2012.06.063.

Smith, J. L.; Lidke, D. S.; Ozbun, M. A. Virus activated filopodia promote human papillomavirus type 31 uptake from the extracellular matrix. *Virology* 2008, *381* (1), 16–21. DOI: 10.1016/j.virol.2008.08.040.

Sparrer, M. N.; Hodges, N. F.; Sherman, T.; VandeWoude, S.; Bosco-Lauth, A. M.; Mayo, C. E. Role of Spillover and Spillback in SARS-CoV-2 Transmission and the Importance of One Health in Understanding the Dynamics of the COVID-19 Pandemic. *Journal of clinical microbiology* 2023, *61* (7), e0161022. DOI: 10.1128/jcm.01610-22.

Spoden, G.; Freitag, K.; Husmann, M.; Boller, K.; Sapp, M.; Lambert, C.; Florin, L. Clathrin- and caveolin-independent entry of human papillomavirus type 16--involvement of tetraspanin-enriched microdomains (TEMs). *PloS one* 2008, *3* (10), e3313. DOI: 10.1371/journal.pone.0003313.

Spoden, G. A.; Besold, K.; Krauter, S.; Plachter, B.; Hanik, N.; Kilbinger, A. F. M.; Lambert, C.; Florin, L. Polyethylenimine is a strong inhibitor of human papillomavirus and cytomegalovirus infection. *Antimicrobial agents and chemotherapy* 2012, *56* (1), 75–82. DOI: 10.1128/aac.05147-11.

Stanley, M. A. Epithelial cell responses to infection with human papillomavirus. *Clinical microbiology reviews* 2012, *25* (2), 215–222. DOI: 10.1128/CMR.05028-11.

Stevanović, S.; Draper, L. M.; Langhan, M. M.; Campbell, T. E.; Kwong, M. L.; Wunderlich, J. R.; Dudley, M. E.; Yang, J. C.; Sherry, R. M.; Kammula, U. S.; Restifo, N. P.; Rosenberg, S. A.; Hinrichs, C. S. Complete regression of metastatic cervical cancer after treatment with human papillomavirus-targeted tumor-infiltrating T cells. *Journal of clinical oncology : official journal of the American Society of Clinical Oncology* 2015, *33* (14), 1543–1550. DOI: 10.1200/JCO.2014.58.9093.

Surviladze, Z.; Dziduszko, A.; Ozbun, M. A. Essential roles for soluble virion-associated heparan sulfonated proteoglycans and growth factors in human papillomavirus infections. *PLoS pathogens* 2012, *8* (2), e1002519. DOI: 10.1371/journal.ppat.1002519.

Surviladze, Z.; Sterkand, R. T.; Ozbun, M. A. Interaction of human papillomavirus type 16 particles with heparan sulfate and syndecan-1 molecules in the keratinocyte extracellular matrix plays an active role in infection. *The Journal of general virology* 2015, *96* (8), 2232–2241. DOI: 10.1099/vir.0.000147.

Swift, L. M.; Asfour, H.; Posnack, N. G.; Arutunyan, A.; Kay, M. W.; Sarvazyan, N. Properties of blebbistatin for cardiac optical mapping and other imaging applications. *Pflugers Archiv : European journal of physiology* 2012, *464* (5), 503–512. DOI: 10.1007/s00424-012-1147-2.

Szymonowicz, K. A.; Chen, J. Biological and clinical aspects of HPV-related cancers. *Cancer biology & medicine* 2020, *17* (4), 864–878. DOI: 10.20892/j.issn.2095-3941.2020.0370.

Tao, Y.; Shao, H.; Zhang, T.; Pu, J.; Tang, C. Factors Influencing Men's Attitudes toward HPV Vaccination in Males Included in the Chinese National Immunization Program. *Vaccines* 2022, *10* (7). DOI: 10.3390/vaccines10071054.

Taylor, M. P.; Koyuncu, O. O.; Enquist, L. W. Subversion of the actin cytoskeleton during viral infection. *Nature reviews. Microbiology* 2011, *9* (6), 427–439. DOI: 10.1038/nrmicro2574.

Taylor, M. W. Introduction: A Short History of Virology. In *Viruses and Man: A History of Interactions*; Taylor, M. W., Ed.; Springer International Publishing: Cham, 2014; pp 1–22. DOI: 10.1007/978-3-319-07758-1_1.

Tian, J.; Li, C.; Li, W. Entry of hepatitis B virus: going beyond NTCP to the nucleus. *Current opinion in virology* 2021, *50*, 97–102. DOI: 10.1016/j.coviro.2021.08.001.

Tommasino, M. The human papillomavirus family and its role in carcinogenesis. *Seminars in cancer biology* 2014, *26*, 13–21. DOI: 10.1016/j.semcancer.2013.11.002.

Trus, B. L.; Roden, R. B.; Greenstone, H. L.; Vrhel, M.; Schiller, J. T.; Booy, F. P. Novel structural features of bovine papillomavirus capsid revealed by a three-dimensional reconstruction to 9 A resolution. *Nature structural biology* 1997, *4* (5), 413–420. DOI: 10.1038/nsb0597-413.

Vande Pol, S. B.; Klingelhutz, A. J. Papillomavirus E6 oncoproteins. *Virology* 2013, *445* (1-2), 115–137. DOI: 10.1016/j.virol.2013.04.026.

Vasioukhin, V.; Bauer, C.; Yin, M.; Fuchs, E. Directed actin polymerization is the driving force for epithelial cell-cell adhesion. *Cell* 2000, *100* (2), 209–219. DOI: 10.1016/s0092-8674(00)81559-7.

Vilas Boas, L. C. P.; Campos, M. L.; Berlanda, R. L. A.; Carvalho Neves, N. de; Franco, O. L. Antiviral peptides as promising therapeutic drugs. *Cellular and molecular life sciences : CMLS* 2019, *76* (18), 3525–3542. DOI: 10.1007/s00018-019-03138-w.

Villiers, E.-M. de; Fauquet, C.; Broker, T. R.; Bernard, H.-U.; zur Hausen, H. Classification of papillomaviruses. *Virology* 2004, *324* (1), 17–27. DOI: 10.1016/j.virol.2004.03.033.

Wang, X.; Liu, H.; Ge, H.; Ajiro, M.; Sharma, N. R.; Meyers, C.; Morozov, P.; Tuschl, T.; Klar, A.; Court, D.; Zheng, Z.-M. Viral DNA Replication Orientation and hnRNPs Regulate Transcription of the Human Papillomavirus 18 Late Promoter. *mBio* 2017, *8* (3). DOI: 10.1128/mBio.00713-17.

Woodham, A. W.; Da Silva, D. M.; Skeate, J. G.; Raff, A. B.; Ambroso, M. R.; Brand, H. E.; Isas, J. M.; Langen, R.; Kast, W. M. The S100A10 subunit of the annexin A2 heterotetramer facilitates L2-

mediated human papillomavirus infection. *PloS one* 2012, *7* (8), e43519. DOI: 10.1371/journal.pone.0043519.

Wüstenhagen, E.; Hampe, L.; Boukhallouk, F.; Schneider, M. A.; Spoden, G. A.; Negwer, I.; Koynov, K.; Kast, W. M.; Florin, L. The Cytoskeletal Adaptor Obscurin-Like 1 Interacts with the Human Papillomavirus 16 (HPV16) Capsid Protein L2 and Is Required for HPV16 Endocytosis. *Journal of virology* 2016, *90* (23), 10629–10641. DOI: 10.1128/JVI.01222-16.

Yokoyama, H.; Sato, K.; Okudaira, M.; Morita, C.; Takahashi, C.; Suzuki, D.; Sakai, H.; Iwamoto, Y. Serum and urinary concentrations of heparan sulfate in patients with diabetic nephropathy. *Kidney international* 1999, *56* (2), 650–658. DOI: 10.1046/j.1523-1755.1999.00591.x.

Yoon, C. S.; Kim, K. D.; Park, S. N.; Cheong, S. W. alpha(6) Integrin is the main receptor of human papillomavirus type 16 VLP. *Biochemical and biophysical research communications* 2001, *283* (3), 668–673. DOI: 10.1006/bbrc.2001.4838.

Yu, L.; Majerciak, V.; Lobanov, A.; Mirza, S.; Band, V.; Liu, H.; Cam, M.; Hughes, S. H.; Lowy, D. R.; Zheng, Z.-M. HPV oncogenes expressed from only one of multiple integrated HPV DNA copies drive clonal cell expansion in cervical cancer. *mBio* 2024, *15* (5), e0072924. DOI: 10.1128/mbio.00729-24.

Yu, L.; Majerciak, V.; Zheng, Z.-M. HPV16 and HPV18 Genome Structure, Expression, and Post-Transcriptional Regulation. *International journal of molecular sciences* 2022, *23* (9). DOI: 10.3390/ijms23094943.

Zhang, Q.; Tang, W.; Stancanelli, E.; Jung, E.; Syed, Z.; Pagadala, V.; Saidi, L.; Chen, C. Z.; Gao, P.; Xu, M.; Pavlinov, I.; Li, B.; Huang, W.; Chen, L.; Liu, J.; Xie, H.; Zheng, W.; Ye, Y. Host heparan sulfate promotes ACE2 super-cluster assembly and enhances SARS-CoV-2-associated syncytium formation. *Nature communications* 2023, *14* (1), 5777. DOI: 10.1038/s41467-023-41453-w.

Zhang, Y.; Qiu, K.; Ren, J.; Zhao, Y.; Cheng, P. Roles of human papillomavirus in cancers: oncogenic mechanisms and clinical use. *Signal transduction and targeted therapy* 2025, *10* (1), 44. DOI: 10.1038/s41392-024-02083-w.

Zheng, Z.-M.; Wang, X. Regulation of cellular miRNA expression by human papillomaviruses. *Biochimica et biophysica acta* 2011, *1809* (11-12), 668–677. DOI: 10.1016/j.bbagrm.2011.05.005.

Zona, L.; Lupberger, J.; Sidahmed-Adrar, N.; Thumann, C.; Harris, H. J.; Barnes, A.; Florentin, J.; Tawar, R. G.; Xiao, F.; Turek, M.; Durand, S. C.; Duong, F. H. T.; Heim, M. H.; Cosset, F.-L.; Hirsch, I.; Samuel, D.; Brino, L.; Zeisel, M. B.; Le Naour, F.; McKeating, J. A.; Baumert, T. F. HRas signal transduction promotes hepatitis C virus cell entry by triggering assembly of the host tetraspanin receptor complex. *Cell host & microbe* 2013, *13* (3), 302–313. DOI: 10.1016/j.chom.2013.02.006.

zur Hausen, H. Papillomaviruses and cancer: from basic studies to clinical application. *Nature reviews. Cancer* 2002, *2* (5), 342–350. DOI: 10.1038/nrc798.

7. Danksagung

Zuerst möchte ich mich bei Prof. Dr. Thorsten Lang für die Möglichkeit bedanken in seiner Arbeitsgruppe an diesem spannenden und interessanten Projekt zu arbeiten. Vielen Dank für die freundliche Hilfe, Unterstützung und wertvollen Diskussionen. Unsere Gespräche werden mir stets als bereichernder und motivierender Austausch in Erinnerung bleiben. Ein großer Dank geht auch an Prof. Dr. Luise Florin und Dr. Snježana Mikuličić für ihre Unterstützung, Bereitstellung der PsVs und die Kooperation bei diesem Projekt. Vielen Dank auch an die DFG für die Bereitstellung der Finanzierung des Forschungsprojekts. Außerdem möchte ich auch Prof. Dr. Eva Kiermaier für die Übernahme des Zweitgutachtens danken.

Ein großes Dankeschön geht an alle aktuellen und ehemaligen Mitglieder der AG Lang. Vielen Dank für eure Unterstützung und die durchgängig angenehme, freundliche und kollegiale Arbeitsatmosphäre. Besonderer Dank geht dabei an Sara Konopka, Charlie Schneider, Kerstin Pinkwart und Yahya Homsi, die immer für mich da waren, auch wenn es mal nicht so gut lief. Vielen Dank für eure Hilfsbereitschaft und eure Beiträge und Anregungen im Labmeeting. Ich habe großes Glück gehabt so großartige Kollegen zu haben mit denen man sich auch außerhalb des Labs so gut versteht. Ohne euch hätte die ganze Arbeit nur halb so viel Spaß gemacht. Vielen Dank auch an die Mitglieder der AG Burgdorf, AG Kiermaier und AG Kolanus, die immer für eine lockere und entspannte Stimmung in der Mittagspause gesorgt haben. Gerne möchte ich hier auch die Gelegenheit nutzen mich bei meinen Lieblingsbands als auch den Mitwirkenden diverser Hörspielreihen zu bedanken ohne die die langen Tage vor dem STED-Mikroskop doch sehr langweilig gewesen wären.

Als nächstes möchte ich mich bei meinen Freunden bedanken, die mich in dieser Zeit stets unterstützt haben. Vielen Dank an Alex, Katrin, Kira, Niklas, Lukas, Philipp und Yannick (der ja eigentlich schon zur Familie gehört). Ich kann mich immer auf euren Support verlassen. Ob bei gemeinsamen Spieleabenden, DnD/PnP Kampagnen, Krimi-Dinner oder Konzerten, zusammen mit euch habe ich immer eine passende Ablenkung gefunden, wenn es auch mal nicht so gut lief. Vielen Dank für eure langjährige Unterstützung und Freundschaft (teilweise ja sogar schon seit über 25 Jahren (wir werden (sind) alle alt)).

Mein größter Dank geht natürlich an meine Familie. An meine Eltern, die mich immer unterstützen und immer für mich da sind. Ich kann mich immer auf euch verlassen und ihr habt stets an mich geglaubt. An Carina, der besten kleinen Schwester, die man sich nur wünschen kann. Es ist großartig eine Schwester zu haben, mit der man sich so gut versteht und mit der man alles zusammen machen und teilen kann. Ich schätze mich sehr glücklich dich nicht nur eine Schwester, sondern auch eine

Freundin nennen zu können. Ich bin unendlich dankbar, eine so großartige Familie zu haben, die immer für einen da ist. Danke für alles!

In Gedenken an Alle, die viel zu früh von uns gegangen sind.